Hydrothermal Chemistry of Methylene Chloride and MTBE: Experimental Kinetics and Reaction Pathways

by

Joshua D. Taylor

B.S., Chemical Engineering
University of California at Berkeley, 1995

M.S., Chemical Engineering Practice
Massachusetts Institute of Technology, 1998

Submitted to the Department of Chemical Engineering
in Partial Fulfillment of the Requirements for the Degree of

DOCTOR OF SCIENCE IN CHEMICAL ENGINEERING

at the

MASSACHUSETTS INSTITUTE OF TECHNOLOGY

February, 2001

Signature of Author: ______________________
Department of Chemical Engineering
January 9, 2001

Certified by: ______________________
Professor Jeffrey I. Steinfeld
Thesis Supervisor

Certified by: ______________________
Professor Jefferson W. Tester
Thesis Supervisor

Accepted by: ______________________
Professor Robert E. Cohen
St. Laurent Professor of Chemical Engineering
Chairman, Committee for Graduate Students

Hydrothermal Chemistry of Methylene Chloride and MTBE: Experimental Kinetics and Reaction Pathways

by
Joshua D. Taylor

Submitted to the Department of Chemical Engineering on
December 15, 2000 in partial fulfillment of the requirements for the
Degree of Doctor of Science in Chemical Engineering

Abstract

With the growing desire for sustainable technologies, reactions in benign solvents, such as hydrothermal water and supercritical fluids, have become the focus of many investigations. Hydrothermal water has been used as a medium for chemical reactions, where the enhanced dissociation constant of water led to both acid- and base-catalysis without added reagents. Supercritical water oxidation (SCWO) has been proposed as an alternative technology for the treatment of aqueous-organic waste streams. At typical SCWO conditions ($T = 550$-650°C and $P = 250$-300 bar), mixed organic waste streams can be completely mineralized (>99.99%) in residence times of less than one minute. In an SCWO process, the waste stream is preheated to temperatures of >400°C in the absence of oxygen prior to the reactor. In the preheater, hydrolysis reactions may occur, significantly changing the composition of the reactor feed. To properly model these processes, a fundamental understanding of the reaction pathways and associated rates is essential.

The rates of methylene chloride and methyl *tert*-butyl ether (MTBE) hydrolysis in sub- and supercritical water have been measured experimentally at 250 bar over a range of temperatures from 100 to 600°C. The rate constants for both compounds showed a local maximum below the critical temperature of water (374°C) followed by a local minimum just above the critical temperature. This behavior was qualitatively attributed to the changes in the solvent properties of water, shifting from a polar solvent in the subcritical region to a nonpolar solvent in the supercritical region. One of the primary objectives of this thesis was to develop a better understanding of the molecular-level effects of the solvent on the reaction rates and mechanistic pathways.

The effects of water as a solvent on the hydrolysis reaction of CH_2Cl_2 were modeled as a dielectric continuum using Kirkwood theory. A correction factor, obtained from *ab initio* calculations, was applied to adjust the activation energy in order to account for differences in the free energy of solvation of the reactant and the transition state. Application of the Kirkwood correction to the empirical rate expression fit to data from 100-250°C yielded a model that quantitatively agreed with the experimentally measured reaction rate over the entire temperature range (from 100 to 500°C).

To explain the extrema in the rate constant measured for MTBE hydrolysis, an acid-catalyzed mechanism was proposed. A new empirical rate expression was determined with a first-order dependence on the concentrations of H^+ and MTBE. For the entire temperature range studied from 150 to 600°C, the empirical rate expression quantitatively modeled the experimentally measured decomposition rate within the uncertainty of the experiments.

Further experiments were conducted with added HCl or NaOH that validated the acid-catalyzed hydrolysis pathway. The experimentally observed dependence on the concentration of H^+ was slightly smaller than predicted by the proposed mechanism. *Ab intio* tools were employed to determine the relative contribution of a unimolecular decomposition pathway, which concluded that the pathway was not significant below 550°C. The unimolecular decomposition pathway set a lower limit on the overall reaction rate, which was observed experimentally under basic conditions where the acid-catalyzed pathway was effectively shut off.

In addition to the kinetic measurements, two new experimental tools were developed to improve the capabilities of the supercritical fluids laboratory. Firstly, a new, large-bore tubular reactor system was built to address limitations in the current flow reactors in the supercritical fluids laboratory. The reactor was designed with the following advantages: 1) large diameter to minimize wall effects; 2) direct organic feed to eliminate hydrolysis during preheaters; 3) movable sampling probe; 4) sapphire windows to allow optical accessibility. The reactor was tested in preliminary runs up to 600°C and 250 bar. Secondly, a new reactor system was built to allow optical accessibility for *in situ* Raman spectroscopic measurement in supercritical fluids. The system was used in a study to probe local solvent effects in supercritical carbon dioxide. The effect of temperature, pressure, and density of CO_2 on the vibrations of benzene and methylene chloride were investigated. As the density of CO_2 increased, the vibrations shifted to lower frequency initially, and then leveled off at moderate densities. This leveling off may be due to local clustering of solvent molecules around solutes in these systems.

Thesis Supervisors: Jeffrey I. Steinfeld
Professor of Chemistry

Jefferson W. Tester
Herman P. Meissner Professor of Chemical Engineering
Director of the MIT Energy Laboratory

Acknowledgements

While people may say, "**you** did it," I am keenly aware that without the help of many smart people around me, this would not have been possible. I am first and foremost thankful to my advisors, Jeff Steinfeld and Jeff Tester. They both allowed me the freedom and flexibility to shape my own research project and gave me the resources to do so. They offered direction and asked all of the right questions. I am thankful for the opportunities they gave me to attend conferences to develop professionally, as well as their concern for my personal well being.

I am also grateful to my thesis committee, who helped me to focus my project from the start and provided direction throughout my stay at MIT. Professor Ken Smith kept me honest, forced me to shoot straight with him, and wouldn't let me get away with waving my hands. Dr. Bill Peters gave a fresh perspective in his thought-provoking questions and was always very supportive of my work. Professor K.C. Swallow taught me that analytical chemistry is not a matter of injecting samples into a black box and obtaining all the answers. I appreciate her help and friendly guidance along the way. Although not official members of my thesis committee, Professors Bill Green and Bernhardt Trout were both very helpful in teaching me how to perform *ab initio* calculations. Both were willing to set time aside for me to come ask them questions and I learned a lot from them.

I would like to thank several members of the support staff that have been helpful and patient with me along the way. Anyone associated with the energy lab knows that nothing would happen without the assistance of Bonnie Murphy. Thank you so much for your patience and help over the years. Jocelyn Dewitt, has been a joyful addition to the elab support staff and I appreciate her. In the student office, Janet Fisher and Elaine Aufiero were both always willing to help with any problems or happy to just talk and be friends to me. Arline Benford was always the informant of available food and always made me feel special when I saw her. Finally, our practice school mom, Carol Phillips, though she is missed dearly, will always live in our hearts. We all love you Carol.

Joining "Team Tester" was clearly the best decision I made in my first year at MIT. The people in the group made spending 40+ hours per week in the basement of a cement building actually enjoyable. These are also the people who became my companions in rafting, hiking, skiing, and biking. They showed me restaurants around Boston, and even as far as Maine. Although this could not do justice to how grateful I am, I would like to take a moment to recognize each of them.

Joanna Blanchard was always willing to let me pester her with an endless barrage of questions. She was key in organizing so many of our fun activities and was a dear friend to me. Brian Phenix helped me in the early stages to set goals and focus on realistic thesis objectives. Brian was also responsible for a trip to one of the nicest restaurants in Boston. Matt DiPippo was instrumental in helping me get started out with

equipment in the lab. He was always willing to drop what he was doing to help me out. I am grateful to Phil Marrone who set the stage for much of my work with CH_2Cl_2 and the large reactor. Phil continues to be very helpful when I have questions and I enjoy his friendship. Randy Weinstein provided countless hours of entertainment in lab with his exploits in MIT theater and elsewhere. Randy's energy and motivation also make him a great Professor and I wish him the best in his career. Matt Reagan took over the outdoor trip arrangements when Joanna left and always worked hard to get our ski trip at the best locations. I wish Matt the best of luck in his next career move to one (?) of the National labs in Livermore. Jason Cline and Mike Kutney were both huge helps to me in the realm of computers. I thank Jason for teaching me the basics of UNIX and somehow swindling access for me to use the Pleiades cluster through the physics department. I also thank Mike for always being willing to come over whenever Bill Gates caused us problems in the lab. Two postdocs who played important parts in our group were Dolors Salvatierra and Fredric Vogel. I enjoyed working closely with Dolors on the CH_2Cl_2 studies and somehow I managed to get a trip to Barcelona out of the deal. I also learned very much from working alongside Fredric, who is one of the best engineers I know.

Of the present Team Tester members, I especially thank Mike Timko. I have learned so much from our brainstorming sessions and our light talks on the way to coffee breaks. I pass on the torch to Mike as senior member in the lab and know that it is in good hands. Zhitao Cao has been a great addition to the group since he initiated the Trout-Tester bridge. Zhitao has been a great sport in learning new activities and joining in on group outings. I also thank Zhitao for providing me some computational time on Clathrate and for loaning me the laptop for my defense. Patty, Paul, and Murray, whose names will always remind me of an oldies group, are the most recent additions to our team. They add a great dynamic to the lab and will carry on the tradition of "best group on campus". I am thankful to Patty for her presence and friendship in the lab over this past year (You can bug me with questions whenever you like). Joe S. and Wolfgang Voelcker were both visiting students who made significant contributions to the group in a relatively short time period. I thank Liz Gron for her advice and encouragement over this past half year. And finally, I'd like to acknowledge Federico Pacheco. Federico was an outstanding undergraduate researcher who helped me get started on the pH experiments.

Outside of MIT, many people have impacted my life and made it possible for me to be where I am today. My parents have been so supportive of me through my countless years of schooling. I owe this all to them and love them dearly. I can only hope to be as good a parent as they are. I admire my brother, Sean, more than he could ever realize. I always wanted to be as good as him at everything and he challenged me to aim high. My biggest support and strength over these past two years has come from my soon-to-be-Bride, Shaundra. I cannot even begin to express my love and gratitude for everything you are to me (including editor of this thesis). Finally, although not politically correct at MIT, I am thankful to Jesus Christ, through whom I can do all things.

“If this is dying, it’s not so bad”

—Harry Potter

From J.K. Rowlings
Harry Potter and the
Chamber of Secrets

Table of Contents

List of Figures

List of Tables

Chapter 1

Introduction and background

In this chapter, a general background of supercritical fluids is presented, with emphasis on their physical properties. Following the background is a description of the supercritical water oxidation process and its current status. Finally, a review of relevant studies and significant contributors to the field is provided. The intention of the review is not to be comprehensive, but to provide a general overview of the collection of research publications to date. In Section 1.3, studies that utilized high-temperature, high-pressure water for hydrolysis or synthetic chemistry are discussed. In Section 1.4, basic research studies on SCWO kinetics are described. A fairly complete summary of experiments and modeling by our group at MIT is provided, followed by a brief synopsis of studies by groups elsewhere.

1.1 Supercritical Fluids

For a pure substance, the critical point is defined as the terminus of the liquid-vapor coexistence curve on a P–T diagram. At this point, the liquid and vapor phases are indistinguishable from one another and form one fluid phase. As the temperature or pressure is increased beyond its critical value (as shown by the shaded regions in Figures 1.1 a and b), no phase changes will occur for all possible variations in temperature or pressure. Under these conditions, the fluid is referred to as supercritical.

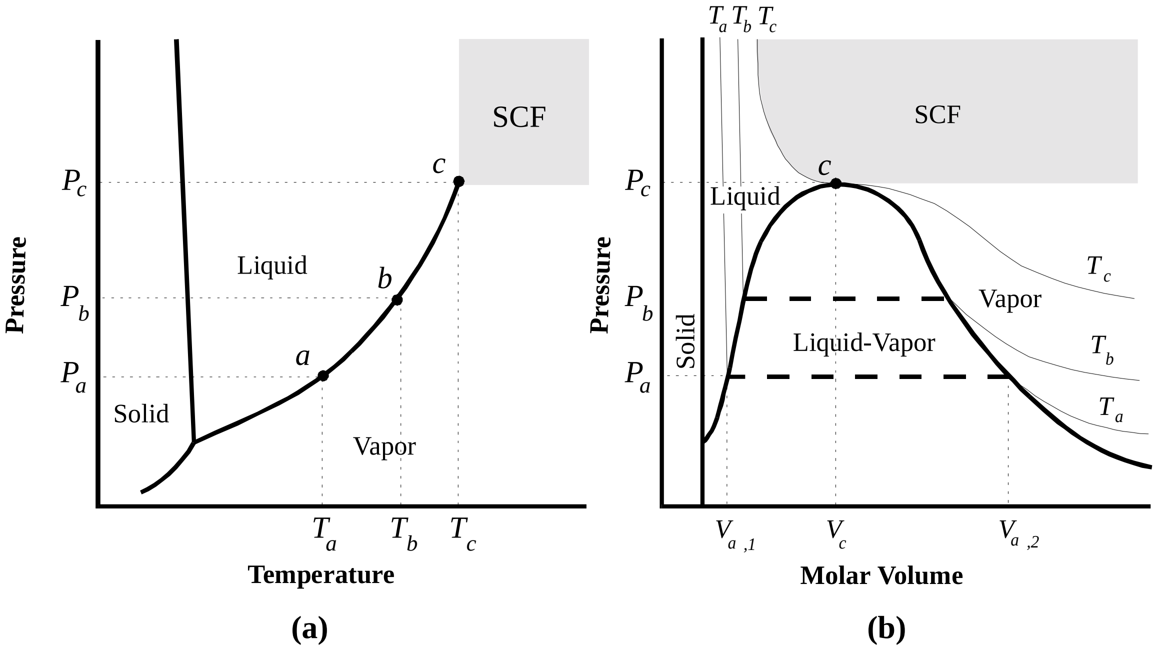

Figure 1.1: (a) Generic single component *P-T* diagram (b) Generic single component *P-V* diagram with isotherms drawn at T_a, T_b, and T_c.

The critical point is best illustrated by the following mental exercise. Imagine that a pure liquid partially fills a container and is in equilibrium with its vapor in the headspace. The state of this system corresponds to a point on the liquid-vapor coexistence curve that we shall label "*a*" in the generic *P–T* diagram shown in Figure 1.1a. On the corresponding *P–V* diagram (Figure 1.1b), the state of this system is illustrated by the tie line (dashed) at T_a and P_a. The ends of the tie line represent the molar volume (or density) of the liquid ($V_{a,1}$) and the vapor ($V_{a,2}$) respectively. As the temperature is increased to T_b and as the vapor pressure reaches P_b, the liquid phase expands and the molar volume of the vapor decreases. If the temperature is increased further, the molar volumes of the two phases approach the same value until the critical point (*c*) is reached. At this point, the densities of the liquid and vapor phases are equal ($\rho_L = \rho_V = \rho_c$) and form one fluid phase with $T = T_c$ and $P = P_c$.

Since phase changes do not occur in the supercritical fluid region, physical properties vary continuously with changes in temperature and pressure. A supercritical fluid is often referred to as a dense gas, but most of its physical properties are intermediate to those of a gas and a liquid. Table 1.1 lists typical values of density, viscosity, and diffusivity for the three fluid phases so that their physical properties may be compared (Squires *et al.*, 1983).

Table 1.1: Comparison of liquid, supercritical fluid, and gas-phase physical properties

	Liquid	**Supercritical Fluid**	**Gas**
Density (g/cc)	1	10^{-1}	10^{-3}
Viscosity (Pa s)	10^{-3}	10^{-4}	10^{-5}
Diffusivity (cm^2/s)	10^{-5}	10^{-4}	10^{-1}

Under extreme pressure or temperature, the physical properties can vary significantly from liquid-like to gas-like values. Because solvation depends primarily on density, supercritical fluids can make good solvents for a wide range of compounds at moderate to high densities (Villard, 1896). Additionally, because the density may be decreased significantly by a modest drop in pressure, some compounds can be selectively separated from mixtures dissolved in supercritical fluids. A combination of good solvent strength and enhanced transport properties over liquids makes supercritical fluids attractive media for chemical reactions.

The critical values of temperature and pressure can vary drastically for different components. Generally, critical constants are lower for species with weak intermolecular interactions and higher for species with strong attractive forces and molecular ordering. Table 1.2 provides a list of critical constants for several representative fluids.

Table 1.2: List of critical constants for selected compounds (from Weast, 1975)

	T_c (°C)	P_c (bar)
Helium	–239.9	2.3
Argon	–122.3	48.7
Methane	–82.1	46.0
Ethane	32.2	48.8
Propane	96.8	42.5
Carbon Dioxide	31.1	73.8
Ammonia	132.5	113.5
Water	374.1	221.2

Although many supercritical fluids have been used in research laboratories, carbon dioxide (CO_2) and water have gained the most widespread use because they are abundant in nature, non-toxic, and chemically inert. Supercritical (and liquid) CO_2 is used for extraction and cleaning applications because of its desirable solvent strength and mild critical conditions (McHugh and Krukonis, 1986). For example, the industrial decaffeination of coffee and the extraction of flavor from hops are accomplished via supercritical CO_2. Likewise, the degreasing of microelectronics and a new environmentally friendly dry cleaning technique also utilize supercritical or liquid CO_2 as a solvent. Additionally, supercritical CO_2 is being studied extensively as an environmentally benign replacement solvent for organic syntheses and transformations (Savage, 1999; DeSimone *et al.*, 1992; Weinstein *et al.*, 1996).

Because the critical temperature of water is relatively high, many compounds become unstable. Consequently, supercritical water (SCW) is a more effective medium for the destruction and degradation of organic compounds rather than for their synthesis. The oxidation of hazardous organic wastes and the recovery of monomers from recycled polymers are practical examples that employ SCW. Water also elicits great interest from a fundamental chemistry and thermodynamics standpoint due to the dramatic changes that occur in macroscopic physical properties and molecular interactions as one passes through the critical region. The following subsections discuss the unique properties of supercritical water and its potential uses in greater detail.

1.1.1 Properties of Supercritical Water (SCW)

In passing from a liquid to a supercritical state, water exhibits reduced hydrogen bonding and molecular ordering, resulting in physical properties that are dramatically different from those of liquid water under ambient conditions. To illustrate this, consider ice as a fully hydrogen bonded network where each molecule donates two hydrogen atoms to H-bonds and accepts two H-bonds with its two lone pairs of electrons. As ice melts, some of this network is broken, allowing molecules to migrate past one another. Yet even as a liquid, the average number of H-bonds remains fairly high at a value of 3.2 (counting accepted and donated H-bonds equally). However, SCW under conditions of interest has only 0.5 to 2 H-bonds per molecule (Kalinichev and Bass, 1997).

The reduced hydrogen bonding and molecular ordering is in part due to the decreased density of SCW. A plot of the density, ρ, and the dielectric strength (relative to vacuum), ε, as functions of temperature at 250 bar is shown in Figure 1.2 (Haar *et al.*, 1984); (Uematsu and Franck, 1980). The density shows a modest decline as the temperature increases towards T_c, then decreases sharply in the critical region, and finally levels off at values of about 0.1 g/cc at temperatures above 420°C.

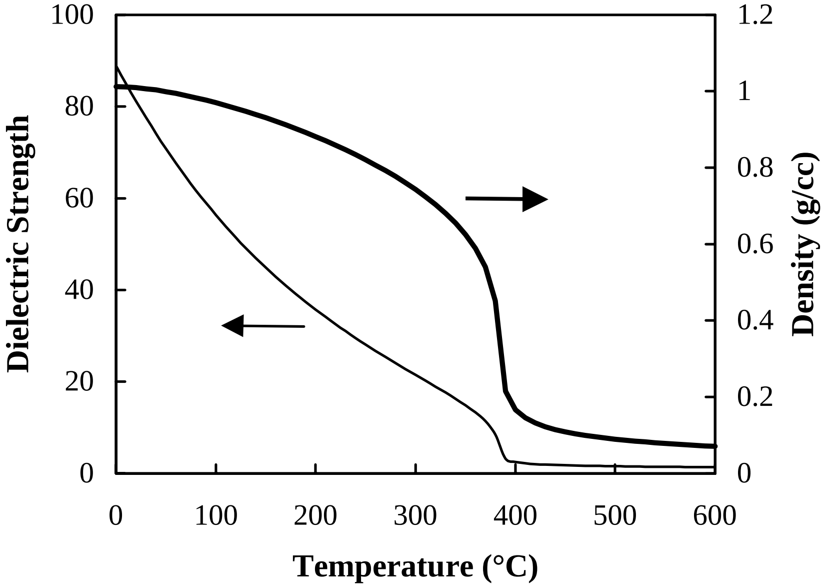

Figure 1.2: Density and dielectric strength of water at 250 bar

The dielectric strength characterizes the ability of a solvent to shield a charge or to stabilize a charge separation (such as a dipole moment). As the thermal energy of the solvent molecules increase and the density decreases, water molecules cannot arrange around solutes to shield charges or dipole moments. This result is seen in the decrease of dielectric strength from 80 at 25ºC to approximately 10 at the critical temperature, and finally reaching values of 3 to 1.5 far above T_c. Although a very polar solvent under ambient conditions, water behaves like moderately polar organic solvents below T_c, and in its supercritical state is comparable to nonpolar liquid organic solvents such as hexane or toluene.

Because it behaves as a nonpolar solvent, most organic compounds and gases such as O_2, N_2, CO, and CO_2 dissolve miscibly in SCW. SCW's ability to solvate organic compounds and oxygen make it an attractive medium for the oxidation of hazardous waste streams. However, ionic species are very sparingly soluble in SCW. Dissolved salts exist primarily as associated pairs since SCW cannot stabilize the individual ions. Therefore, the presence of salts in processes utilizing SCW is problematic due to the potential for plugging.

The inability of SCW to solvate dissociated charged species is further demonstrated by the decrease in the ion-dissociation constant of water, K_w^*. K_w^* is defined as the product of the activity of H^+ and OH^-. A decrease in K_w^* indicates a decrease in the relative number of dissociated H_2O molecules. Figure 1.3 shows a plot of K_w^* versus temperature at 250 bar [1](Marshall and Franck, 1981; Bandura and Lvov, 2000). As temperature is increased below T_c, K_w^* increases to values as high as 10^{-11} where acid- and base-catalyzed pathways are both enhanced. Near the critical temperature, K_w^* decreases by approximately 7 orders of magnitude, indicating that water exists almost exclusively as molecular water. Such behavior indicates that ionic reaction pathways would be enhanced in subcritical water and greatly diminished in supercritical water. Typically, free-radical pathways and nonionic reactions dominate in the supercritical region (Tester *et al.*, 1993).

---

[1] The values of K_w^* in Figure 1.3 were obtained from the correlation by Marshall and Franck for densities above 0.4 g/cc and from a correlation by Bandura and Lvov for densities less than 0.4 g/cc (see Appendix 11.1).

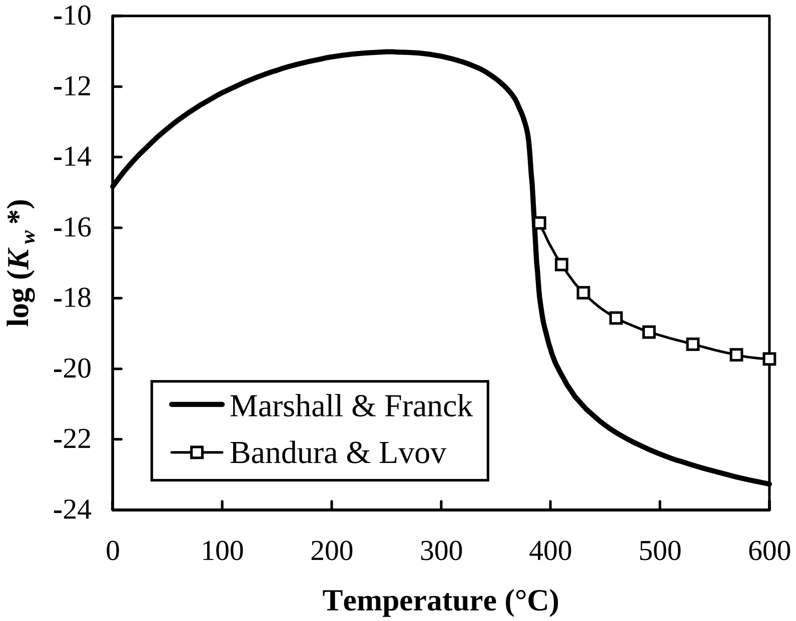

Figure 1.3: The ion dissociation constant of water at 250 bar, including two different correlations for supercritical temperatures (see Appendix 11.1).

1.2 Supercritical Water Oxidation

The supercritical water oxidation (SCWO) process generally refers to hydrothermal oxidation remediation of hazardous organic waste streams in supercritical water. As described in Section 1.1.1, SCW is completely miscible with most organic compounds and oxygen, providing an ideal environment where oxidation reactions occur without mass transport limitations caused by phase boundaries. Under typical operating conditions for SCWO (P = 250 to 300 bar and T = 450 to 650ºC), free-radical reactions occur rapidly, resulting in complete (>99.99%) mineralization of most organic compounds in less than one minute (Tester *et al.*, 1993). The free-radical reaction mechanisms are similar to those seen in combustion, but because of the moderate temperatures (relative to combustion) and abundance of water in SCWO, the mechanisms depend on different radical species as the primary initiators and propagators.

Analogous to combustion, organics are completely oxidized to CO_2 and H_2O. Yet due to the more moderate temperatures of SCWO, species containing nitrogen produce mostly molecular N_2 and some N_2O rather than NO_x (Killilea and Swallow, 1992). Heteroatoms (*e.g.*, Cl, S, P) are oxidized to their respective inorganic acids (HCl, H_2SO_4, H_3PO_4), which are typically neutralized with caustic to prevent corrosion. The resulting salts can be very insoluble and precipitate from the SCW, necessitating their removal. An exception to this is NaCl, which can form a dense brine solution (rather than precipitating out as a solid) that may reach 60 wt. % in equilibrium with the supercritical fluid for temperatures ranging from 380 to 450°C.

1.2.1 Applications

In the United States alone, the chemical industry produces 300 million tons of aqueous waste per year. Annually, the pulp and paper industry generates another 28 million (dry) tons of aqueous sludges and municipalities generate an additional 7 million dry tons of metabolic sludge (Modell, 1995). After bioremediation of these municipal and paper wastes, the aqueous sludges are difficult to dewater beyond 30%, requiring landfills as a means of disposal. As landfills become less viable throughout the world, effective methods for the treatment of organic waste streams and aqueous sludges become necessary. SCWO has been demonstrated as a viable technology for the complete oxidation of such wastes and sludges.

In economic terms, SCWO is competitive for treatment of difficult-to-dewater aqueous waste streams that are 1 to 20 wt% organics (Modell, 1989; Thomason *et al.*, 1990). At higher concentrations of organics, combustion is the most cost-effective treatment option. However, because of public opposition to incinerators, SCWO is being considered for the destruction of many concentrated organic streams of very hazardous compounds, such as chemical weapons, explosives, and other military wastes (Shaw *et al.*, 1991). For dilute aqueous wastes (<1 wt%), bioremediation or adsorption on activated carbon is generally the most cost-effective option. Although not truly a treatment technology, activated carbon adsorption is used for the removal of dilute contaminants from aqueous streams. At concentrations above 1%, the cost of regenerating or replacing the carbon makes this technique cost-prohibitive. Bioremediation is effective on well-characterized feed streams under conditions optimized for a specific waste. However, changes in the composition of waste or of particularly toxic substances may lead to microbial death, rendering many bioremediation processes ineffective. Conversely, SCWO is relatively insensitive to variations in feed composition and attacks all H/C/N organic substances indiscriminately.

SCWO has been used effectively to treat a variety of sludges, hazardous waste streams, and toxic substances in research laboratories and pilot-scale facilities. Examples of sludges treated with SCWO include human metabolic waste (Hong *et al.*, 1987); (Hong *et al.*, 1988), municipal sludge (Shanableh and Gloyna, 1991), a mixture of municipal sludge and distillery wastewater (Goto *et al.*, 1998), pulp and paper sludge (Modell *et al.*, 1992), and a mixture of primary clarifier sludge with bleach plant effluent (Cooper *et al.*, 1997). Other waste streams that have been treated include pharmaceutical and biopharmaceutical waste streams (Johnston *et al.*, 1988), dinitrotoluene (DNT) process wastewater (Li *et al.*, 1993), brewery effluents, and polymer process effluents

(Schmieder and Abeln, 1999). SCWO has also been demonstrated on polychlorinated biphenyls (PCBs) (Staszak *et al.,* 1987), pesticides such as DDT (Modell *et al.,* 1982), and dioxins (Thomason *et al.,* 1990).

A promising application for SCWO is the treatment of hazardous chemical agents and propellants from the defense sector (Shaw *et al.*, 1993). In these cases, the ability to treat many different wastes with one contained process is clearly attractive. Economic constraints are minimal due to the great political pressure to be rid of these extremely hazardous wastes in an environmentally friendly manner, and this also benefits SCWO as a disposal alternative. These wastes encompass explosives, propellants, smokes, dyes, naval shipboard waste, and chemical weapons (including nerve agents and mustard gas). 32,000 tons of chemical weapons were slated for incineration by 2007, but because of public opposition to incinerators, the army was required to consider alternatives for their disposal. The National Research Council identified SCWO as a promising technology for the disposal of chemical weapons in 1993 (NRC, 1993). Since then, researchers have demonstrated the effectiveness of SCWO for destroying chemical warfare agents (Spritzer *et al.,* 1995; Snow *et al.,* 1996), propellants (Buelow, 1990), smokes and dyes (Rice *et al.,* 1994), and explosives (Harradine *et al.,* 1993). However, currently SCWO is primarily being considered as a secondary treatment for the effluent of a process whereby chemical agents are neutralized via caustic hydrolysis.

1.2.2 SCWO Process Description

A schematic of a general SCWO process with the MODAR reactor design is illustrated in Figure 1.4. The feed to the process is an aqueous stream (solution or slurry)

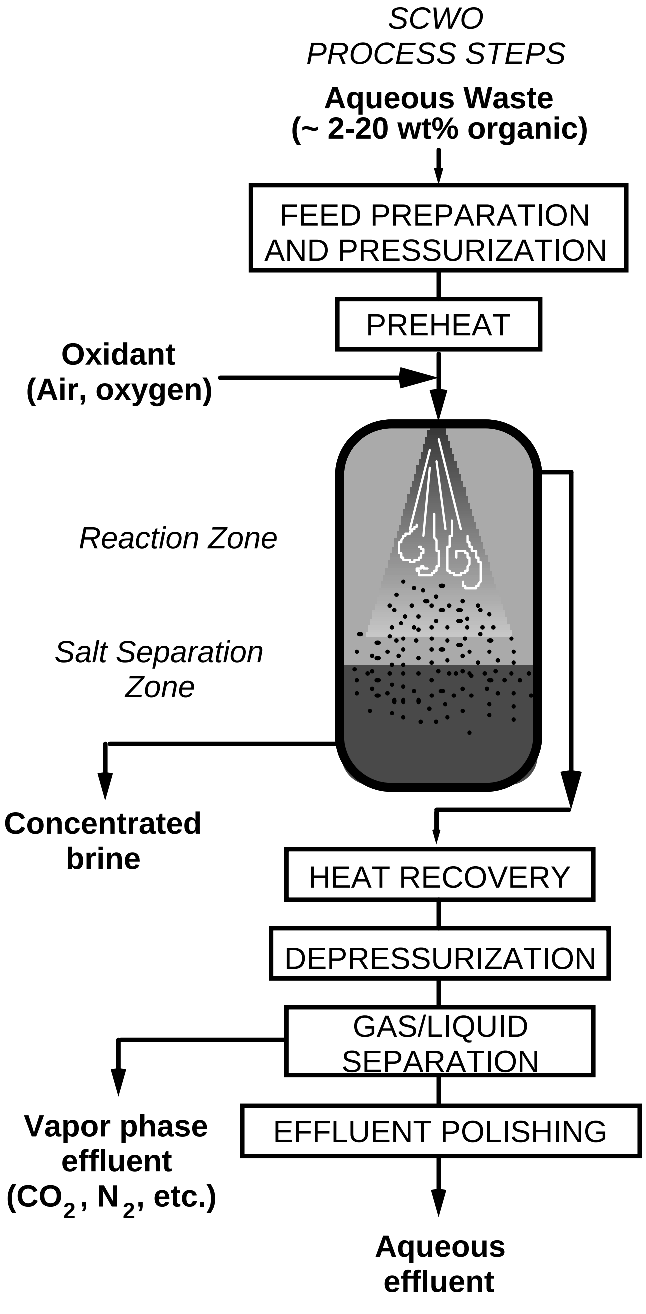

Figure 1.4: Schematic of the MODAR SCWO Reactor System

that is 1-20 wt% organics. Municipal and industrial waste streams may be fed directly to the process, whereas chemical agent streams are typically hydrolyzed in a caustic solution prior to entering the SCWO process. Fuels with high heating value are added to waste streams that are dilute or have low heating values. The feed is pressurized and preheated to a temperature between 400 and 500ºC, and a separate stream of oxidant is also pressurized and preheated. The oxidant may be air, oxygen, hydrogen peroxide, or even ammonium nitrate. The two streams are mixed at the reactor inlet where fast exothermic reactions increase the temperature to the final operating temperature of 600 to 650ºC.

Several reactor designs have been proposed for the commercialization of SCWO. In the MODAR design (illustrated in Figure 1.4), the oxidation reactions occur rapidly in the hot reaction zone in the top part of the reactor. The lower section of the reactor is a cool zone where liquid water dissolves any salts formed from the oxidation of compounds containing heteroatoms. The concentrated brine solution is removed from the lower section of the reactor, and the reaction product stream is removed from the top section. Other reactor designs include a tubular plug-flow reactor (Gloyna and Li, 1995), a transpiring wall reactor (Haroldsen *et al.*, 1996), and a hydrothermal burner (LaRoche *et al*, 1997).

The heat in the effluent of the reactor is recovered for use in the preheaters, and the solution is then depressurized. The gas-phase consists of primarily CO_2, N_2, and unreacted O_2 and may be vented to the atmosphere. The liquid effluent usually does not require further processing and may be released., Occasionally, however, suspended or dissolved solids containing metals in process effluents necessitate further effluent polishing prior to release.

1.2.3 Advantages and Technical Barriers

SCWO has several advantages over incineration, including: 1) complete containment allowing for product analysis prior to effluent release; 2) no production of NO_x or dioxin precursors; 3) can be self-sustaining for aqueous organic streams with modest heating values.

However, SCWO has several technical barriers that prevent its implementation industrially. Many of the typical aqueous waste streams contain organic compounds containing chlorine or other heteroatoms. Upon oxidation, these heteroatoms are oxidized to form acids that attack the reactor walls, resulting in severe corrosion problems. In order to reduce corrosion, caustic is fed to the reactor, effectively neutralizing the acid. Problematically, though, the salts produced by this neutralization process precipitate out of solution due to their low solubility in SCW, and stick to the reactor walls causing fouling and plugging. Minimization of the effects of these two technical barriers is essential to the deployment of SCWO technology for the remediation of hazardous waste.

Several process improvements have been proposed as solutions to these problems. Michael Modell, the inventor of SCWO, has proposed that proper pretreatment of the Nickel alloys that constitute the reactor walls (such as Inconel 625 or Hastelloy C-276) minimizes corrosion. This pretreatment involves flowing a dilute hydrogen peroxide solution at moderate temperature for several hours to form a passivated oxide layer on the surface of the metal. Furthermore, in his tubular reactor design, small metal wire brushes were occasionally passed through the preheater and reactor sections. In this manner, precipitated salts were removed, preventing plugging and minimizing corrosion. In a collaboration between Aerojet, Foster-Wheeler, and Sandia National Labs, a transpiring wall reactor has been designed and tested for SCWO (Haroldsen *et al.* 1996). This system involves a plenum in the reactor section where a thin layer of cool, liquid water is constantly flowing through pores in the walls, protecting the reactor from corrosion and dissolving any salts that precipitate in the SCW.

1.2.4 Current Status

SCWO is finding its way out of research laboratories and into pilot scale and industrial use in the United States, Europe, and Japan. A recent review article (Schmieder and Abeln 1999) covers some of the recent advances in each geographical region and a summary of the progress is presented below.

1.2.4.1 United States

In 1994, Eco Waste Technologies and the Huntsman Corporation built and began operating the first commercial SCWO facility. Their system utilizes a 200 m long tubular reactor that operates between 540 and 600ºC at 280 bar. The process is capable of handling 1100 kg/hr of waste with a nominal feed of 10 wt% organics and total organic carbon oxidation efficiencies greater than 99.9%. To date, the process has primarily operated on non-aggressive feedstocks of hydrocarbons, alcohols, and amines in this plant. Eco Waste also operates a pilot plant where aggressive feedstocks are treated successfully.

Several plants for the treatment of military wastes are in different stages of development. General Atomics has built a facility for the U.S. Air Force capable of handling 25,000 lbs/day of solid propellants. The U.S. Navy has tested two SCWO pilot plants for the disposal of shipboard waste. General Atomics built one of the reactors and the other was a transpiring wall reactor built by Foster Wheeler in collaboration with Sandia National Laboratories and Gencorp Aerojet. The Navy is investigating the feasibility of small SCWO facilities aboard its ships. The U.S. Army has contracted Foster Wheeler to design and build a disposal facility at Pine Bluff Arsenal in Arkansas for the disposal of 10,000 tons of smokes, dyes and pyrotechnics. The facility at Pine Bluff will treat 80 lbs/hr and will utilize a transpiring wall reactor. The Army is also building a pilot scale facility using the General Atomics reactor design for the treatment of VX nerve agent hydrolysate at Newport Chemical Agent Disposal Facility in Indiana. Additional testing is being conducted at Tooele Army Depot in Utah and at Aberdeen Proving Ground in Maryland on potential technologies (SCWO being one of several options) for disposal of assembled chemical weapons.

1.2.4.2 Europe

Several industrial facilities have implemented or plan to implement SCWO technology for the treatment of industrial waste. In a collaboration between Daimler-Chrysler and Fraunhofer Institute ITC, a mobile plant was built for the destruction of electronic scrap and for the recovery of high value metals. Chematur Engineering, AB of Sweeden has built a pilot plant for the treatment of sludge from a pulp and paper mill. The system uses the Eco Waste design and is capable of processing 250 kg/hr of waste. Further plans are underway to build a larger facility for the treatment of electronic scrap.

Additionally, Elf-Aquitaine is currently planning to build an SCWO pilot plant in collaboration with the University of Bordeaux. Several academic research groups are designing new reactor systems that specifically target applications for industrial waste streams.

1.2.4.3 Japan

The Organo Corporation has built the first SCWO processing plant in Japan. This plant will be used for the treatment of municipal sewage sludge in collaboration with the Japan Sewage Agency. Several other companies have license agreements and indicate plans to build SCWO treatment facilities. These companies include Hitachi, NGK, Komatsu and Kurita. Many other companies — including Kubota, Toshiba, Mitsubishi, and Sumitomo Heavy Industry — are actively pursuing research on SCWO, but their plans and progress are not available at this time.

1.3 Hydrothermal Chemistry

While supercritical water is primarily considered for oxidation of hazardous waste, subcritical water is an appealing medium for some organic syntheses and chemical transformations. With the dielectric strength ranging from 21.5 at 300ºC to 11.3 at 370ºC (P = 250 bar), subcritical water behaves like a moderately polar organic solvent. As a result, many organic molecules have high solubilities in subcritical water. Furthermore, the ion dissociation constant (K_w^*) of near-critical water (300-370ºC, 250 bar) is approximately 3 orders of magnitude greater than that of ambient water. Therefore, reactions that are either acid- or base-catalyzed may proceed without requiring the addition of extra acid or base. Hydrothermal chemistry refers to reactions that occur in high-pressure water and temperatures ranging from approximately 200 to 600°C. For the purposes of this thesis, hydrothermal chemistry is used to describe hydrolysis or other reactions that occur in the absence of oxygen.

1.3.1 Overview of Prior Research in Hydrothermal Water

In this section, some of the various chemistries explored in both sub- and supercritical water in the absence of oxygen will be discussed. This section is not intended to provide a complete review of all reactions in hot water but instead to provide a general overview and to discuss significant contributions in this field. For a more comprehensive review of organic reactions in sub- and supercritical water, several articles have been published (Katritzky *et al.,* 1996; Parsons, 1996; An *et al.,* 1997; Savage, 1999).

Near-critical water has been shown to function as a good medium for certain reactions that form carbon-carbon bonds. For example, Eckert and coworkers have demonstrated that Freidel-Crafts chemistry can be successfully performed in water at 275ºC in the absence of added catalysts (Chandler *et al.,* 1997). In traditional Freidel-Crafts syntheses, $AlCl_3$ is added to these reactions to generate acids that catalyze the reaction. The use of near-critical water as a replacement for $AlCl_3$ (in organic solvents) demonstrates the potential hydrothermal chemistry holds. Parsons and coworkers utilize near-critical and SCW for Heck arylation reaction (Diminnie *et al.*, 1995; Reardon *et al.*, 1995). The authors found that the alkenes needed for the Heck reactions could be synthesized in situ via elimination reactions from various starting materials. The Diels-Alder cycloaddition reaction was also studied with SCW as a solvent, and the authors reported that the Diels-Alder reactions proceeded rapidly with high yields of clean products (Korzenski and Kolis, 1997).

Kuhlman *et al.* (1994) have studied ring opening reactions of 2,5-dimethylfuran to produce 2,5-hexanedione in water at 250ºC. They concluded that the reaction was acid-catalyzed and that quantitative amounts of the product could be obtained. In another study, the same authors showed that several bicyclic diols underwent rearrangement to form their respective ketones in water at 275ºC (Kuhlmann *et al.,* 1994). The acid-catalyzed rearrangement reaction of cyclohexene to produce methylcyclopentene was reported by Parsons and coworkers (Crittendon and Parsons, 1994). The Beckmann rearrangement of cyclohexanone-oxime has also been shown proceed in sub- and supercritical water without added acid catalysts (Sato *et al.*, 1998).

Antal and coworkers have worked extensively with the acid-catalyzed dehydration of alcohols to form alkenes in near-critical water. Several of the alcohols studied include ethanol (Xu *et al.,* 1991), 1- and 2-propanol (Antal Jr. *et al.,* 1998), and tert-butanol (Xu *et al.,* 1997). Other elimination reactions such as the decarboxylation of organic acids in hydrothermal environments have also been studied. For example, citric acid rapidly reacts in water at 250ºC to form itaconic and citraconic acids (Carlsson *et al.,* 1994). At higher temperatures, itaconic acid undergoes decarboxylation to form methacrylic acid. Dehydrohalogenation reactions have also been performed in near-critical water on polyvinylchloride and other chlorinated organics (Katritzky *et al.,* 1996).

Hydrolysis reactions of many compounds have been studied in sub- and supercritical water. The reviews of An and Katrizky provide overviews of the various compounds studied in these hydrothermal environments (Katritzky *et al.*, 1996; An *et al.*, 1997). Most of these experiments were conducted to describe the chemistries that take place and not to obtain detailed kinetics of the reactions. Detailed kinetic studies have been performed on several classes of chemicals in both sub- and supercritical water, however. Iyer and Klein (1997) determined that the hydrolysis of butyronitrile was further catalyzed by the acidic product. Similar findings were reported for the hydrolysis of ethyl acrylate (Krammer and Vogel, 2000) and dibenzyl ether (Penninger *et al.*, 1999). Studies of hydrolysis reactions by our group at MIT are summarized in Section 1.4.1.

1.4 Overview of Previous Basic Research in SCWO Kinetics

While the effectiveness of SCWO for the treatment of hazardous waste has been demonstrated, accurate oxidation kinetics of individual compounds are necessary to properly model SCWO reactors. Many research groups throughout the world have useful data on the oxidation kinetics of individual compounds in SCWO. A summary of research contributions by the MIT group and by others in the US dealing with reaction kinetics in SCWO processes follows.

1.4.1 MIT Contributions

Oxidation kinetics studied at MIT have examined a wide array of model compounds. These model compounds were selected to either simulate real waste compounds of interest (*e.g.*, CH_2Cl_2 and benzene), or because they were refractory intermediates in the degradation of real waste compounds (CH_4, CO, and CH_3COOH). Global rate expressions that are assumed to be first-order in the concentration of the compound are typically reported and primary reaction pathways are determined. At a molecular level, elementary reaction models have been modified from combustion literature and applied to reactions in SCWO.

In the first study, the oxidation of carbon monoxide was studied from 420 to 570ºC at 246 bar and a first-order global rate expression was fit over the range (Helling and Tester, 1987; Helling and Tester, 1988; Holgate and Tester, 1994). The water-gas shift reaction was found to contribute significantly to the disappearance of CO. In another study, hydrogen oxidation was measured from 495 to 600ºC at 246 bar (Holgate and Tester, 1993; Holgate and Tester, 1994). An elementary reaction model was developed for the oxidation of both hydrogen and carbon monoxide (Holgate and Tester, 1994). Ammonia was studied at higher temperatures of 650 to 700ºC and showed only modest conversions of 0-15% at residence times of 10-15s (Helling and Tester, 1988; Webley *et al.,* 1991).

The rate of methanol oxidation has been measured in various different studies in our lab (Webley and Tester, 1989; Tester *et al.,* 1993; Phenix, 1997). The primary reaction products were CO, CO_2, H_2, and CH_2O. A global rate expression was determined over the temperature range of 450 to 550ºC and the oxidation was highly activated. Preliminary experiments on the oxidation of ethanol were conducted and the products were CO, CO_2, and acetaldehyde (Helling and Tester, 1988). A more complete study was performed recently and a global rate expression was determined (unpublished at this time).

The oxidation of methane was studied from 560 to 650ºC at 246 bar and produced CO and CO_2 (Webley and Tester, 1991). Evidence of hydrolysis was not observed, nor were catalytic effects seen. Benzene oxidation kinetics were experimentally measured from 450 to 600ºC (DiNaro, 1999; DiNaro *et al.*, 2000b). Conversion was minimal below 520ºC and hydrolysis reactions were minimal over the entire temperature range. The primary oxidation products were CO, CO_2, methane, and phenol. An elementary reaction model was developed which represented the system well (DiNaro *et al.*, 2000a). The reaction model provided an explanation for early appearance of CO_2 in the reaction.

The oxidation of acetic acid was measured from 425 to 600ºC and 160 to 263 bar (Meyer *et al.*, 1995). The reaction rate was 0.72 order in acetic acid and unaffected by changes in pressure. The primary products of oxidation were CO, CO_2, and methane. The hydrolysis and oxidation of glucose were studied from 425 to 600ºC (Holgate *et al.*, 1995). Complete conversion of glucose was seen in 6 s at 600ºC, even in the absence of oxygen. The primary products of hydrolysis were CO, CO_2, CH_4, C_2H_4, C_2H_6, acetaldehyde (CH_3CHO), acetic acid (CH_3COOH), acetonylacetone ($CH_3COC_2H_4COCH_3$), and propenoic acid (C_2H_5COOH).

The hydrolysis and oxidation of methylene chloride was studied from ambient to 600ºC . CH_2Cl_2 was found to hydrolyze under subcritical hydrothermal conditions from 200 to 400°C, producing HCl and CH_2O (Marrone *et al.*, 1998). Since most of the hydrolysis occurred in the non-isothermal section of the preheater, a temperature profile was determined. Using this profile, a hydrolysis rate expression was regressed for the entire temperature range. A Kirkwood approximation was employed to model the solvation effects as the physical properties of water changed from ambient to supercritical conditions (Marrone *et al.*, 1998).

Thiodiglycol was studied for both hydrolysis and oxidation from 200 to 525ºC (Lachance, 1995; Lachance *et al.*, 1999). Thiodyglycol was found to hydrolyze at temperatures greater than 300°C, producing C_2H_4, acetaldehyde, and H_2S. Additional products were seen in the oxidation experiments including CO, CO_2, methane, formic acid, acetic acid, and elemental sulfur.

1.4.2 Extramural Studies

Professor Savage and coworkers have studied the oxidation kinetics of various compounds in SCWO. Global rate expressions have been developed for phenol (Thornton and Savage, 1990), 2-chlorophenol (Li *et al.*, 1993), CH_3- and CHO substituted phenols (Martino and Savage, 1997), acetic acid (Savage and Smith, 1995), and methanol (Brock *et al.*, 1996). Savage *et al.* have also used elementary reaction models to describe the oxidation of methanol, methane, CO, H_2 (Brock and Savage, 1995), and phenol (Gopalan and Savage, 1995).

A group at Sandia National Laboratories led by Steve Rice has studied both overall destruction efficiencies of hazardous wastes as well as detailed kinetic measurements. In one detailed kinetic study, Raman spectroscopy was used to monitor methane oxidation in SCW (Steeper *et al.*, 1996). In another study, formaldehyde was found as the primary, metastable intermediate in methanol oxidation (Rice *et al.*, 1996). A comparison of the oxidation kinetics of n-propanol and i-propanol revealed that n-propanol reacted faster (Hunter *et al.*, 1996). Finally, hydrogen peroxide decomposition was measured in supercritical water (Croiset *et al.*, 1997).

Gloyna *et al.* have studied the kinetics of a wide array of compounds under SCWO conditions. Some of the compounds studied include phenol (Li *et al.*, 1997), n-octanol (Li *et al.*, 1997), pyridine (Crain *et al.*, 1993), dimethyl methylphosphonate (McKendry *et al.*, 1994), dinitrotoluene (Li *et al.*, 1993), acetamide (Lee and Gloyna, 1992), 2,4-dichlorophenol (Lee *et al.,* 1990), and acetic acid (Li *et al.,* 1997). Gloyna *et al.* (1994) have studied many other areas of engineering as it relates to SCWO.

Buelow and coworkers at Los Alamos National Laboratory have studied the primary oxidation pathways of explosives, propellants (Harradine *et al.*, 1993), and chlorinated hydrocarbons (Foy *et al.,* 1996). In one study, they used *in situ* Raman spectroscopy to measure the oxidation of hydrazine (Masten *et al.*, 1993). Other studies have aimed at the effectiveness of alternative oxidants, such as nitrates and nitrites, on the oxidation of methanol, acetic acid, EDTA, and phenol (Proesmans *et al.*, 1997).

At the University of Delaware, Klein and coworkers have studied the oxidation of nitroanilines (Wang *et al.,* 1995), 1-nitrobutane (Iyer *et al.,* 1996), and butyronitrile (Iyer and Klein, 1997) in SCW. Lumped models have also been developed for C1-C3 alcohols and acetic acid (Boock and Klein, 1993). Also at Delaware, Brill and coworkers have used spectroscopic measurement techniques to measure the oxidation of urea (Kieke *et al.,* 1996), ethylenediammonium nitrate (Maiella and Brill, 1996), guanidinium nitrate (Schoppelrei *et al.,* 1996), and malonic acid (Maiella and Brill, 1996).

Finally, although they do not explicitly report oxidation kinetics parameters, Johnston and coworkers at University of Texas have been significant contributors to the understanding of reactions in SCWO. A small subset of their investigations includes the use of molecular simulations to predict the free energy of solvation for Cl^-, OH^-, Na^+, and HCl (Balbuena *et al.*, 1996), and the prediction of the local density of SCW around Li^+, Na^+, K^+, F^-, Cl^-, Be^{2+}, Mg^{2+}, and Ca^{2+} using a dielectric concentric shell model (Flanagin *et al.,* 1997). Johnston and coworkers have also measured pH and acid dissociation in sub- and supercritical water (Xiang *et al.*, 1996).

1.5 References

An, J. Y., L. Bagnell, T. Cablewski, C. R. Strauss, and R. W. Trainor (1997). "Applications of high-temperature aqueous media for synthetic organic reactions." *Journal of Organic Chemistry* **62** (8): 2505.

Antal Jr., M. J., M. Carlsson, X. Xu, and D. G. M. Anderson (1998). "Mechanism and kinetics of the acid-catalyzed dehydration of 1- and 2-propanol in hot compressed liquid water." *Industrial & Engineering Chemistry Research* **37** (10): 3820.

Balbuena, P. B., K. P. Johnston, and P. J. Rossky (1996). "Molecular dynamics simulation of electrolyte solutions in ambient and supercritical water. 1. Ion solvation." *Journal of Physical Chemistry* **100** (7): 2706.

Bandura, A. V. and S. N. Lvov (2000). "The ionization constants of water over a wide range of temperatures and densities." in *Steam, water, and hydrothermal systems: Physics and chemistry meeting the needs of industry*. P. R. Tremaine, P. G. Hill, D. E. Irish and P. V. Palakrishnan. Ottawa, NRC Press.

Boock, L. T. and M. T. Klein (1993). "Lumping strategy for modeling the oxidation of C1-C3 alcohols and acetic acid in high-temperature water." *Industrial & Engineering Chemistry Research* **32**: 2464.

Brock, E. E., Y. Oshima, P. E. Savage, and J. R. Barker (1996). "Kinetics and mechanism of methanol oxidation in supercritical water." *Journal of Physical Chemistry* **100** (39): 15834.

Brock, E. E. and P. E. Savage (1995). "Detailed chemical kinetics model for supercritical water oxidation of C1 compounds and H2." *AIChE Journal* **41** (8): 1874.

Buelow, S. J. (1990). Destruction of propellant components in supercritical water. Los Alamos, NM, Los Alamos National Laboratory.

Carlsson, M., C. Habenicht, L. C. Kam, M. J. Antal, N. Y. Bian, R. J. Cunningham, and M. Jones (1994). "Study of the sequential conversion of citric to itaconic to methacrylic-acid in near-critical and supercritical water." *Industrial & Engineering Chemistry Research* **33** (8): 1989.

Chandler, K., F. Deng, A. K. Dillow, C. L. Liotta, and C. A. Eckert (1997). "Alkylation reactions in near-critical water in the absence of acid catalysts." *Industrial & Engineering Chemistry Research* **36** (12): 5175.

Cooper, S. P., H. G. Folster, S. A. Gairns, and E. G. Hauptmann (1997). "Treatment of lagoon sludge, primary clarifier sludge, and bleach plant effluent by supercritical water oxidation." *Pulp & Paper-Canada* **98** (10): 37.

Crain, N., S. Tebbal, L. Li, and E. F. Gloyna (1993). “Kinetics and reaction pathways of pyridine oxidation in supercritical water.” *Industrial & Engineering Chemistry Research* **32** (10): 2259.

Crittendon, R. C. and E. J. Parsons (1994). “Transformations of cyclohexane derivatives in supercritical water.” *Organometallics* **1994** (13): 7.

Croiset, E., S. F. Rice, and R. G. Hanush (1997). “Hydrogen peroxide decomposition in supercritical water.” *AIChE Journal* **43** (9): 2343.

DeSimone, J. D., Z. Guan, and C. S. Elsbernd (1992). “Synthesis of fluouropolymers in supercritical carbon dioxide.” *Science* **257** (5072): 945.

Diminnie, J., S. Metts, and E. J. Parsons (1995). “In-situ generation and Heck coupling of alkenes in superheated water.” *Organometallics* **14** (8): 4023.

DiNaro, J. L. (1999). "Oxidation of benzene in supercritical water: Experimental measurement and development of an elementary reaction mechanism." Ph.D. Thesis, Department of Chemical Engineering, MIT. Cambridge, MA.

DiNaro, J. L., J. B. Howard, W. H. Green, J. W. Tester, and J. W. Bozzelli (2000a). "Elementary reaction mechanism for benzene oxidation in supercritical water." *Journal of Physical Chemistry A* **104** (45): 10576.

DiNaro, J. L., J. W. Tester, J. B. Howard, and K. C. Swallow (2000b). "Experimental measurements of benzene oxidation in supercritical water." *AIChE Journal* **46** (11): 2274.

Flanagin, L. W., P. B. Balbuena, K. P. Johnston, and P. J. Rossky (1997). “Ion solvation in supercritical water based on an adsorption analogy.” *Journal of Physical Chemistry* **101** (40): 7998.

Foy, B. R., K. Waldthausen, M. A. Sedillo, and S. J. Buelow (1996). “Hydrothermal processing of chlorinated hydrocarbons in a titanium reactor.” *Environmental Science and Technology* **30** (9): 2790.

Gloyna, E. F., L. Li, and R. N. McBrayer (1994). “Engineering aspects of supercritical water oxidation.” *Water Science Technology* **30** (9): 1.

Gloyna, E. F. and L. X. Li (1995). “Supercritical water oxidation research and development update.” *Environmental Progress* **14** (3): 182.

Gopalan, S. and P. E. Savage (1995). “A reaction network model for phenol oxidation in supercritical water.” *AIChE Journal* **41** (8): 1864.

Goto, M., T. Nada, A. Ogata, A. Kodama, and T. Hirose (1998). “Supercritical water oxidation for the destruction of municipal excess sludge and alcohol distillery wastewater of molasses.” *Journal of Supercritical Fluids* **13**: 277.

Haar, C., J. S. Gallagher, and G. S. Kell (1984). *NBS/NRC Steam Tables*. Hemisphere Publishing Corp., Washignton, D. C.

Haroldsen, B. L., D. Y. Ariizumi, B. E. Mills, B. G. Brown, and D. Greisen (1996). "Transpiring wall supercritical water oxidation test reactor design report." Report No. SAND96-8255, Sandia National Laboratories, Livermore, CA.

Harradine, D. M., S. J. Buelow, P. C. DellOrco, R. B. Dyer, B. R. Foy, J. M. Robinson, J. A. Sanchez, T. Spontarelli, and J. D. Wander (1993). “Oxidation chemistry of energetic materials in supercritical water.” *Hazardous Waste and Hazardous Materials* **10** (2): 233.

Helling, R. K. and J. W. Tester (1987). “Oxidation kinetics of carbon monoxide in supercritical water.” *Energy & Fuels* **1**: 417.

Helling, R. K. and J. W. Tester (1988). “Oxidation of simple organic compounds and mixtures in supercritical water: Carbon monoxide, ammonia, and ethanol.” *Environmental Science and Technology* **22** (11): 1319.

Holgate, H. R., J. C. Meyer, and J. W. Tester (1995). “Glucose hydrolysis and oxidation in supercritical water.” *AIChE Journal* **41** (3): 637.

Holgate, H. R. and J. W. Tester (1993). “Fundamental kinetics and mechanisms of hydrogen oxidation in supercritical water.” *Combustion Science and Technology* **88**: 369.

Holgate, H. R. and J. W. Tester (1994). “Oxidation of hydrogen and carbon monoxide in sub- and supercritical water: Reaction kinetics, pathways, and water-density effects. 1. Experimental results.” *Journal of Physical Chemistry* **98**: 800.

Holgate, H. R. and J. W. Tester (1994). “Oxidation of hydrogen and carbon monoxide in sub- and supercritical water: Reaction kinetics, pathways, and water-density effects. 2. Elementary reaction modeling.” *Journal of Physical Chemistry* **98**: 810.

Hong, G. T., P. K. Fowler, W. R. Killilea, and K. C. Swallow (1987). "Supercritical water oxidation: treatment of human waste and system configuration tradeoff study." SAE Technical Series Paper #871444, 17th Intersociety Conference on Environmental Systems, Seattle, WA.

Hong, G. T., W. R. Killilea, and T. B. Thomason (1988). "Supercritical water oxidation: space applications." ASCE Space '88 Proceedings, Albuquerque, NM, August 29-31.

Hunter, T. B., S. F. Rice, and R. G. Hanush (1996). “Raman spectroscopic measurement of oxidation in supercritical water. 2. Conversion of isopropyl alcohol to acetone.” *Industrial & Engineering Chemistry Research* **35** (11): 3984.

Iyer, S. D. and M. T. Klein (1997). “Effects of pressure on the rate of butyronitrile hydrolysis in high-temperature water.” *Journal of Supercritical Fluids* **10**: 191.

Iyer, S. D., G. R. Nicol, and M. T. Klein (1996). “Hydrothermal reactions of 1-nitrobutane in high temperature water.” *Journal of Supercritical Fluids* **9**: 26.

Johnston, J. B., R. E. Hannah, V. L. Cunningham, B. P. Daggy, F. J. Sturm, and R. M. Kelly (1988). “Destruction of pharmaceutical and biopharmaceutical wastes by the MODAR supercritical water oxidation process.” *Biotechnology* **6** (12): 1423.

Kalinichev, A. G. and J. D. Bass (1997). “Hydrogen bonding in supercritical water 2. Computer simulations.” *Journal of Physical Chemistry A* **101** (50): 9720.

Katritzky, A. R., S. M. Allin, and M. Siskin (1996). “Aquathermolysis: Reactions of organic compounds with superheated water.” *Accounts of Chemical Research* **29** (8): 399.

Kieke, M. L., J. W. Schoppelrei, and T. B. Brill (1996). “Spectroscopy of hydrothermal reactions. 1. The CO_2-H_2O system and kinetics of urea decomposition in an FTIR spectroscopy flow reactor cell operable to 725 K and 335 bar.” *Journal of Physical Chemistry* **100**: 7455.

Killilea, W. R. and K. C. Swallow (1992). “The fate of nitrogen in supercritical water oxidation.” *Jounal of Supercritical Fluids* **5** (1): 72.

Korzenski, M. B. and J. W. Kolis (1997). “Diels-Alder reactions using supercritical water as an aqueous solvent medium.” *Tetrahedron Letters* **38** (32): 5611.

Krammer, P. and H. Vogel (2000). “Hydrolysis of esters in subcritical and supercritical water.” *Journal of Supercritical Fluids* **16**: 189-206.

Kuhlmann, B., E. M. Arnett, and M. Siskin (1994). “Classical organic reactions in pure superheated water.” *Journal of Organic Chemistry* **59** (11): 3098.

Kuhlmann, B., E. M. Arnett, and M. Siskin (1994). “H-D exchange in pinacolone by deuterium-oxide at high-temperature and pressure.” *Journal of Organic Chemistry* **59** (18): 5377.

Lachance, R. P. (1995). "Oxidation and hydrolysis reactions in supercritical water: chlorinated hydrocarbons and organosulfur compounds." Master's Thesis, Department of Chemical Engineering, MIT. Cambridge, MA.

Lachance, R. P., J. Paschkewitz, J. L. DiNaro, and J. W. Tester (1999). “Thiodiglycol hydrolysis and oxidation in sub- and supercritical water.” *Journal of Supercritical Fluids* **16** (2): 133.

LaRoche, H. L., M. Weber, and C. Trepp (1997). “Design rules for the wall-cooled hydrothermal burner (WHB).” *Chemical Engineering & Technology* **20** (3): 208.

Lee, D. S. and E. F. Gloyna (1992). "Hydrolysis and oxidation of acetamide in supercritical water." *Environmental Science and Technology* **26** (8): 1587.

Li, L., P. Chen, and E. F. Gloyna (1997). "Pilot-plant validation of kinetic models for supercritical water oxidation." *Chemical Oxidation* **4**: 219.

Li, L., E. F. Gloyna, and J. E. Sawicki (1993). "Treatability of DNT process wastewater by supercritical water oxidation." *Water Environamental Research* **65**: 250.

Li, R., P. E. Savage, D. Szmukler (1993). "2-chlorophenol oxidation in supercritical water: Global kinetics and reaction products." *AIChE Journal* **39** (1): 178.

Maiella, P. G. and T. B. Brill (1996). "Spectroscopy of hydrothermal reactions. 3. The water-gas reaction, 'hot spots', and formation of volatile salts of NCO- from aqueous $[NH_3(CH_2)_nNH_3]NO_3$ (n = 2,3) at 720 K and 276 bar by T-jump/FTIR spectroscopy." *Applied Spectroscopy* **50**: 829.

Maiella, P. G. and T. B. Brill (1996). "Spectroscopy of hydrothermal reactions. 5. Decarboxylation of malonic acid and monosodium malonate." *Journal of Physical Chemistry* **100**: 14352.

Marrone, P. A., P. M. Gschwend, et al. (1998). "Product distribution and reaction pathways for methylene chloride hydrolysis and oxidation under hydrothermal conditions." *Journal of Supercritical Fluids* **12** (3): 239.

Marrone, P. A., P. M. Gschwend, K. C. Swallow, W. A. Peters, and J. W. Tester (1998). "Solvation effects on kinetics of methylene chloride reactions in sub and supercritical water: Theory, experiment, and ab initio calculations." *Journal of Physical Chemistry A.* **102**(35): 7013-7028.

Marshall, W. L. and E. U. Franck (1981). "Ion product of water substance, 0-1000°C 1-10,000 bars. New international formulation and its background." *Journal of Physical Chemistry Reference Data* **94** (2): 295-304.

Martino, C. J. and P. E. Savage (1997). "Supercritical water oxidation kinetics, products, and pathways for CH_3- and CHO- substituted phenols." *Industrial & Engineering Chemistry Research* **36** (5): 1391.

Masten, D. A., B. R. Foy, D. M. Harradine, and R. B. Dyer (1993). "*In situ* Raman spectroscopy of reactions in supercritical water." *Journal of Physical Chemistry* **97** (33): 8557.

McHugh, M. A. and V. J. Krukonis (1986). *Supercritical Fluid Extraction: Principles and Practice*. Butterworth Publishers, Stoneham, MA.

McKendry, J. K., L. Li, and E. F. Gloyna (1994). "The effect of additives on the oxidation of dimethyl methylphosphonate in supercritical water." *Proceedings of the Industrial Waste Conference* **49**: 365.

Meyer, J. C., P. A. Marrone, and J. W. Tester (1995). “Acetic acid oxidation and hydrolysis in supercritical water.” *AIChE Journal* **41** (9): 2108.

Modell, M. (1989). "Supercritical water oxidation." in *Standard Handbook of Hazardous Waste Treatment and Disposal*. H. M. Freeman, Ed., McGraw-Hill**:** 8.153, New York, NY.

Modell, M. (1995). "Supercritical Water Oxidation of Aqueous Wastes." 56th Annual International Water Conference, Pittsburgh, PA.

Modell, M., G. G. Gaudet, M. Simson, G. T. Hong, and K. Biemann (1982). “Supercritical water: testing reveals new process holds promise.” *Solids Waste Management*.

Modell, M., J. Larson, and S. F. Sobczynski (1992). “Supercritical water oxidation of pulp mill sludges.” *Tappi Journal* 195.

NRC (1993). "Alternative technologies for the destruction of chemical agents and munitions." National Research Council, Washington, D. C.

Parsons, E. J. (1996). “Organic reactions in very hot water.” *CHEMTECH* **26** (6): 30.

Penninger, J. M. L., R. J. A. Kersten, and H. C. L. Baur (1999). “Hydrolysis of diphenylether in supercritical water: Effects of dissolved NaCl.” *Journal of Supercritical Fluids* **17**: 215-226.

Phenix, B. D. (1997). "Hydrothermal oxidation of simple organic compounds." Ph.D. Thesis, Department of Chemical Engineering, MIT. Cambridge, MA.

Proesmans, P. I., L. Luan, and S. J. Buelow (1997). “Hydrothermal oxidation of organic wastes using ammonium nitrate.” *Industrial & Engineering Chemistry Research* **36**: 1559.

Reardon, P., S. Metts, C. Crittendon, P. Daugherity, and E. J. Parsons(1995). “Palladium-catalyzed coupling reactions in superheated water.” *Organometallics* **14** (8): 3810.

Rice, S. F., T. B. Hunter, A. C. Ryden, and R. G. Hanush (1996). “Raman spectroscopic measurement of oxidation in supercritical water: 1. Conversion of methanol to formaldehyde.” *Industrial & Engineering Chemistry Research* **35** (7): 2161.

Rice, S. F., C. A. LaJeunesse, R. G. Hanush, J. D. Aiken, and S. C. Johnston (1994). "Supercritical water oxidation of colored smoke, dye, and pyrotechnic compositions." Report No. SAND94-8209, Sandia National Laboratories. Livermore, CA.

Sato, O., Y. Ikushima, and T. Yokoyama (1998). “Noncatalytic Beckmann rearrangement of cyclohexanone-oxime in supercritical water.” *Journal of Organic Chemistry* **63**: 9100.

Savage, P. E. (1999). “Organic reactions in supercritical water.” *Chemical Reviews* **99** (2): 603.

Savage, P. E. and M. A. Smith (1995). “Kinetics of acetic acid oxidation in supercritical water.” *Environmental Science and Technology* **29** (1): 216.

Schmieder, H. and J. Abeln (1999). “Supercritical water oxidation: State of the art.” *Chemical Engineering Technology* **22** (11): 903.

Schoppelrei, J. W., M. L. Kieke, X. Wang, M. T. Klein, and T. B. Brill (1996). “Spectroscopy of hydrothermal reaction. 4. Kinetics of urea and guanidinium nitrate at 200-300ºC in a diamond cell, infrared spectroscopy flow reactor.” *Journal of Physical Chemistry* **100**: 14343.

Shanableh, A. and E. F. Gloyna (1991). “Supercritical water oxidation - wastewater and sludges.” *Water Science Technology* **23**: 389.

Shaw, R. W., T. B. Brill, A. A. Clifford, C. A. Eckert, and E. U. Franck (1991). "Supercritical water: a medium for chemistry." *Chemical Engineering News* **69** (51): 26.

Snow, R. H., W. Sabato, K. Taylor, G. C. Sresty, K. Downey, D. Hazelbeck, and D. Jensen (1996). "Demilitarization of chemical agents by hydrolysis and supercritical water oxidation." *Proceedings of ERDEC Scientific Conference on Chemical and Biological Defense Research* : 359.

Spritzer, M. H., D. A. Hazelbeck, and K. W. Downey (1995). “Supercritical waster oxidation of chemical agents and solid propellants.” *Journal of Energetic Materials* **13**: 185.

Squires, T. G., C. G. Venier, and T. Aida (1983). “Supercritical fluid solvents in organic chemistry.” *Fluid Phase Equilibria* **10**: 261.

Staszak, C. N., K. C. Malinowski, and W. R. Killilea (1987). “The pilot-scale demonstration of the MODAR oxidation process for the destruction of hazardous waste materials.” *Environmental Progress* **6** (1): 39.

Steeper, R. R., S. F. Rice, et al. (1996). “Kinetics measurements of methane oxidation in supercritical water.” *Journal of Physical Chemistry* **100** (1): 184.

Tester, J. W., H. R. Holgate, F. J. Armellini, P. A. Webley, W. R. Killilea, G. T. Hong, and H. E. Barner (1993). "Supercritical water oxidation technology: A review of process development and fundamental research." in *Emerging technologies for* *hazardous waste management III*. D. W. Tedder and F. G. Pohland, Eds. American Chemical Society, **518:** Chapter 3, Washington, D. C.

Tester, J. W. and M. Modell (1996). *Thermodynamics and Its Applications*. Prentice Hall PTR, Upper Saddle, NJ.

Tester, J. W., P. A. Webley, and H. R. Holgate (1993). "Revised global kinetic measurements of methanol oxidation in supercritical water." *Industrial & Engineering Chemistry Research* **32** (1): 236.

Thomason, T. B., G. T. Hong, K. C. Swallow, and W. R. Killilea (1990). "The MODAR supercritical water oxidation process." in *Innovative Hazardous Waste Treatment Technology Series, Volume 1: Thermal Processes*. H. M. Freeman, Ed. Technomic Publishing**:** 31, Lancaster, PA.

Thornton, T. D. and P. E. Savage (1990). "Phenol oxidation in supercritical water." *Journal of Supercritical Fluids* **3**: 240.

Uematsu, M. and E. U. Franck (1980). "Static dielectric constant of water and steam." *The Journal of Physical Chemical Reference Data* **9** (4): 1291.

Villard, P. (1896). "Solubility of liquids and solids in gas." *Journal of Physics* **5**: 455.

Wang, X. G., L. U. Gron, M. T. Gron, and T. B. Brill (1995). "The influence of high-temperature water on the reaction pathways of nitroanilines." *Journal of Supercritical Fluids* **8**: 236.

Weast, R. C. (1975). *Handbook of Chemistry and Physics*. CRC Press Cleveland, OH.

Webley, P. A. and J. W. Tester (1989). "Fundamental kinetics of methanol oxidation in supercritical water." in *Supercritical Fluid Science and Technology,* K. P. Johnston and J. M. L. Penninger, Eds. ACS Symposium Series, **406**. American Chemical Society, Washington, D.C. 259.

Webley, P. A. and J. W. Tester (1991). "Fundamental kinetics of methane oxidation in supercritical water." *Energy & Fuels* **5**: 411.

Webley, P. A., J. W. Tester, and H. R. Holgate (1991). "Oxidation kinetics of ammonia and ammonia-methanol mixtures in supercritical water in the temperature range 530 to 700ºC at 246 bar." *Industrial & Engineering Chemistry Research* **30** (8): 1745.

Weinstein, R. D., A. R. Renslo, R. L. Danheiser, J. G. Harris, and J. W. Tester (1996). "Kinetic Correlation of Diels-Alder Reactions in Supercritical Carbon Dioxide." *The Journal of Physical Chemistry* **100** (30): 12337.

Xiang, T., K. P. Johnston, W. T. Wofford, and E. F. Gloyna (1996). "Spectroscopic measurement of pH in aqueous sulfuric acid and ammonia from sub- to supercritical conditions." *Industrial & Engineering Chemistry Research* **35**: 4788.

Xu, X., M. J. Antal Jr., and D. G. M. Anderson (1997). "Mechanism and temperature-dependent kinetics of the dehydration of tert-butyl alcohol in hot compressed liquid water." *Industrial & Engineering Chemistry Research* **36** (1): 23.

Xu, X., C. P. De Almeida, and M. J. Antal (1991). "Mechanism and kinetics of the acid-catalyzed formation of ethene and diethyl ether from ethanol in supercritical water." *Industrial & Engineering Chemistry Research* **30**: 1478-1485.

Chapter 2

Objectives and Approach

The overall objective of this thesis is to provide a better understanding of the reaction pathways and rates that occur in sub- and supercritical water from 100°C to 600°C at pressures from the vapor pressure to 250 bar. This objective was accomplished by combining experimental measurements under well-defined conditions with molecular level insights from modeling. Two representative model compounds (CH_2Cl_2 and MTBE) were selected for this study. In each study, emphasis was placed on determining the role that water played in the reaction mechanism. Our hope was to use a fundamental understanding of their reaction pathways as a means for predicting the behavior of larger classes of organic compounds.

The specific approaches taken to achieve these objectives were as follows:

Kinetic Measurements and Analysis of Mechanisms:

1) *Measure the isothermal rate of methylene chloride hydrolysis in sub- and supercritical water.* Chlorinated organics, such as methylene chloride, are common solvents in chemical processes and are therefore present in many waste streams. Methylene chloride has previously been studied in our research group as a model chlorinated organic, and an empirical expression for the hydrolysis rate was determined. However, this correlation was based on conversion measurements at the end of a preheater and reactor system. In the preheater, the temperature increased

from ambient to supercritical temperatures and the temperature profile was estimated using a heat transfer model.

In this study, the goal was to precisely measure the hydrolysis rate at well-defined isothermal conditions. The first step was to design and build an apparatus that would allow us to perform isothermal hydrolysis experiments. The second step was to collect data on the hydrolysis rate of methylene chloride at different temperatures. Additionally, experiments were conducted to determine the effect of metal surfaces on the reaction rate. The complete study is described in detail in Chapter 4 of this thesis.

2) *Measure the hydrolysis rate of methyl tert-butyl ether (MTBE) in sub- and supercritical water.* Ethers represent a class of chemicals used widely as solvents, which are therefore common in organic waste streams. Yet very little is known about the chemistry of ethers in hydrothermal environments. MTBE, a common gasoline additive, has received significant attention as an environmental contaminant caused primarily by leaking underground storage tanks. This research aimed, then, to study the hydrolysis of MTBE in sub- and supercritical water not only as a model of ether behavior, but also as a potential remediation technology for contaminated groundwater. To reach this objective, the rate of MTBE decomposition was measured as a function of temperature (and time) at 250 bar. The complete study of experimental measurements is described in Chapter 5.

3) *Probe the reaction pathways of MTBE in sub- and supercritical water.* In addition to simply measuring the rate of disappearance of MTBE, a fundamental understanding of the reaction chemistry is necessary in order to apply the knowledge obtained in this

study to the broader class of ethers. To understand the reaction chemistry, experiments were designed and implemented to elucidate the individual reaction steps in the overall mechanism. The objective of this study was to determine the factors that affect the reaction rate and mechanistic pathways of MTBE hydrolysis.

The approach to probing the reaction pathways was first to determine the role that water plays in the mechanism. It was important determine whether water plays an active role in the reaction (as a reactant or catalyst) or simply provides the medium in which the reaction takes place. Therefore, reactions were conducted in the presence of added species — such as acids or bases — to determine the effects caused by changes in the concentrations of H^+ or OH^-. These experiments are described in greater detail in Chapter 6.

Molecular Modeling Studies:

4) *Model the hydrolysis of* CH_2Cl_2*, correcting for solvent effects on the reaction rate.* The rate-limiting-step in the reaction mechanism for methylene chloride hydrolysis involves nucleophilic substitution of a water molecule for a chloride group. In the previous study in our group, the effect of water solvation of the reactant and transition state was found to change the effective activation energy of this step. *Ab initio* tools were used and a Kirkwood approximation was determined to correct the activation energy as the solvent properties varied from 100 to 500°C. The goal for this study was to fit an empirical rate expression to the data below 250°C (where the correction is minimal) and then apply the Kirkwood correction to model the experimentally observed rate over the entire temperature range.

5) *Determine the mechanism of MTBE hydrolysis and model the reaction rate.* To model the hydrolysis of MTBE, it was necessary to determine the contribution of various reaction pathways over the entire temperature domain. *Ab initio* tools were employed to correct for solvation effects on a gas-phase, unimolecular decompostion pathway. Additionally, an acid-catalyzed reaction mechanism was proposed. The goal of this study was to determine the relative importance of each pathway over the entire temperature domain. The results of this study are reported in Chapter 6.

Diagnostic Equipment and Technique Development:

6) *Design and construct a new "state-of-the-art" SCWO reactor system.* Because the experimental systems in the laboratory each have certain limitations, we planned to expand our capabilities with a new reactor. The design and construction of this reactor was undertaken to provide several advantages: 1) A large inner diameter to eliminate possible surface effects due to wall catalysis or radical quenching; 2) Sapphire windows were installed to allow optical access for in situ spectroscopic and other measurements of fluid composition and properties without the need to quench and sample; 3) A large internal volume with a movable probe to permit sampling over a wide range of residence times. Complete details of the system, as well as the conditions used for initial testing, are described in Chapter 7.

7) *Develop in situ Raman spectroscopy methods.* Historically, all composition measurements in our group have been conducted by quenching the reaction, depressurizing the reactor or its products, and then analyzing the ambient effluent. With these steps, however, some species that are stable at high temperatures and

pressures, but become unstable at ambient conditions, may undergo further reaction during the quenching and depressurizing stage. Additionally, phase separation during the quenching process may inhibit the ability to accurately measure all species produced in the reactor, especially when very small amounts of gas are produced. Therefore, we intended to implement Raman spectroscopy as an in situ diagnostic tool for composition measurements in supercritical fluids. With *in situ* measurements, stable reaction intermediates as well as reactants and final products can be identified. Such information will provide time-resolved information on the progress of the reactions occurring that could help us understand the reaction mechanism. Such detailed information cannot be determined via ‘quench and analyze’ techniques.

On a more fundamental level, there is currently no good model for reaction dynamics in supercritical fluids. Since a supercritical fluid is neither a gas nor a liquid, the kinetic models established for these phases are not directly applicable. Therefore, tools that probe molecular-level processes, such as Raman spectroscopy, are essential to developing a proper fundamental understanding of reactions in supercritical fluids.

Our plan was first to develop measurement capabilities in a supercritical CO_2 system using a small, optically accessible cell that could be interfaced directly into the Raman apparatus. Once the cell was designed, built and tested, we then determined the effects of changing fluid conditions on the spectra of species dissolved in CO_2. The details of the apparatus and the measurements performed are presented in Chapter 8.

Chapter 3

Equipment, Procedures, and Analytical Methods

3.1 Description of Batch Reactor System

In our laboratory, hydrolysis experiments have historically been conducted in one of two ways. The most common method involves feeding compounds to a bench-scale, tubular, isothermal, isobaric, plug flow reactor (See DiNaro, 1999). Here, the organic solution is preheated from ambient temperatures to the final reactor temperature over a time of approximately 10 seconds. This time in the preheater accounts for about half of the total reaction time, making the prediction of accurate hydrolysis kinetics at a particular temperature very difficult or even impossible. This imprecision generally does not pose a serious problem, however, since these experiments are typically only conducted to verify that hydrolysis reactions contribute insignificantly to the conversion measured in oxidation experiments.

The other method of measuring hydrolysis kinetics occurs by immersing a small bomb reactor into a heated, fluidized sand bath for a prescribed length of time followed by quenching in an ice bath. Because heatup is slow due to the reactor's thermal mass, though, quantitative experiments are possible only for compounds with fairly slow hydrolysis rates, where the heatup time is small relative to the total reaction residence time. Additionally, subcritical hydrolysis experiments in such bomb batch reactors usually must be conducted with a small headspace (at the saturation vapor pressure) to prevent over-pressurization. Having a two-phase system further complicates kinetic measurements because different reactions and/or rates may occur in either phase.

To overcome the limitations of these previous systems, a small batch reactor was designed and built with the purpose of measuring well-defined, isothermal, isobaric hydrolysis kinetics. The primary objectives in the design of the system were as follows: 1) A batch reactor allows for measurement at short and very long residence times; 2) The heatup time of the reactant is minimal so that isothermal kinetics can be determined at short and long residence times; 3) Subcritical experiments can be conducted above the saturated vapor pressure where the solution exists in a single phase.

The reactor system is shown schematically in Figure 3.1 and its components are described in detail in the following sub-sections. The entire reactor system is contained in an aluminum box both to promote safety and to allow mounting of gauges and controls.

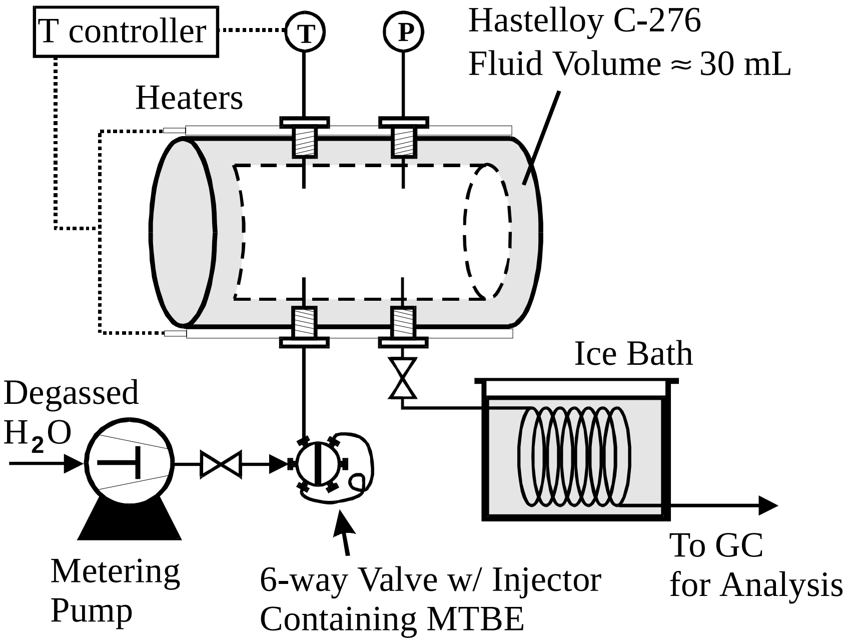

Figure 3.1: Schematic of the experimental batch reactor system

A photograph of the components and controls is shown in Figure 3.2 and will be referenced as each item is described. The procedure used for the operation of the reactor system is described in Section 3.2.

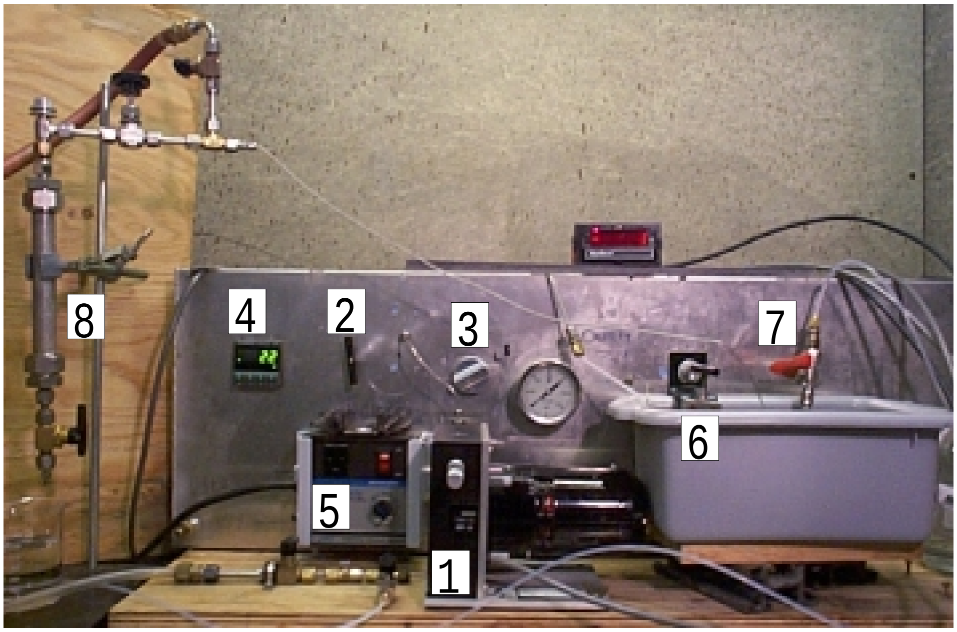

Figure 3.2: Control panel for experimental batch system with individual components labeled as follows: 1) Metering pump 2) Inlet valve 3) 6-way valve 4) Temperature controller 5) Potentiometer 6) Ice bath 7) Helium inlet valve 8) Collection vessel.

3.1.1 Feed Preparation and Injection

Because experiments at hydrothermal conditions may be very sensitive to dissolved gases and to impurities in water, proper feed preparation is essential in the design of our hydrolysis reactor system. Therefore, water from in-house distilled lines was further purified with a Barnstead Nanopure-A system. The Barnstead purification system consisted of four sequential cartridges (each of which removed certain contaminants) followed by a device that measures resistivity to ensure proper water purity. The first cartridge in the sequence was a MACROpure cartridge (p/n D0836), designed to remove most organics and colloids. The purification continued with an ULTRApure cartridge (p/n D0809) that removed any dissolved cations and anions. This cartridge was followed by an ORGANICfree cartridge (p/n D0820) that removed any remaining dissolved organics, and finally, a 0.2 micron filter cartridge (p/n D0749) removed any suspended particles. The resistivity of the water was continuously measured and was only used when the value exceeded 18.0 MΩ-cm.

The purified water was collected in a 1 L glass bottle (Wheaton Scientific) and placed on a hot plate stirrer (VWR p/n 58849-001). Prior to any experiments, the water was continuously stirred and boiled for a minimum of one hour to ensure that no oxygen or carbon dioxide dissolved from the air into the water. A 2 m length of 1/8 in. O.D. Teflon™ tubing was used to carry the boiling water through an ice bath into the inlet of an Eldex metering pump (Model #B-100-S), labeled '1' in Figure 3.2. The metering pump was set to 5.0 units (largest setting for piston stroke) and delivered approximately 7.5 mL/min against a system pressure of 3500 psi. Following the pump was a High Pressure Equipment (HIP) valve (p/n 15-11AF2), labeled '2', which served as a secondary precaution to prevent back-flow from the reactor to the pump.

A Valco 6-way valve (p/n C6UW), labeled '3' in Figure 3.2 and shown schematically in Figure 3.3, was connected immediately in front of the reactor. With the 6-way valve in the “load” position, the water line passed directly through to the reactor.

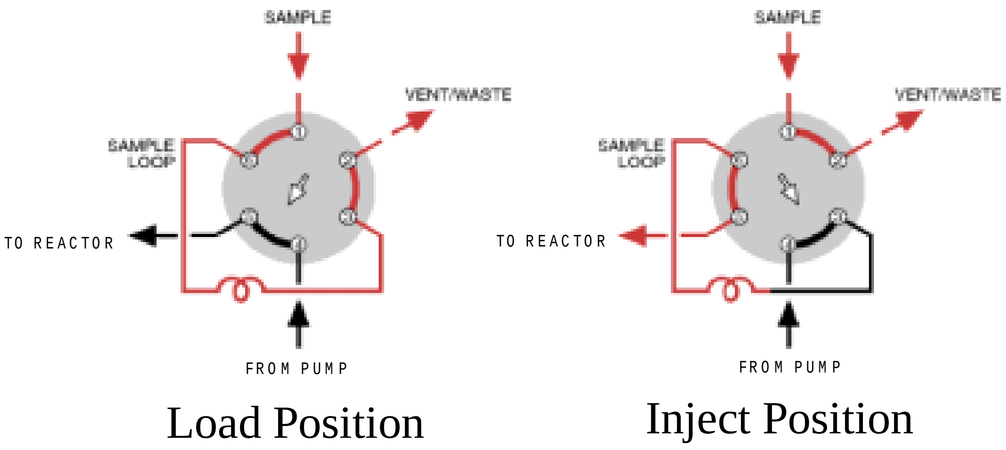

Figure 3.3: Schematic of Valco 6-way valve in both 'load' and 'inject' positions.

In the "load" position, organics or other liquids could be injected into the sample loop with a volumetric syringe via a zero volume syringe port (Valco p/n VISF-2), or they could be flushed through a sample loop using standard connections. When the 6-way valve was switched to the "inject" position, the water line was redirected through the sample loop to displace its contents into the main reactor vessel.

3.1.2 Batch Reactor, Measurements, and Controls

The main reactor vessel was constructed from a solid Hastelloy C-276 rod that was bored out and then TIG welded shut with a 1/2 in. thick piece of C-276. Four HIP female ports (to accept 1/8 in. taper seal fittings) were machined into the main reactor to allow for temperature and pressure measurements as well as inlet and outlet flows. A machinist's drawing of the reactor is shown in Figure 3.4 and the ports are numbered 1-4. C-276 HIP thermocouple adapters (p/n 15-21AF1AM2-T) were placed in each port to allow 1/16 in. O.D. tubing to be inserted through the ports and into the center of the reactor. A 1/16 in. inconel sheathed Type K thermocouple (Omega p/n GKQIN-116G-12) was inserted into Port 1 for temperature measurement (for the controller). Port 2 was connected to a

Dynisco Pressure Transducer (p/n G832-000-7.5M) and to a pressure relief valve (Nupro p/n SS-4R3A-F) that was set to open at 4000 psi (272 bar). The inlet stream was connected to Port 3 and the outlet was connected to Port 4. The tubing for the inlet and outlet streams was 1/16 in. (1.6 mm) C-276, inserted so that the tip reached approximately the middle of the reactor.

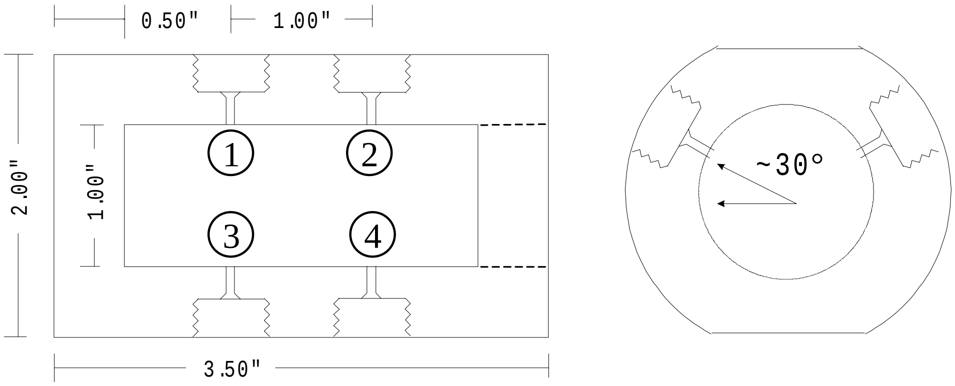

Figure 3.4: Machinist's drawing of the batch reactor. (Dimensions given in inches).

Six strip heaters (Omega p/n NSA-711) with a maximum power output of 125 W each (at 110 VAC) were placed around the reactor and held in place by two metal straps. The heaters were arranged so that two heaters were located on each of the flat faces (top and bottom) and one heater was on each side. A photograph of the reactor and adjacent heaters is shown in Figure 3.5. The reactor was then surrounded with two layers of Fiberfrax insulation (Durablanket-S 6#) to minimize heat loss. An Omega PID controller (p/n CN9000A), labeled '4' in Figure 3.2, was used to control the temperature based on the thermocouple measurement. The output from the controller was 4-20 mA, which was converted to on/off control of standard electricity (110 VAC, 60 Hz) by a solid state relay (Omega p/n SSR240DC45). The voltage was then reduced manually using a potentiometer (Cole-Parmer p/n P-02604-00), labeled '5' in Figure 3.2. The potentiometer was typically set to 20-30% of maximum power output for subcritical experiments, and 30-40% for supercritical experiments.

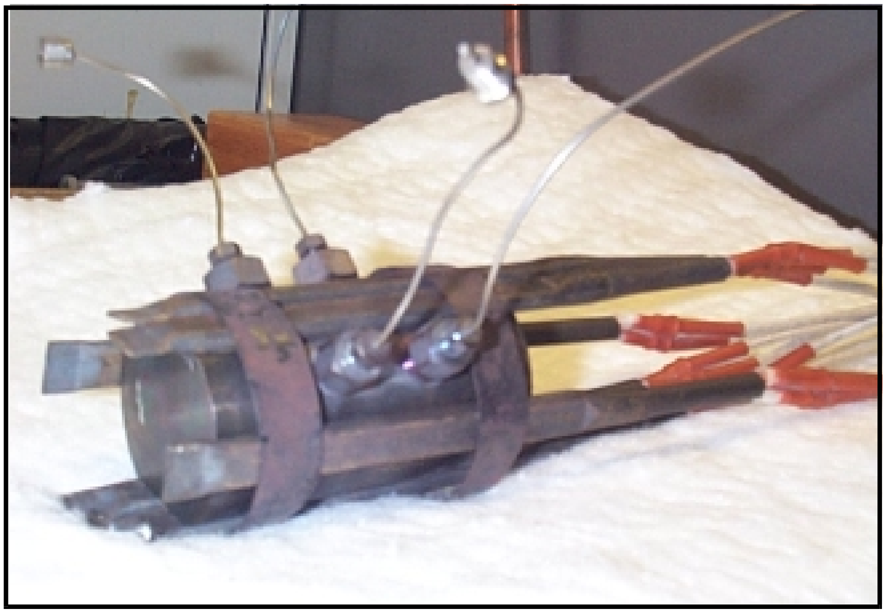

Figure 3.5: Photograph of batch reactor with heaters attached.

3.1.3 Post-Reactor Quench and Sample Collection

A second HIP valve immersed in an ice/water bath, labeled '6' in Figure 3.2, was placed immediately after the reactor. The HIP valve was immersed in an ice/water bath because it was rated to a maximum temperature of 400ºC due to its GRAFOIL seals. We found that the valve could adequately withstand short exposure to the contents of the reactor, even at temperatures as high as 600ºC. A coil made from 32 ft. (10 m) of 1/16 in. (1.6 mm) O.D. stainless steel tubing followed this valve. The coiled tubing served as a heat exchanger to quench the contents of the cell rapidly, terminating any hydrolysis reactions. Industrial grade helium was connected to the heat exchanger coil with a 1/4 turn valve (labeled '7') near the HIP valve in order to displace the effluent into the collection vessel. The collection vessel (labeled '8') was a vertically oriented, 6 in.

(15 cm) length of 1 in. (2.5 cm) O.D. tubing and could be evacuated prior to each run. At the top of the collection vessel was a septum that allowed for gas samples to be drawn and analyzed. A valve at the bottom of the collection vessel released the liquid contents for analysis.

3.2 Reactor Operation

The procedure for each measurement began by heating up the cell to the reaction temperature. Purified water was pumped into the cell until the desired pressure was reached. Two different methods for determining the desired pressure were used at different stages of experiments. For the experiments with methylene chloride, the initial pressure was set to 250 bar and the pressure relief valve was set to open at 250 bar. As the organic was injected (as will be discussed in the next paragraph), some of the hot water was displaced out of the cell through the relief valve. For the experiments with MTBE, the initial pressure was determined experimentally in preliminary runs, so that after injection of the organic, the final pressure would be 250 bar. It is not clear which method is superior, but the second method has the benefit of ensuring that none of the reactant is lost during injection.

Once the reactor stabilized at the desired temperature and pressure, the organic was prepared for injection. Using a zero volume syringe port on a Valco 6-way valve, the desired amount of pure organic (or solution) was injected into a 50 μL sampling loop in the "load" position. The 6-way valve was switched to the "inject" position, and 0.4 g (6 piston strokes at 100 Hz) of water was pumped to displace the organic feed into the cell where it mixed with the hot water. A stopwatch was used to measure the residence time and was started on the sixth “click” of the piston pump. Immediately after the injection, the 6-way valve was switched back to the “load” position and the HIP valve on the inlet line was closed. When the desired residence time was reached, the outlet valve was manually opened, and the entire contents of the cell were emptied through an ice bath via a coiled 1/16 in. (1.6 mm) 316 stainless steel tube. Helium was then used to displace the sample out of the 1/16 in. (1.6 mm) tube and into the collection vessel. The composition of each phase was analyzed, the cell was flushed completely with deionized, degassed water, and then the process was repeated for different residence times.

3.3 Analytical Methods

Gas samples were drawn with a 200 μL gas-tight syringe and injected directly into three gas chromatographs for analysis. Light hydrocarbons (*e.g.*, CH_4, C_2H_4, C_2H_6, C_3H_8, i-C_4H_8) were detected using an HP 5890 with an flame ionization detector. A separate HP 5890 with a thermal conductivity detector was used to determine concentrations of O_2, N_2, CO, and CO_2 using helium as carrier and reference streams. Hydrogen and helium were measured on the third HP5890, which used a thermal conductivity detector with N_2 as reference and carrier streams.

Liquid samples from the reactor system were collected in a small beaker and immediately transferred into GC vials using disposable pipets. The GC vials were 2 mL amber auto-sampler vials with PTFE/Silicone caps. Liquid composition was measured using an HP 6890 gas chromatograph equipped with an auto-injector and a flame ionization detector. Aqueous samples were injected directly into the gas chromatograph without any extraction. In the methylene chloride hydrolysis experiments, methylene chloride (CH_2Cl_2) and methanol (CH_3OH) were both quantified using GC. Two smaller peaks were detected, but their identification was not determined. In the MTBE hydrolysis experiments, methanol (CH_3OH), dissolved isobutene (*i*-C_4H_8), *tert*-butanol ($(CH_3)_3COH$), and MTBE ($CH_3OC(CH_3)_3$) were detected. These were the only peaks observed, and all concentrations were quantified.

Liquid samples were also analyzed using an HPLC equipped with a UV/Visible detector and a DC amperometry detector. HPLC measurements were primarily used for product identification.

A detailed description of all of the chromatography columns, detectors and method settings along with retention times for each type of analysis is included in the Appendix (11.2).

3.4 Data Analysis

3.4.1 Reactor Residence Time and Quench Time

Due to the injection method employed, there is a finite time for the injected organic to heatup and mix with the water in the reactor. To approximate the mixing time, a vessel similar to the batch reactor, except with sapphire windows on each end was used in the experimental system. An inorganic tracer (K_2MnO_4) simulated the injected organic and a video camera recorded the mixing. Visual results indicated that the mixing time at 250ºC was approximately 5 seconds and was 2-3 seconds at 550ºC. While pumping, the temperature deflections upon injection were large because the inlet directly contacted the thermocouple. Immediately after the pump was turned off, however, the temperature returned to within 1ºC of the setpoint.

To account for the effects of mixing and heatup transients, the concentration of organic (and products) at the shortest residence time (t_o) measured was used as the initial concentration (C_o) when determining the rate of destruction. In this manner, the effective residence time (τ_{res}) of a given run is given by subtracting the shortest time (t_o) from the final time (t_{final}).

$$\tau_{res} = t_{final} - t_o \tag{3.1}$$

This method determines the steady state decomposition rate rather than the initial reaction rate and the result should be valid so long as reverse reaction rate is not significant relative to the forward reaction rate. Admittedly, induction times and non-first-order order reaction processes that occur in the initial stages of the reaction will not be observed with this technique.

The reactor contents are quenched in a semi-batch mode, by opening the exit valve and allowing the contents to expand into the ice bath. The time needed to quench the reactor contents is difficult to characterize and varies with the temperature of the system. Above the critical temperature, quenching is very rapid (<1 s) since the fluid simply expands across the outlet valve. Below the critical temperature (when the water is liquid), the pressure immediately drops below the vapor pressure when the outlet valve is opened. The liquid contents then flash to produce a saturated vapor which is condensed rapidly in the quenching heat exchanger. The estimated quenching time for low temperatures is approximately 5 seconds and for high temperatures is approximately 1-2 seconds. To minimize error introduced, the procedure followed for each subsequent run was identical, so the relative residence times should be accurate.

3.4.2 Concentration Measurements

Liquid samples were analyzed with three injections per sample. Since each sample corresponded to a separate experiment, duplicate runs at the same residence times were conducted frequently to ensure reproducibility. Concentration data was plotted in an Excel spreadsheet as it was collected and experiments yielding measurements that appeared to be outliers were repeated.

While the liquid phase concentration measurements were easily determined quantitatively, the gas-phase measurements were difficult to reproduce. This problem was due primarily to the small amount of gas produced in the reaction (<0.5 mL). Furthermore, the control on the head pressure of helium used to push the sample into the collection chamber was not adequate to yield reproducible concentration measurements. Therefore, gas-phase measurements were used only to identify products and not to quantify results.

3.4.3 Assumed First-Order Rate Constants

The rate of reactant decomposition was determined by assuming that the rate of decomposition was first-order in the reactant and zero-order in all other species.

$$-\frac{d[\mathrm{A}]}{dt} = k^{*}\,[\mathrm{A}] \tag{3.2}$$

In Eqn 3.2, *k** is the apparent first-order rate constant and [A] is the molar concentration of the reactant, A. Eqn 3.2 is easily integrated over the appropriate limits.

$$\int_{[\mathrm{A}]_o}^{[\mathrm{A}]} \frac{d[\mathrm{A}]}{[\mathrm{A}]} = \int_{t_o}^{t_{final}} -k^{*}dt \tag{3.3}$$

Solving Eqn 3.3 and combining with Eqn 3.1 yields:

$$\ln\left(\frac{[\mathrm{A}]}{[\mathrm{A}]_o}\right) = -k^{*}\tau_{res} \tag{3.4}$$

Therefore, k^* can be determined from the negative slope of a plot of ln([A]/[A]$_o$) versus the residence time. This calculation was done for each set of data using the regression tool in Microsoft Excel and the uncertainty in the slope was calculated at 95% confidence. Although the value of the left-hand side of Equation (3.4) at $\tau_{res} = 0$ was necessarily zero based on the measured value of $[A]_o$, the intercept was not forced to zero in the regression. This is because the initial concentration was measured and had uncertainty associated with its value in the same way that all other concentration measurements did. In all cases, the regressed intercepts were always close to zero.

3.4.4 Activation Energy and Pre-Exponential Factors

The rate constant can be expressed as a function of temperature as:

$$k^* = A\exp\left(\frac{-E_a}{RT}\right) \tag{3.5}$$

Or equivalently:

$$\ln\left(k^*\right) = \ln(A) - \frac{E_a}{RT} \tag{3.6}$$

From this relationship, a plot of $\ln(k^*)$ vs. $1/T$ has a slope of $-E_a/R$ and an intercept of $\ln(A)$.

3.4.5 Uncertainty and Error Analysis

The uncertainty associated with each composition measurement was based on the scatter in the 3 subsequent injections. However, the scatter in subsequent measurements from a particular sample was always very small relative to scatter associated with concentrations measured from duplicate runs.

The uncertainty associated with values of the assumed first-order rate constant (k^*) were determined using the linear, least-squares regression tool in Excel with 95% confidence intervals. For this analysis, the intercept was not forced to zero because the initial concentration was a measured value.

To determine $\ln(A)$ and E_a, a linear, least-squares regression was performed on a plot of $\ln(k^*)$ versus $1/T$ with a 95% confidence interval. Uncertainties associated with these two parameter are highly correlated and therefore appear larger than the uncertainty associated with the calculated values of k^*.

3.5 References

DiNaro, J. L. (1999). "Oxidation of benzene in supercritical water: Experimental measurement and development of an elementary reaction mechanism." Ph.D. Thesis, Department of Chemical Engineering, MIT. Cambridge, MA.

Chapter 4

Hydrolysis of CH_2Cl_2 in Sub- and Supercritical Water

In this chapter, the results of experimental hydrolysis measurements and modeling of methylene chloride are presented. This work builds largely on previous measurements taken by Phil Marrone *et al.* (1998a; 1998b), which are discussed in the Introduction and Background Section of this chapter. The goal of this study was to experimentally measure and model the isothermal kinetics of methylene chloride hydrolysis from 100 to 500°C at 246 bar. The measurement and modeling effort was undertaken collaboratively with Dr. Dolors Salvatierra and is published in *I&EC Research* (Salvatierra *et al.*, 1999). A complete tabulation of the experimental data is included in Appendix 11.3.

4.1 Introduction and Background

Methylene chloride (CH_2Cl_2) has widely been used as a solvent in industry, and its presence in waste streams, contaminated soils, sediments and groundwaters (Page, 1981) makes it a good candidate for treatment by SCWO. Additionally, the carbon-chlorine bond of methylene chloride allows it to serve as a model compound for the broader class of chlorinated organics in SCWO, offering insight into the behavior of such bonds.

Several prior kinetic studies of chlorinated organics in supercritical water are available. While MODAR, Inc. (Thomason *et al.*, 1990) and Sandia National Laboratories (Rice *et al.*, 1993) have experimentally studied SCWO of CH_2Cl_2 (in addition to a number of other chemicals), their focus was obtaining high destruction and removal efficiencies rather than kinetic data. This research provides little insight into reaction kinetics, since incomplete conversion is required to determine reaction rates. In subcritical water and in the vapor phase, there have been several kinetic studies of CH_2Cl_2 hydrolysis and of the hydrolysis of a number of other chlorinated alkanes and alkenes. For example, Fells and Moelwyn-Hughes (1949) investigated the kinetics of CH_2Cl_2 hydrolysis in liquid water under acidic and alkaline conditions over a temperature range of 80 to 150°C. Moelwyn-Hughes *et al.* also conducted similar kinetic studies on the other members of the chlorinated methane series: chloromethane (Moelwyn-Hughes, 1949; Moelwyn-Hughes, 1953), chloroform and carbon tetrachloride (Fells and Moelwyn-Hughes, 1959). In related research, Chuang and Bozzelli (1986) investigated the vapor phase hydrolysis of chloroform from 611 to 1050°C at 1 atm, while Gaisinovich and Ketov (1969) studied the hydrolysis kinetics of carbon tetrachloride from 350 to 550°C. More recently, Jeffers and coworkers (1989; 1996a; 1996b) have examined and correlated the hydrolysis kinetics of a number of chlorinated methanes, ethanes, ethenes, and propanes from 0 to 180°C at pHs ranging from 3 to 14. In one study, Jeffers and coworkers (1996a) showed conclusively that the hydrolysis of carbon tetrachloride can be modeled with a first-order expression, correcting the rate expression developed by Fells and Moelwyn-Hughes (1959) which reported the hyrolysis as second-order in carbon tetrachloride.

4.1.1 Previous Experimental Studies of CH_2Cl_2 Hydrolysis

Fells and Moelwyn-Hughes (1949) studied the hydrolysis kinetics of CH_2Cl_2 in liquid water from 80 to 150°C. From a series of batch experiments conducted in Pyrex™

ampoules, they proposed the following empirical expression for the first-order rate constant for CH_2Cl_2 hydrolysis under neutral/acidic conditions:

$$\log_{10} k_{FMH} = 98.4408 - 29.66 \log_{10} T - 10597.3 / T \qquad (4.1)$$

where T is in Kelvin and k_{FMH} in s^{-1}. The use of the Fells and Moelwyn-Hughes correlation to predict CH_2Cl_2 hydrolysis conversion in supercritical water required extrapolating Eqn 4.1 more than 200°C beyond the temperature range for which this empirical correlation was developed. This may introduce significant errors and therefore a correlation based on high temperature data was necessary.

Fells and Moelwyn-Hughes also presented an expression for a competing reaction of CH_2Cl_2 with OH^- ions under basic conditions:

$$\log_{10} k_{basic} = 11.5669 - 5730.2 / T \qquad (4.2)$$

However, under neutral/acidic conditions, reaction with OH^- contributes less than 0.3% to the initial rate of CH_2Cl_2 destruction and much less as HCl is produced over the course of the reaction.

In a prior study done in our laboratory, conversion data on CH_2Cl_2 under SCWO conditions were obtained (Marrone *et al.*, 1998a). The results included the product spectrum and distribution along with a proposed reaction network. In that study, significant destruction of CH_2Cl_2 at subcritical temperatures was observed (in a section of the feed preheater with $100 < T < 374$°C), and little additional reaction occurred at supercritical conditions ($T > 400$°C). A temperature profile over the length of the preheater was estimated using a heat-transfer model. From this temperature profile, the rate of destruction at each temperature was determined based on conversion measurement at the end of the reactor. The rates determined with this method (below the critical temperature) were consistently higher than those predicted by the empirical correlation of Fells and Moelwyn-Hughes (Eqn 4.1).

In the prior study, Marrone *et al.* (1998b) used *ab initio* calculations to determine the transition state and a Kirkwood approximation to account for solvation effects. Even after accounting for solvent effects, discrepancies between conversion values measured at the end of the preheater and those calculated by Eqn 4.1 were larger than expected.

Furthermore, conversions obtained in the high-nickel alloy (Hastelloy C-276) tubing used for the reactor in Marrone's experiments were different than those measured in Pyrex™ ampoules by Fells and Moelwyn-Hughes. This difference suggests that the discrepancy in conversion values could be due to an additional metal-catalyzed surface reaction of CH_2Cl_2. Evidence in the literature supports this possibility of a surface reaction. It has been known for some time that chlorinated organic compounds in aqueous environments can undergo accelerated degradation in the presence of metals (Reynolds *et al.*, 1990; Wilson, 1995). Generally, the main pathway is believed to be a redox reaction where the chlorinated organic compound is reduced and the metal is oxidized. The literature on surface reactions of CH_2Cl_2 and other chlorinated compounds is intriguing in the present context. Earlier studies confirm the possibility that chlorinated methanes can undergo surface reactions (both reduction and oxidation). However, not all of the experimental conditions (temperatures, pressures/densities, and the metal/catalyst) used in these earlier studies overlap the conditions examined in our tubular flow reactor experiments. It is therefore not possible to unequivocally determine the importance of surface reactions in our system based on the literature alone. Since nickel is known to be a good catalyst for many oxidation and hydrolysis reactions of organic molecules, we set forth in this study to quantitatively evaluate its catalytic effectiveness.

These shortcomings motivated us to obtain isothermal kinetic data for hydrolysis under well-defined conditions. The objective of the work reported here was to quantitatively characterize CH_2Cl_2 hydrolysis kinetics at specific temperatures from 100 to 500°C. Isothermal batch experiments over this range of temperatures were employed to (1) develop a reliable global rate expression for the hydrolysis of CH_2Cl_2; (2) validate previous experimental results at low temperatures using improved analytical techniques; and (3) examine the possibility of catalytic effects induced by the metals comprising the walls of the reactor.

4.2 Experimental Techniques

4.2.1 Quartz Ampoule Experiments

A series of controlled batch experiments were conducted to determine if exposure to Hastelloy C-276 had any influence on the rate of CH_2Cl_2 hydrolysis. The composition of Hastelloy C-276 (by weight) is 55-64% Ni, 14.5-16.5% Cr, 4-7% Fe, 15-17% Mo, 3-4.5% W, 0.02% C, with traces of Nd, Ti, and Al. Quartz ampoules of approximately 6 mL in total volume were used as the reactor vessels. Each ampoule was filled with 5 mL of an aqueous CH_2Cl_2 solution. A fine powder of Hastelloy C-276 beads (–60 mesh size) was added to two of the four ampoules used for each residence time and temperature. The amount of Hastelloy C-276 used was based on achieving either a 1:1 or 10:1 molar ratio of Ni to CH_2Cl_2, assuming a 60 wt% nickel content of the alloy. The mass of Hastelloy C-276 used to obtain these ratios was 15 mg and 150 mg, respectively.

After loading the feed solution and metal (if used), the ampoule was immediately flame sealed and placed in a 1.9 cm (3/4 in.) O.D. and 12 cm (4.7 in.) long 316 stainless steel tube. The tube was used as a container to hold the ampoule during heating. In order to avoid breakage of the ampoule due to the pressure increase that occurs while heating, a calculated amount of water was added to the tube container to maintain balanced pressure between the interior of the ampoule and the external cylinder. This technique was developed by Houser and Liu (1996). Temperature was measured by a thermocouple inserted through the top end of the tube container. The total system — consisting of the metal pressure vessel and its ampoule — was heated either by insertion into a Techne SBL-2D fluidized sandbath (for short residence times) or a convection oven (for longer residence times). After the specified time in the sandbath or oven, the system was removed and cooled in an ice bath. The container was then opened, the ampoule was removed and cracked, and its contents analyzed for CH_2Cl_2.

Experiments in quartz were carried out at five different subcritical temperatures: 100, 130, 150, 200, and 250°C. For each temperature, seven different residence times ranging from 10 minutes to 14 days were explored. Each experiment at any given temperature and residence time consisted of a set of three ampoules — one containing only CH_2Cl_2 solution, one containing CH_2Cl_2 solution and 15 mg of Hastelloy C-276, and one containing CH_2Cl_2 solution and 150 mg of Hastelloy C-276.

4.2.2 High-Temperature, High-Pressure Reactor Experiments

The apparatus used for high-temperature experiments is described in detail in Chapter 3 and shown schematically in Figure 3.1. The temperatures studied were 300, 325, 340, 350, 360, 390, 450, and 500ºC and the pressure was set at 246 bar. Residence times ranged from 5 s to 10 min. Methylene chloride was injected from a filled sample loop (10 or 50 μL) via a 6-way valve and displaced with approximately 0.4 g of water. The initial methylene chloride concentration (C_o) was determined by the shortest residence time (t_o) experiment, and all other residence times were calculated relative to the shortest time.

4.3 Results

4.3.1 Quartz Ampoule Experiments

In order to have an accurate determination of the initial concentration of CH_2Cl_2, selected sealed ampoules were stored at 1°C (with and without metal in them) and opened at the same time as the ampoules used for the hydrolysis experiments. Measured CH_2Cl_2 concentrations from these selected ampoules were used as the initial concentration (C_0) for each run.

As an example of one of these batch experiments, results for 150°C are shown in Figure 4.1 as a plot of the fractional conversion, expressed as ln C/C_0, as a function of time. At each temperature, the data clearly show that Hastelloy C-276 had no significant effect on the rate of CH_2Cl_2 decomposition. In addition, data for all temperatures (100-250°C) and at each loading (*i.e.*, 0, 15, or 150 mg) of Hastelloy C-276 produced a straight-line fit (ln C/C_0 vs. t), indicating that the reaction exhibits first-order behavior. First-order rate constant values, calculated from the slopes of least-squares best-fit lines, are included in Table 4.1 along with the R-squared values and parameter uncertainties at the 95% confidence level. Note that the rate constant values for each data set at the same temperature are well within experimental uncertainty of each other, indicating that there is no statistically significant evidence of any catalytic effect. Thus, without sacrificing any accuracy, all three data sets at the same temperature were pooled to produce a single regressed line, which is displayed as the "*All Data*" result in Table 4.1.

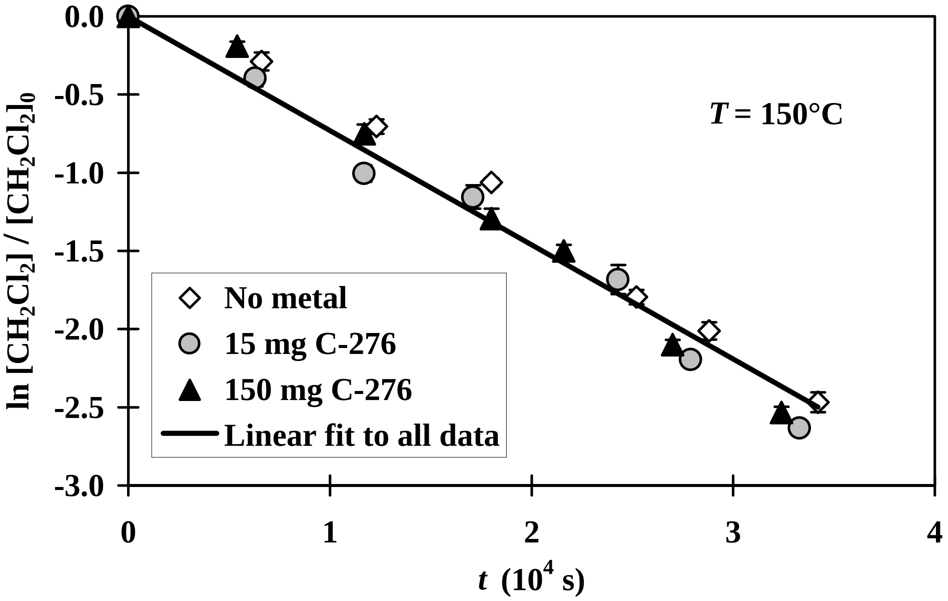

Figure 4.1: CH_2Cl_2 conversion results at T = 150°C from quartz ampoule experiments. The pressure for these experiments was the vapor pressure of pure water (4.8 bar).

Table 4.1: First-order rate constants from quartz ampoule experiments

Experimental Conditions		***k*** **(s^{-1})**	***R^2***	**# samples**
100°C	No metal	$8.76 \pm 0.75 \times 10^{-7}$	0.99	7
130°C	No metal	$1.06 \pm 0.12 \times 10^{-5}$	0.99	5
	15 mg of C-276	$9.58 \pm 1.60 \times 10^{-6}$	0.97	5
	150 mg of C-276	$9.13 \pm 0.86 \times 10^{-6}$	0.98	7
	All data	$9.84 \pm 0.67 \times 10^{-6}$	0.97	17
150°C	No metal	$6.89 \pm 0.58 \times 10^{-5}$	0.99	7
	15 mg of C-276	$7.60 \pm 0.56 \times 10^{-5}$	0.99	7
	150 mg of C-276	$7.47 \pm 0.62 \times 10^{-5}$	0.99	7
	All data	$7.30 \pm 0.32 \times 10^{-5}$	0.99	19
200°C	No metal	$1.02 \pm 0.17 \times 10^{-3}$	0.96	7
	15 mg of C-276	$8.21 \pm 1.10 \times 10^{-4}$	0.98	7
	150 mg of C-276	$8.94 \pm 3.06 \times 10^{-4}$	0.79	7
	All data	$9.12 \pm 1.10 \times 10^{-4}$	0.88	19
250°C	No metal	$6.51 \pm 1.47 \times 10^{-3}$	0.97	5
	15 mg of C-276	$6.55 \pm 1.87 \times 10^{-3}$	0.96	5
	150 mg of C-276	$9.47 \pm 4.49 \times 10^{-3}$	0.96	4
	All data	$6.98 \pm 0.97 \times 10^{-3}$	0.94	14

4.3.2 High-Temperature, High-Pressure (HT/HP) Reactor Experiments

For temperatures from 300 to 500°C, experiments were conducted in the high temperature, high-pressure reactor described in Chapter 3. The CH_2Cl_2 concentration of a sample taken at the shortest measured residence time (for each different temperature) was used as the initial concentration, and was repeated several times to ensure the reproducibility of the result.

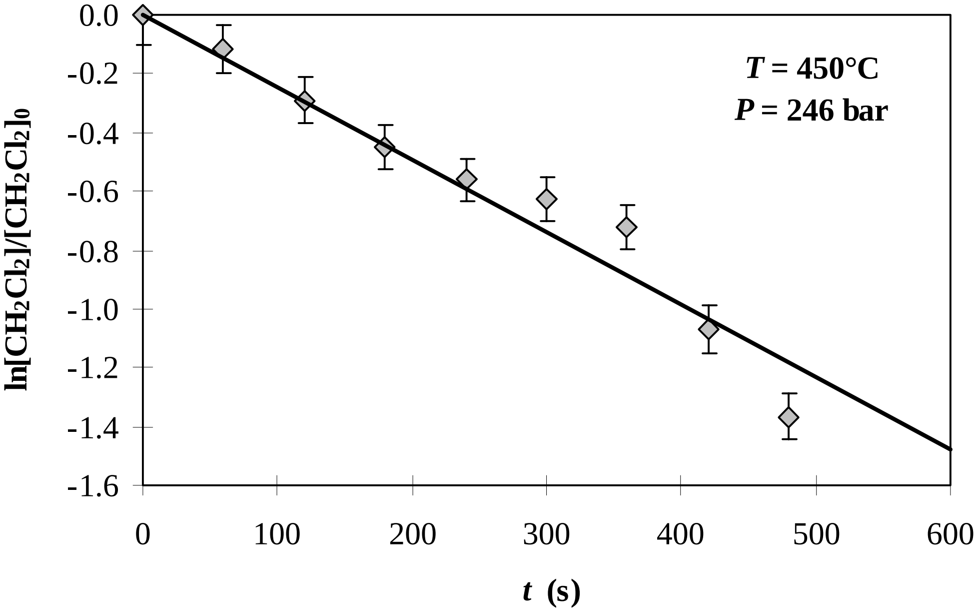

Figure 4.2: CH_2Cl_2 Conversion results at T = 450°C and P = 246 bar from the high temperature, high-pressure reactor experiments

As an example of these batch experiments, results at 450°C and 246 bar are shown in Figure 4.2 as ln C/C_0 versus time. First-order rate constant values obtained for each experiment are given in Table 4.2 along with the R-squared values and parameter uncertainties for the linear fit at a 95% confidence level.

Near the critical point, at 390°C, the physical properties of the solvent are very sensitive to the pressure/density and temperature changes, resulting in higher uncertainties. For example, it is difficult to duplicate the initial concentration (C_0) accurately between runs because a small change in the pressure from one run to another greatly affects the density and thus the measured CH_2Cl_2 concentration.

Table 4.2: Results of experimentally measured rate constants compared to those predicted by the Fells and Moelwyn-Hughes Correlation

T (°C)	k_{FMH} [a] (s^{-1})	k [b] (s^{-1})	C_o [c] (M)	Time [d]	# samples	reactor
100	5.66×10^{-7}	$8.76 \pm 0.72 \times 10^{-7}$	2.21×10^{-2}	0-14 d	7	Glass
130	7.44×10^{-6}	$9.84 \pm 0.67 \times 10^{-6}$	1.80×10^{-2}	0-72 hr	18	Glass
150	3.10×10^{-5}	$7.33 \pm 0.36 \times 10^{-5}$	1.60×10^{-2}	0-10 hr	25	Glass
200	5.01×10^{-4}	$9.12 \pm 1.10 \times 10^{-4}$	1.80×10^{-2}	0-1 hr	19	Glass
250	3.53×10^{-3}	$6.98 \pm 0.96 \times 10^{-3}$	2.21×10^{-2}	0-10 min	14	Glass
300	1.38×10^{-2}	$1.50 \pm 0.32 \times 10^{-1}$	2.40×10^{-2}	5-12 s	6	HT/HP
325	2.30×10^{-2}	$8.48 \pm 1.99 \times 10^{-2}$	5.84×10^{-2}	10-30 s	5	HT/HP
340	3.00×10^{-2}	$1.17 \pm 0.31 \times 10^{-1}$	8.20×10^{-2}	5-35 s	11	HT/HP
350	3.52×10^{-2}	$1.34 \pm 0.23 \times 10^{-1}$	8.20×10^{-2}	5-25 s	11	HT/HP
360	4.07×10^{-2}	$1.33 \pm 0.10 \times 10^{-1}$	8.51×10^{-2}	5-25 s	8	HT/HP
390	5.90×10^{-2}	$6.70 \pm 7.43 \times 10^{-2}$	7.93×10^{-2}	5-25 s	7	HT/HP
450	9.58×10^{-2}	$2.47 \pm 0.26 \times 10^{-3}$	3.73×10^{-4}	2-10 min	9	HT/HP
500	1.17×10^{-1}	$7.72 \pm 0.95 \times 10^{-3}$	3.27×10^{-4}	1-6 min	7	HT/HP

[a] Rate constant predicted by the Fells and Moelwyn-Hughes correlation (Eqn 4.1)
[b] Results from a linear ln (C/C_o) vs t plot of data from this study
[c] Initial concentration of CH_2Cl_2 for this set of data
[d] Range of residence times

4.4 Discussion

In order to check the reproducibility of their results, three of the temperatures selected for study were in the temperature range investigated by Fells and Moelwyn-Hughes (1949). Corresponding values of the first-order rate constant predicted by the Fells and Moelwyn-Hughes correlation (Eqn 4.1) at each operating temperature are also shown in Table 4.2. Note that for temperatures up to 250°C, the rate constant value from the batch experiments of this study using the complete set of pooled data is about twice that predicted by Eqn 4.1, and the discrepancy is even larger as the temperature approaches the critical point (374°C). This factor of two is consistent with the results from our earlier plug flow reactor experiments which used an estimated temperature profile to predict the CH_2Cl_2 concentration at the end of the preheater section and integrated Eqn 4.1 over the predicted temperature-time history.

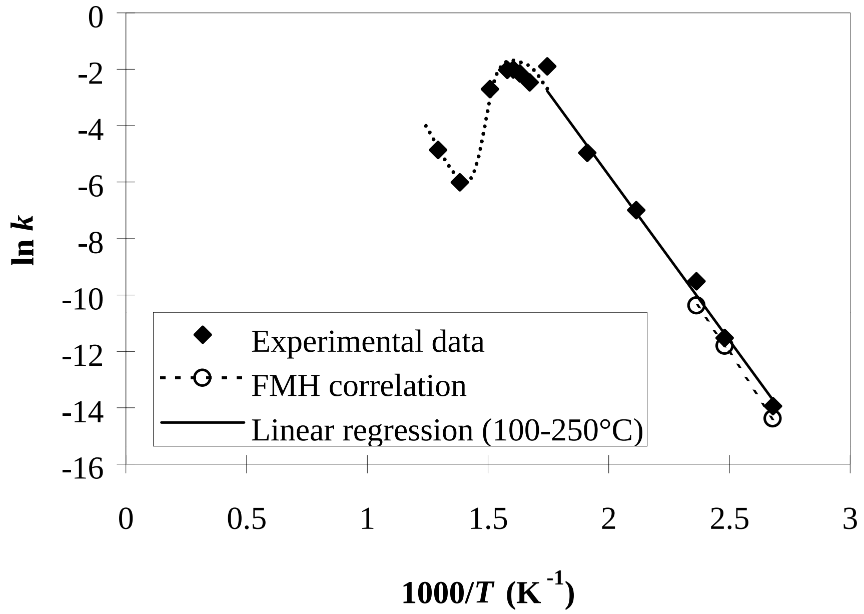

Figure 4.3: Arrhenius plot of experimental data and the correlated first-order rate expression from 100 to 250°C

The Arrhenius plot in Figure 4.3, representing ln *k* versus 1000/*T* (K^{-1}), shows a comparison between the values predicted by the Fells and Moelwyn-Hughes correlation (Eqn 4.1) and our results. Although the lower predictions of Eqn 4.1 are partially hidden by the scale selected, one can see that within experimental uncertainties, the slopes (or activation energies) determined from either data set are similar. The regressed rate expression based on our results in the linear, first-order region from 100 to 250°C is:

$$\ln k = 17.675 - \frac{11719}{T} \tag{4.3}$$

where T is the absolute temperature (K). Eqn 4.3 leads to a pre-exponential factor of 4.75×10^7 s^{-1} ($\ln A = 17.7 \pm 4.4$) and an activation energy (E_a) of 97.4 ± 15 kJ/mol for this linear region. As is commonly the case, A and E_a are highly correlated so errors in the predicted values of k using:

$$k = A \exp\left[\frac{-E_a}{RT}\right] \tag{4.4}$$

are lower at 95% confidence level than might be expected based on the individual errors reported for A and E_a.

From Figure 4.3, we also see very non-linear behavior above 300°C. A local maximum occurs in the rate constant around 350°C followed by a local minimum near 400°C. This behavior reflects the dramatic changes in the physical properties of water that occur in the critical region (374°C ± 30°C). These property changes can result in either a shift in the primary reaction mechanism or a destabilization of the transition state due to the decrease in the dielectric constant. This decrease in dielectric strength is particularly important when the transition state has a different dipole moment than the reactants. These experimentally observed local extrema are consistent with the observations of the previous study in our group (Marrone *et al.*, 1998b).

Using the experimentally-determined rate constant based on our data from 100 to 250°C, we applied the Kirkwood correction in order to account for solvent effects near and above the critical temperature of pure water.

$$\ln k = \ln A - \frac{E_a}{RT} + \Phi(T, \varepsilon, \rho, d_{m,i}) \tag{4.5}$$

In this modified rate equation, Φ is the Kirkwood correction factor to the rate constant and its values over the temperature range of interest are calculated from *ab initio* techniques (see (Marrone *et al.*, 1998b)). In general, Φ is a function of temperature, dielectric constant (ε), fluid density (ρ), and the dipole moment of the reactants and transition state ($d_{m,i}$). Although the values of Φ were calculated from first principles, it is computationally convenient to apply a polynomial fit in temperature:

$$\Phi(T,\varepsilon,\rho,d_{m,i}) = \Phi(T) = \sum_{k=0}^{9} \alpha_k T^k \tag{4.6}$$

where values of the coefficients (α_k) were regressed in prior work (Marrone *et al.*, 1998b). The values of these parameters are listed in Table 4.3.

Table 4.3: Parameters for calculating the Kirkwood correction factor in Eqn 4.6.

T range (°C)	**25 ≤ T ≤ 374**	**374 ≤ T ≤ 386**	**386 ≤ T ≤ 525**	**525 ≤ T ≤ 600**
α_0	1.3658×10^{-1}	7.2641851×10^{4}	1.2294119×10^{5}	-2.6826×10^{1}
α_1	-1.1319×10^{-2}	-5.8225257×10^{2}	-1.4212424×10^{3}	1.1691×10^{-1}
α_2	3.8850×10^{-4}	1.5556709×10^{0}	6.3373575×10^{0}	-2.3416×10^{-4}
α_3	-7.9558×10^{-6}	$-1.3855168 \times 10^{-3}$	$-1.2385424 \times 10^{-2}$	1.5557×10^{-7}
α_4	9.4188×10^{-8}		4.1293324×10^{-6}	
α_5	-6.7546×10^{-10}		2.3961584×10^{-8}	
α_6	2.9717×10^{-12}		$-3.8255570 \times 10^{-11}$	
α_7	-7.8277×10^{-15}		$1.8223581 \times 10^{-14}$	
α_8	1.1315×10^{-17}			
α_9	-6.8988×10^{-21}			

Applying the Kirkwood correction (Eqn 4.5) to our correlation (Eqn 4.3) reproduced the experimental data quantitatively over the entire temperature domain of this study remarkably well, as shown in Figure 4.4. In a previous study, the Kirkwood correction was applied to the Fells and Moelwyn-Hughes (FMH) expression (Marrone *et al.*, 1998b). The modified FMH correlation –also shown in Figure 4.4– only qualitatively captured the changes in *k* near the critical point, but significantly under-predicted *k* values above 200°C.

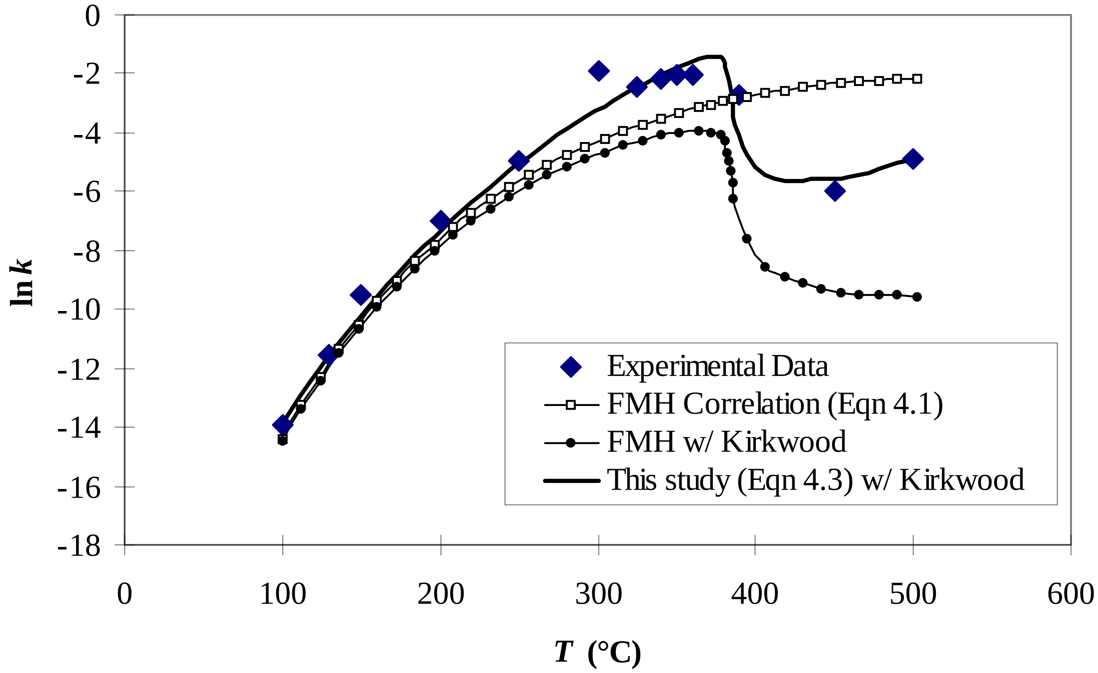

Figure 4.4: Comparison of experimental rate constant data with the extrapolation of the Fells and Moelwyn-Hughes correlation, the FMH correlation with the Kirkwood correction, and the correlation found in this study with the Kirkwood correction

Additionally, Marrone *et al* (1998a) regressed the following rate expression to conversion data at the end of the preheater using the calculated temperature profile:

$$\frac{-d[\mathrm{CH_2Cl_2}]}{dt} = 10^{12.9}\exp\left[\frac{-180000}{RT} + \Phi\right][\mathrm{H_2O}][\mathrm{CH_2Cl_2}] \qquad (4.7)$$

Combining the second order rate constant with the molar concentration of water (from the NIST Steam Tables (Harvey *et al.*, 1998)) yields a pseudo first-order rate constant:

$$k_{eff} = 10^{12.9} \exp\left[\frac{-180000}{RT} + \Phi\right][H_2O] \tag{4.8}$$

Figure 4.5 compares the empirical rate constant from Eqn 4.3 (w/ Kirkwood) and the effective rate constant from Eqn 4.8. The agreement of Eqn 4.8 is excellent near the critical temperature and higher, but at lower temperatures the correlation significantly underpredicts the rate. Because the rate expression was regressed to measured conversions at the end of the preheater, it is logical that the fit would be most accurate in the region where conversion rates were highest (300-350°C).

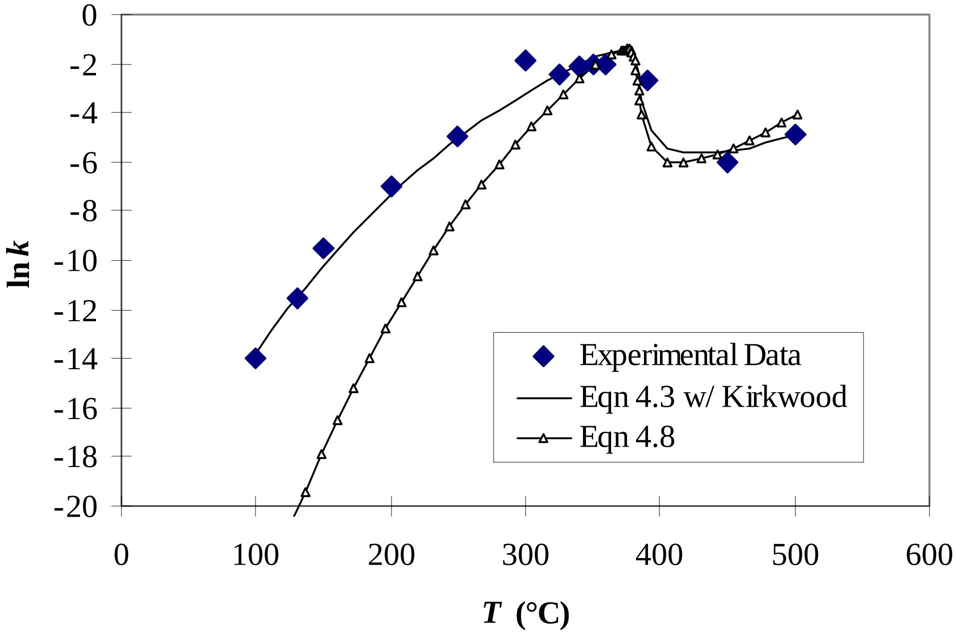

Figure 4.5: Comparison of ln *k* vs *T* from this study (Eqn 4.3 w/ Kirkwood correction) with values predicted by Eqn 4.8

4.5 Conclusions

Experiments at isothermal conditions within a range of temperatures from 100 to 500°C were completed using two different reactor systems. The results of the quartz ampoule batch experiments clearly show that (1) surface effects due to Hastelloy C-276 metal on CH_2Cl_2 hydrolysis are negligible, and (2) the Fells and Moelwyn-Hughes rate constant correlation (Eqn 4.1) predicts slower CH_2Cl_2 hydrolysis kinetics than our experimental results.

A new empirical first-order rate expression, obtained using data from 100 to 250°C, was determined and correlated using a standard Arrhenius expression for the rate constant (Eqn 4.3). Over the entire temperature range measured from 100 to 500°C, variations of the experimental rate constant are quantitatively consistent with Kirkwood corrections for changes in dielectric constant and density in the near critical and supercritical region.

4.6 References

Chuang, S. C. and J. W. Bozelli (1986). “Conversion of chloroform to HCl by reaction with hydrogen and water vapor.” *Environmental Science & Technology* **20**: 568.

Fells, I. and E. A. Moelwyn-Hughes (1949). “The kinetics of the hydrolysis of methylene dichloride.” *Journal of the Chemical Society*: 1326.

Fells, I. and E. A. Moelwyn-Hughes (1959). “The kinetics of the hydrolysis of chlorinated methanes.” *Journal of the Chemical Society*: 398.

Gaisinovich, M. S. and A. N. Ketov (1969). “High-temperature hydrolysis of carbon tetrachloride and phosgene in the gaseous phase.” *Russian Journal of Inorganic Chemistry* **14** (9): 1218.

Harvey, A. H., A. P. Peskin, and S. A. Klein (1998). *NIST/ASME STEAM Properties Database*, Release 2.11

Houser, T. J. and X. Liu (1996). “Reactions of 1-chloro-3-phenylpropane, 2-chlorotoluene, and 4-chlorophenol in supercritical water.” *Journal of Supercritical Fluids* **9**: 167.

Jeffers, P. M., C. Brenner and N. L. Wolfe (1996a). “Hydrolysis of carbon tetrachloride.” *Environ. Toxicol. Chem.* **15** (7): 1064.

Jeffers, P. M., L. M. Ward, L. M. Woytowitch and N. L. Wolfe (1989). “Homogeneous hydrolysis rate constants for selected chlorinated methanes, ethanes, ethenes, and propanes.” *Environmental Science & Technology* **23** (8): 965.

Jeffers, P. M. and N. L. Wolfe (1996b). “Homogeneous hydrolysis rate constants—Part II: Additions, corrections and halogen effects.” *Environ. Toxicol. Chem.* **15** (7): 1066.

Marrone, P. A., P. M. Gschwend, K. C. Swallow, W. A. Peters and J. W. Tester (1998a). “Product distribution and reaction pathways for methylene chloride hydrolysis and oxidation under hydrothermal conditions.” *Journal of Supercritical Fluids* **12** (3): 239.

Marrone, P. A., P. M. Gschwend, K. C. Swallow, W. A. Peters and J. W. Tester (1998b). “Solvation effects on kinetics of methylene chloride reactions in sub and supercritical water: Theory, experiment, and ab initio calculations.” *Journal of Physical Chemistry A* **102** (35): 7013-7028.

Moelwyn-Hughes, E. A. (1949). “The kinetics of certain reactions between methyl halides and anions in water.” *Proceedings of the Royal Society London A* **196**: 540.

Moelwyn-Hughes, E. A. (1953). "The kinetics of hydrolsys." *Proceedings of the Royal Society London A* **220**: 386.

Page, G. W. (1981). "Comparison of groundwater and surface water for patterns and levels of contamination by toxic substances." *Environmental Science & Technology* **15** (12): 1475.

Reynolds, G. W., J. T. Hoff and R. W. Gillham (1990). "Sampling bias caused by materials used to monitor halocarbons in groundwater." *Environmental Science & Technology* **24** (1): 135.

Rice, S. F., R. R. Steeper and C. A. LaJeunesse (1993) "Destruction of representative navy wastes using supercritical water oxidation." SAND94-8203:UC-402, Sandia National Laboratories: Livermore, CA

Salvatierra, D., J. D. Taylor, P. A. Marrone and J. W. Tester (1999). "Kinetic study of hydrolysis of methylene chloride from 100 to 500C." *Industrial & Engineering Chemistry Research* **38** (11): 4169.

Thomason, T. B., G. T. Hong, K. C. Swallow and W. R. Killilea (1990). "The MODAR supercritical water oxidation process." *Innovative Hazardous Waste Treatment Technology Series, Volume 1: Thermal Processes*. H. M. Freeman, Ed. Technomic Publishing**:** 31. Lancaster, PA.

Wilson, E. K. (1995). "Zero-valent metals provide possible solution to groundwater problems." *Chemical Engineering News* (July 3): 19.

Chapter 5

Hydrolysis of MTBE in Sub- and Supercritical Water

Like methylene chloride, methyl *tert*-butyl ether (MTBE) reacts in subcritical water in the absence of oxygen. This chapter presents the results of experimental hydrolysis measurements and modeling of MTBE. The goal of these measurements was to gain mechanistic insight into reactions of MTBE in hydrothermal water. A report of the experimental measurements and mechanistic modeling reported in this chapter has been accepted for publication in *Industrial & Engineering Chemistry Research* (Taylor *et al.*, in press, 2001). A complete tabulation of the data from the experiments described in this Chapter can be found in the Appendix (11.3).

5.1 Introduction and Background

5.1.1 Methyl *tert*-Butyl Ether (MTBE)

MTBE is a common gasoline additive that was initially used to enhance octane rating and to reduce engine knock, replacing organo-lead additives used previously. With the passage of The Clean Air Act of 1990, the Environmental Protection Agency mandated that polluted urban areas increase the amount of oxygenates in reformulated gasoline to levels as high as 2.7 wt% oxygen (which amounts to approximately 15% MTBE by volume). The concept was that oxygen contained in these new additives would result in more complete combustion of the fuel, resulting in lower emissions of hydrocarbons and carbon monoxide.

However in the early 1990's, after only a few years of deployed use in reformulated gasoline, reports of MTBE contamination in groundwater, attributed primarily due to leaking underground storage tanks, began to surface. By 1995, a study by the United States Geological Survey found that 27% of the shallow groundwater sources in the eight urban areas studied were contaminated with MTBE (Squillace *et al.*, 1996). Estimates now indicate that there exist over 10,000 contaminated sites in California alone (Happel *et al.*, 1998). Because of its high solubility and mobility in water, MTBE contamination continues to spread, rendering many drinking water supplies unpotable. The problem is further exacerbated by the fact that MTBE does not biodegrade under natural conditions and does not favorably adsorb onto carbon or soil particles. Therefore, it is important both to understand the reactivity of MTBE in water over a wide range of conditions and to investigate potential treatment and remediation options.

5.1.2 Objective

In a typical SCWO process, an organic-laden waste stream is preheated prior to the addition of oxygen. During this preheating stage over temperatures ranging from 25 to 650°C, thermal decomposition and hydrolysis reactions occur, significantly changing the composition of the feed entering the SCWO reactor. In this study, the reactions of MTBE in hydrothermal water under oxygen-free conditions were studied between 150 and 600°C at 250 bar in order to (1) understand the mechanism of ether decomposition in SCWO using MTBE as a model compound; (2) identify fundamental effects of changing solvent properties on the rate of reactions in hydrothermal environments; and (3) evaluate the effectiveness of SCWO for the treatment of MTBE contaminated water.

Because of their widespread use as solvents in industrial chemical processing and their relatively high solubility in water, ethers are common components of aqueous waste streams. Therefore, general knowledge of how this class of compounds react under hydrothermal conditions is valuable in assessing thermal treatment options. Although it is less commonly used in solvent applications than diethyl ether, MTBE is an ideal model compound for this study, as it has a low Henry's Law coefficient in water (0.59 bar·L/mol at 25°C) and therefore remains preferentially partitioned in the aqueous phase. MTBE is stable at ambient conditions, unlike diethyl ether, which readily forms peroxides that dramatically affect the kinetics and pose a potential safety hazard. As a result, MTBE was chosen as a model compound for our study.

The dramatic changes in the physical properties of water that occur in passing from subcritical to supercritical conditions can change both the energetics of reactions as well as the accessible pathways. For example, the measured activation energy of a specific chemical reaction includes both the intramolecular activation (i.e. bond breakage/formation or atomic rearrangement) as well as the solvation energy of the transition state and the reactant. In this study we attempt to link the experimentally measured reaction rate of MTBE to the changes in the solvent properties of water. Typically, ionic pathways tend to dominate below the critical point of water, whereas nonionic and free-radical pathways dominate above the critical point. This difference in pathways will be discussed as it relates to MTBE decomposition.

Finally, because of the widespread problem of MTBE contamination in groundwater, remediation technologies that are effective in achieving complete destruction are needed. Many articles in the news media and in scientific journals have focused on treatment options for MTBE contaminated water. Most of these options involve oxidation via ozone (Liang *et al.*, 1999) or OH radical production (Yeh and Novak, 1995), biodegradation (Hanson *et al.*, 1999), or sonolytic destruction (Kang *et al.*, 1999). While these options show promise for practical implementation after some of the impediments are overcome, a fundamental understanding of the chemistry is still lacking.

In this study, we characterize the preheating region as the first step of MTBE decomposition and will report on the subsequent oxidation of the hydrolysis products in supercritical water in a future article. Our intention with this study was to obtain a better fundamental understanding of the chemistry to support the practical implementation of SCWO as a viable treatment option. As such, the economic aspects of this technology are not considered in this paper.

5.1.3 Review of Prior Hydrolysis Studies

Earlier studies in our group have shown unusual effects on the rate of hydrolysis of CH_2Cl_2 over a range of conditions from 100 to 500°C at 250 bar (Marrone *et al.*, 1998b; Marrone *et al.*, 1998a). For example, a local maximum in the rate of methylene chloride hydrolysis at 350°C followed by a local minimum just above the critical temperature was identified (as discussed in Chapter 4)(Salvatierra *et al.*, 1999). This decrease in the hydrolysis rate near the critical point was attributed to changes in the energetics of the reaction which were due to changes in the polarity of the solvent according to Kirkwood theory. *Ab initio* quantum chemical calculations were performed to incorporate solvation effects of the reactant and the transition state into the experimentally determined activation energy. Krammer and Vogel (2000) also saw a local minimum followed by a local maximum in the hydrolysis rate of ethyl acetate over a temperature range of 250-450°C. They explained that a shift in mechanism — from an acid-catalyzed pathway at subcritical temperatures to a direct nucleophilic attack pathway at supercritical temperatures — resulted in two distinct kinetic regimes.

Several other investigators have studied hydrolysis of ethers in sub- and supercritical water. Katritzky and coworkers (1994) studied diphenyl ether, cyclohexyl phenyl ether, and 1-naphthyl phenyl ether in water at 460°C. Klein and coworkers studied the relative importance of pyrolysis and hydrolysis pathways of coal-derived ethers in supercritical water (Townsend *et al.*, 1988). From their data, a correlation with dielectric constant was made for the hydrolysis rate constant using a Kirkwood approach. Yamaura and coworkers studied the decomposition of dibenzyl ether in both subcritical (280-310°C) and supercritical (390-415°C) water (Funazukuri *et al.*, 1997). Typical Arrhenius behavior was observed and rate expressions were assigned to the hydrolysis and pyrolysis pathways. Importantly, their subcritical experiments were conducted with two phases present, which may affect the rates observed.

Penninger and coworkers studied the hydrolysis of diphenyl ether above the critical temperature (415-480°C) (Penninger *et al.*, 1999b). They determined that the hydrolysis of diphenyl ether proceeds by an acid-catalyzed ionic mechanism, even under supercritical conditions. Further investigation, involving the addition of NaCl to mixtures of diphenyl ether and supercritical water, supported their acid-catalyzed mechanism (Penninger *et al.*, 1999a). In those experiments, the reaction rate initially decreased at low concentrations of salt, but with addition of more salt, the reaction rate increased. This was explained by a mechanism where hydrated Na^+ clusters provided the catalytic proton to the reactant, leaving NaOH.

5.2 Experimental Techniques

Isothermal experiments were conducted in a batch reactor system described in Chapter 3 to measure the rate of destruction of MTBE in sub- and supercritical water. A total of 116 experiments were collected at 14 different temperatures ranging from 150 to 600ºC at pressures of 250 bar.

Three modifications to the experimental procedures were made after the experiments with methylene chloride. Firstly, in the early stages of these experiments, it became clear that improved degassing of the water was essential to obtaining reproducible results. Therefore, purified water with a resistivity of 18.0 MΩ-cm was continuously boiled on a hot plate to degas any dissolved oxygen or carbon dioxide. The boiled water was then passed through an ice bath immediately before entering the metering pump. Secondly, the initial pressure of the filled cell was not equal to the final pressure. In the methylene chloride experiments, the reactor was filled to 246 bar and then as more water was pumped in (with the organic), some fluid exited through a relief valve. In these experiments, the reactor was filled to an initial pressure that was determined experimentally (for each temperature) so that the final pressure after injection of the MTBE would be approximately 250 bar. In this manner, fluid did not have to be removed from the reactor during charging and pressurization/heating to reaction conditions. Finally, the method of filling the sample loop with the proper amount of organic was modified. Using a zero volume syringe port on a Valco 6-way valve, 10 μL of pure MTBE were injected into a 50 μL sampling loop in the "load" position. Aside from these minor modifications, the experimental apparatus and procedures were followed as described in Chapter 3.

5.3 Results and Discussion

5.3.1 Products and Reaction Pathways

The primary products measured in the isothermal hydrolysis experiments were methanol, *t*-butanol, and isobutene. Methanol and *t*-butanol were only detected in the liquid effluent, whereas isobutene was detected both dissolved in the aqueous phase and in the gas phase. Small amounts of CO were also detected in the gas phase. From these products, we can deduce several possible pathways for the decomposition of MTBE. One pathway involves the direct reaction of MTBE to form methanol and isobutene:

$$t\text{-}\mathrm{C_4H_9OCH_3} \rightarrow i\text{-}\mathrm{C_4H_8} + \mathrm{CH_3OH} \tag{5.1}$$

Another possible pathway is the reaction of MTBE with one water molecule to form *t*-butanol and methanol:

$$t\text{-}\mathrm{C_4H_9OCH_3} + \mathrm{H_2O} \rightarrow t\text{-}\mathrm{C_4H_9OH} + \mathrm{CH_3OH} \tag{5.2}$$

The direct reaction of MTBE to form methanol and isobutene will henceforth be referred to as the *unimolecular decomposition pathway* and the reaction of MTBE with water to form *t*-butanol and methanol will be called the *hydrolysis pathway*. However, the presence of both pathways cannot be confirmed simply by the presence of all three products because isobutene and *t*-butanol equilibrate in the presence of hot water (Xu *et al.*, 1997):

$$i\text{-}\mathrm{C_4H_8} + \mathrm{H_2O} \rightarrow t\text{-}\mathrm{C_4H_9OH} \tag{5.3}$$

This equilibration among the products made it difficult to determine the relative importance of the two reaction pathways. One goal of this study was to determine the relative importance of the two competing pathways described by Eqns 5.1 and 5.2.

5.3.2 Kinetics of MTBE Decomposition

The concentrations of MTBE and the reaction products in the liquid phase are plotted versus time for T = 250°C and 425°C in Figure 5.1. From these plots, one can see the exponential disappearance of MTBE and the formation of methanol, isobutene, and *t*-butanol at temperatures above and below the critical point.

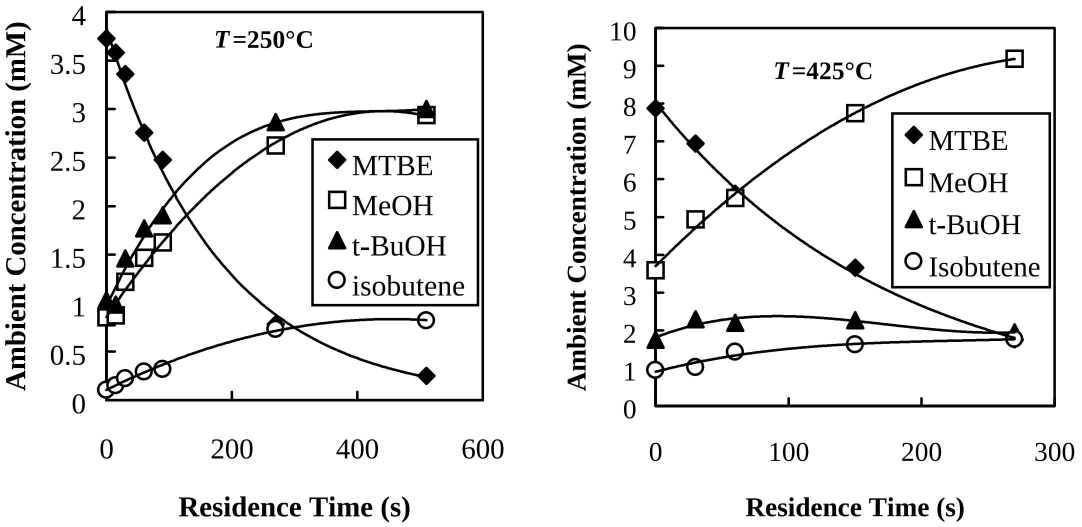

Figure 5.1: Composition of liquid effluent over the range of residence times measured at T = 250 and 425°C and P = 250 bar.

Below 374°C, *t*-butanol was produced in high concentrations at short residence times indicating that the direct pathway to produce *t*-butanol dominates (Eqn 5.2). However, the equilibration of isobutene and *t*-butanol (about 40% and 60% respectively at 250°C) occurs rapidly under these conditions, as noted by Antal and coworkers (Xu *et al.*, 1997). At 425°C, the concentration of *t*-butanol reached a maximum and then slowly began to decrease. This decline could indicate decomposition of either the *t*-butanol or the isobutene into gas phase products that were not detected. Another explanation could be that the dehydration reaction was taking place at a rate faster than *t*-butanol was being formed by the hydrolysis of MTBE. This behavior was not seen at temperatures below 400°C for the time scale of our measurements, but the decline became even more prominent as temperature was increased. At 550°C, the maximum concentration of *t*-butanol occurred in the first 5 seconds (before t_o) and decayed throughout the time investigated despite the fact that more *t*-butanol continued to be produced as the MTBE reacted.

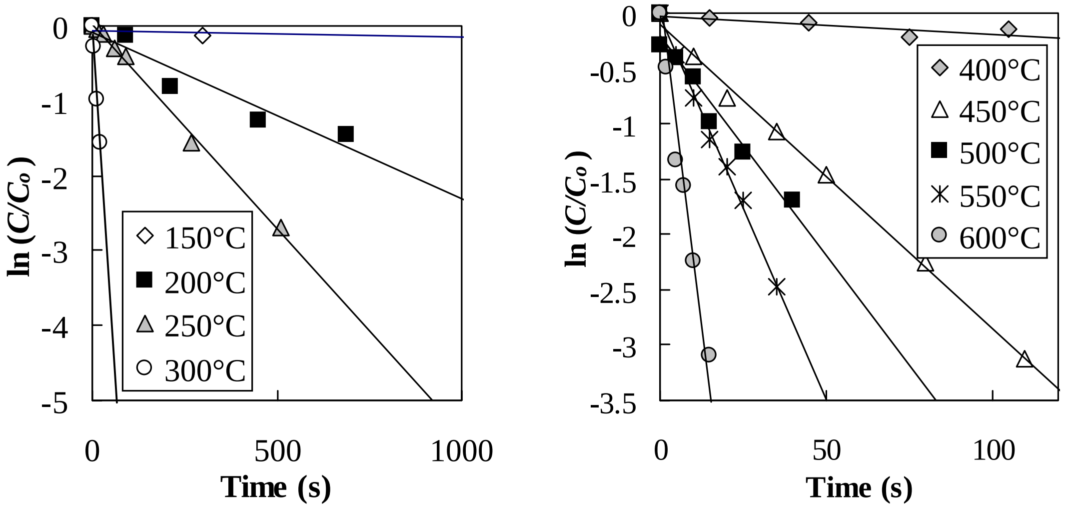

(a) (b)

Figure 5.2: Experimental data of the disappearance of MTBE plotted as ln (*C/Co*) versus time at 250 bar. Temperatures separated into subcritical (a) and supercritical (b) domains. Note: both time and concentration scales change between (a) and (b).

The rate of decomposition of MTBE is shown in Figure 5.2 as an assumed first-order plot of ln (C/C_o) versus time. Note that time = 0 refers to the shortest residence time measured (t_o) and C_o refers to the concentration measured at that time. The data are separated into subcritical (150-325°C) and supercritical (400-600°C) temperatures. The linearity of the data validates the first-order assumption for the present system. Therefore, the rate constant, k^*, can be estimated from the negative slope of the best-fit line. Table

5.1 lists the number of data points, the range of actual residence times, the conversion at the longest residence time, the best-fit value and the uncertainty (at 95% confidence) of k^* for each temperature.

Table 5.1: Summary of MTBE hydrolysis experiments performed at 250 bar

T (°C)	# of pts.	t_{actual} (s)	Conversion [a]	k^* (s^{-1}) [b]	Uncertainty [c]
150	5	300-7200	0.26	0.000028	±0.00002
200	6	30-720	0.77	0.0024	±0.001
250	7	30-540	0.93	0.0055	±0.0004
275	7	15-120	0.92	0.024	±0.007
300	6	5-25	0.79	0.077	±0.05
325	5	1-10	0.97	0.41	±0.06
400	15	15-540	0.74	0.0025	±0.0006
425	14	15-360	0.80	0.0046	±0.0006
450	18	5-60	0.77	0.025	±0.004
475	5	15-90	0.89	0.029	±0.002
500	8	5-45	0.82	0.041	±0.014
550	7	5-40	0.92	0.069	±0.005
575	7	5-30	0.91	0.095	±0.008
600	6	5-20	0.96	0.21	±0.03

[a] Conversion is defined as 1-C/C_o, from the shortest residence time to the longest
[b] Assumed first-order rate constant
[c] At 95% confidence

A plot of ln k^* versus 1000/T in Figure 5.3 shows that the rate constant increased as temperature increased from 150°C toward the critical point. At temperatures between 325 and 400°C, a local maximum in the rate constant was reached (around 350°C), followed by a sharp drop to a local minimum (around 400°C). The rate constant then proceeded to increase as temperature increased above the critical point. Clearly, the hydrolysis of MTBE does not follow a typical Arrhenius-type expression corresponding to a single reaction with a constant activation energy.

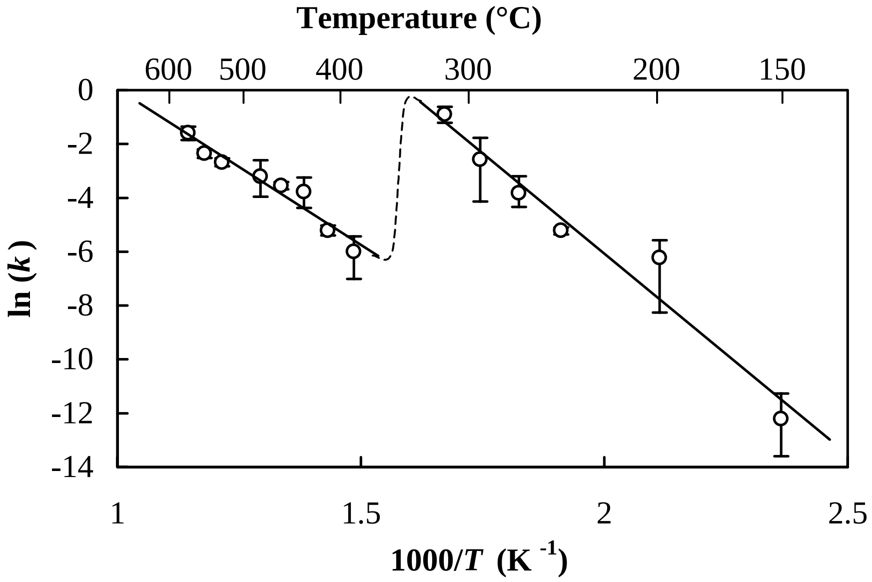

Figure 5.3: Arrhenius plot with an assumed first-order rate constant for the disappearance of MTBE at 250 bar. A linear, least-squares fit is shown for both sub-and supercritical regimes with a dashed curve drawn for the critical region.

5.3.3 Modeling MTBE Hydrolysis

One possible explanation for the non-linear behavior is that two or more different reaction pathways contribute to the overall rate of decomposition. This idea of multiple pathways finds corroboration in the study of Krammer and Vogel (2000), which modeled the decomposition of ethyl acetate by considering the reaction below the critical temperature as acid-catalyzed and above the critical temperature as a nucleophilic substitution. Because of the dramatic change in the polarity of water that occurs over this temperature range, reactions involving ionic pathways are expected to occur at much slower rates above the critical temperature of water. Given this behavior, the temperature domain can be conveniently divided into two specific regions; *e.g.* a subcritical region where an ionic mechanism dominates and a supercritical region where a nonionic mechanism dominates. Following this approach, a typical Arrhenius expression can be fit for each data region — the resulting best-fit lines are shown in Figure 5.3. The values obtained for the activation energy, E_a, and for log A of the reaction in the subcritical region are 105 ± 28 kJ/mol and 8.6 ± 2.9 s^{-1} respectively. Likewise, E_a and log A are 98 ± 27 kJ/mol and 5.1 ± 1.8 s^{-1} for the reaction occurring in the supercritical region. (Note: all uncertainties are at the 95% confidence level and the large error bands associated with E_a and A are reduced substantially when used to evaluate k^* due to the high correlation between the two parameters.)

If we assume that supercritical water behaves as a dense, nonpolar gas, then we can hypothesize that the nonionic decomposition pathway is similar to the gas-phase unimolecular decomposition. This pathway involves the intramolecular transfer of a hydrogen atom from a tertiary methyl group to the oxygen atom, resulting in a methanol leaving group. Another study, in which the unimolecular decomposition of MTBE was measured in the gas phase at low pressures (10^{-5} bar or less) for temperatures ranging from 615 to 885°C, yielded values of E_a and log A reported as 246.86 kJ/mol and 13.9 s^{-1} (Choo *et al.*, 1974). The identical values of E_a and log A were reported by Brocard and Baronnet (1987) at pressures of 0.1 to 0.3 bar and temperatures of 427 to 488°C. Comparison of the rate calculated from these parameters indicates that the gas-phase reaction pathway contributes significantly to our measured rate only at temperatures above 550°C. Although solvation may decrease the activation energy of the reaction, it is unlikely that the decrease will be large enough to make this pathway comparable to the observed reaction rates below 550°C. Therefore, there must be another mechanism occurring above the critical temperature that accounts for the experimentally observed decomposition rate of MTBE.

In the subcritical region, the hydrolysis most likely occurs by an acid-catalyzed pathway. But acid catalysis has been demonstrated in the supercritical region (Narayan and Antal Jr., 1990; Xu *et al.*, 1991) and might be relevant over the entire temperature range studied. In this manner, the local minimum in the experimentally observed rate constant may be due to the dramatic decrease in K_w (shown in Figure 1.3) and the consequent drop in the concentration of H^+ (catalyst) near the critical temperature. The most likely mechanism for the acid-catalyzed hydrolysis of MTBE is shown in Figure 5.4. In this mechanism, the first step involves the protonation of MTBE. Assuming that the first step is fast and quasi-equilibrated, we can express the concentration relationship of the species with the following equation:

$$K_1 = \frac{a_{t\text{-}C_4H_9OH^+CH_3}}{a_{t\text{-}C_4H_9OCH_3} a_{H^+}} = K_\gamma K_C = \frac{\gamma_{t\text{-}C_4H_9OH^+CH_3}}{\gamma_{H^+}\gamma_{t\text{-}C_4H_9OCH_3}} \frac{\left[t\text{-}C_4H_9OH^+CH_3\right]}{\left[H^+\right]\left[t\text{-}C_4H_9OCH_3\right]} \tag{5.4}$$

where [i] and γ_i are the molar concentration and the activity coefficient of species i respectively and reference states are assumed to be unit molarity with ideal solution behavior (i.e. $\gamma_i^o = 1.0$).

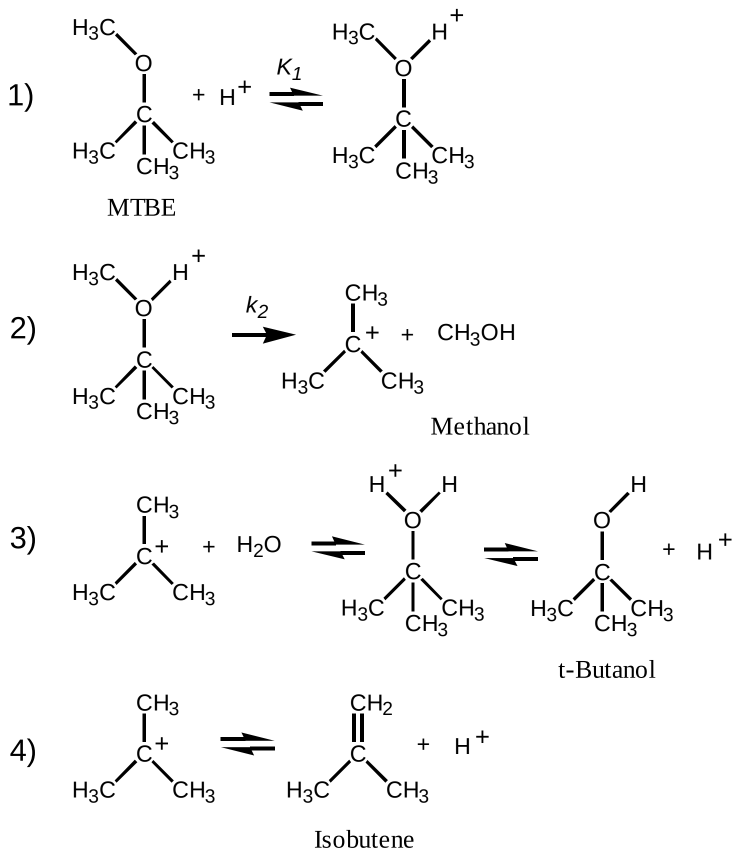

Figure 5.4: Acid-catalyzed mechanism for the decomposition of MTBE.

The second step of the reaction involves the S_N1 dissociation of the protonated MTBE to form methanol and a tertiary carbocation. If step 2 is the rate-determining step of the overall reaction, then we can express the rate of MTBE disappearance as:

$$-\frac{d\left[t\text{-C}_4\text{H}_9\text{OCH}_3\right]}{dt} = -\frac{d\left[t\text{-C}_4\text{H}_9\text{OH}^+\text{CH}_3\right]}{dt} = k_2\left[t\text{-C}_4\text{H}_9\text{OH}^+\text{CH}_3\right] \qquad (5.5)$$

Therefore, assuming $[H^+]$ is constant, rearrangement of Eqn 5.4 and substitution into Eqn 5.5 yields:

$$-\frac{d\left[t\text{-C}_4\text{H}_9\text{OCH}_3\right]}{dt} = k_2\frac{K_1}{K_\gamma}\left[\text{H}^+\right]\left[t\text{-C}_4\text{H}_9\text{OCH}_3\right] = k_{expt}\left[t\text{-C}_4\text{H}_9\text{OCH}_3\right] \qquad (5.6)$$

where K_γ = the ratio of activity coefficients given in Eqn 5.4 and k_{expt} = the assumed first-order rate constant measured in the isothermal experiments. The final two steps involve the competitive reactions that produce the observed final products. Step 3 shows the reaction of the carbocation with water to form *t*-butanol and regenerate the catalyst, H^+; while Step 4 shows the elimination reaction (E_1) of the carbocation to form isobutene and regenerate H^+. Note: the equilibrium reaction between the products is represented by the combination of Steps 3 and 4.

In this analysis, several assumptions were made that are important to discuss. Firstly, we assume that K_1 and k_2 are not functions of density. This assumption is supported by Johnston and coworkers (Ryan *et al.*, 1996; Xiang *et al.*, 1996), who found that reactions in which the number of charged species is conserved do not depend strongly on the density (and dielectric strength) of the solvent. Secondly, water dissociation is assumed to be the only source of H^+ (and OH^-) in the system. At ambient conditions, the K_a of methanol is approximately the same as that of water. If one assumes that the acidity of methanol and water remain approximately equal as the temperature and density are changed, then the contribution to $[H^+]$ due to methanol dissociation will be minimal since it is several orders of magnitude more dilute than water. The contributions due to *t*-butanol, isobutene, and MTBE should be much less since their K_a's and K_b's are orders of magnitude smaller than water at ambient conditions. However, if experiments were performed at higher concentrations of MTBE, producing higher concentrations of products, these effects on $[H^+]$ could not be ignored.

From this analysis, we can calculate k_2K_1/K_γ by dividing k_{expt} by $[H^+]$ at each temperature. A plot of ln (k_{expt} / $[H^+]$) versus 1000/T in Figure 5.5 shows the linearity over the entire temperature range, which is consistent with the acid-catalyzed mechanism proposed in Figure 5.4.

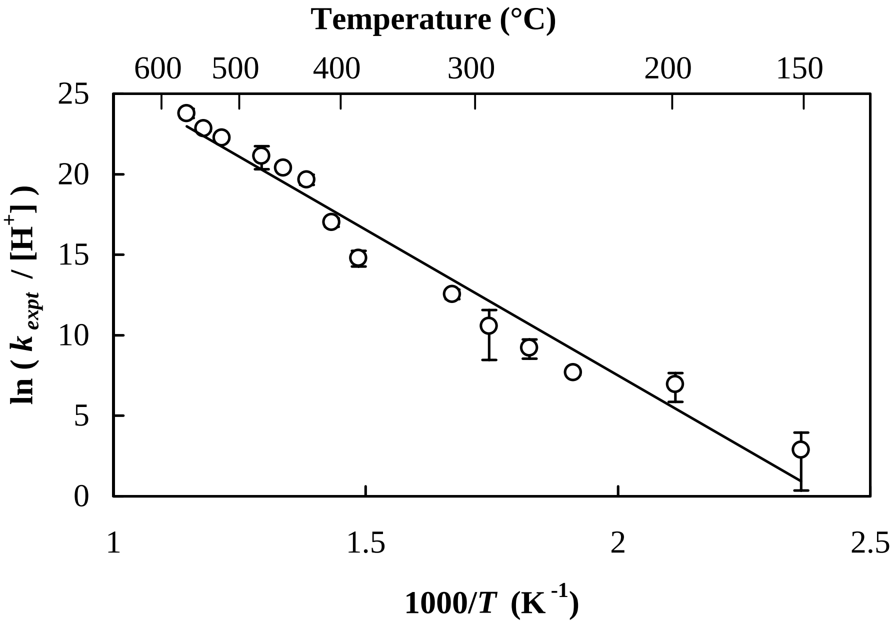

Figure 5.5: Experimentally measured rate constant, k_{expt}, divided by [H$^+$] versus 1000/T yields a linear fit over the entire temperature range measured at 250 bar.

From the best-fit line, the pre-exponential factor and the apparent activation energy can be determined. This is only an apparent activation energy because the experimentally observed rate constant is not that of a single elementary step.

$$k_2 \frac{K_1}{K_\gamma} = \left(A_2 \exp\left[\frac{-E_{a,2}}{RT} \right] \right) \left(\exp\left[\frac{\Delta S_1^{\text{o}}}{R} \right] \exp\left[\frac{-\Delta H_1^{\text{o}}}{RT} \right] \right) \tag{5.7}$$

A_2 and $E_{a,2}$ are the pre-exponential factor and the activation energy, respectively, for reaction Step 2, and ΔS_1^{o} and ΔH_1^{o} are the change in entropy and enthalpy for reaction Step 1 in its appropriate reference state. From this definition, the apparent activation energy and pre-exponential factors are:

$$E_{a,app} = E_{a,2} + \Delta H_1^{\circ} \tag{5.8}$$

$$A_{app} = A_2 \exp\left[\frac{\Delta S_1^{\circ}}{R}\right] \tag{5.9}$$

The best-fit value of A_{app} is $10^{19 \pm 1.5}$ L/mol s and $E_{a,app}$ is 150 ± 18 kJ/mol (uncertainties correspond to 95% confidence based on a linear fit). The resulting global rate expression for the decomposition of MTBE is:

$$-\frac{d[\mathrm{MTBE}]}{dt} = 10^{19\pm1.5} \exp\left[\frac{-150 \pm 18\,\mathrm{kJ/mol}}{RT}\right]\left[\mathrm{H}^{+}\right][\mathrm{MTBE}] \tag{5.10}$$

A comparison of predictions from Eqn 5.10 and experimentally measured rate constants are shown in Figure 5.6.

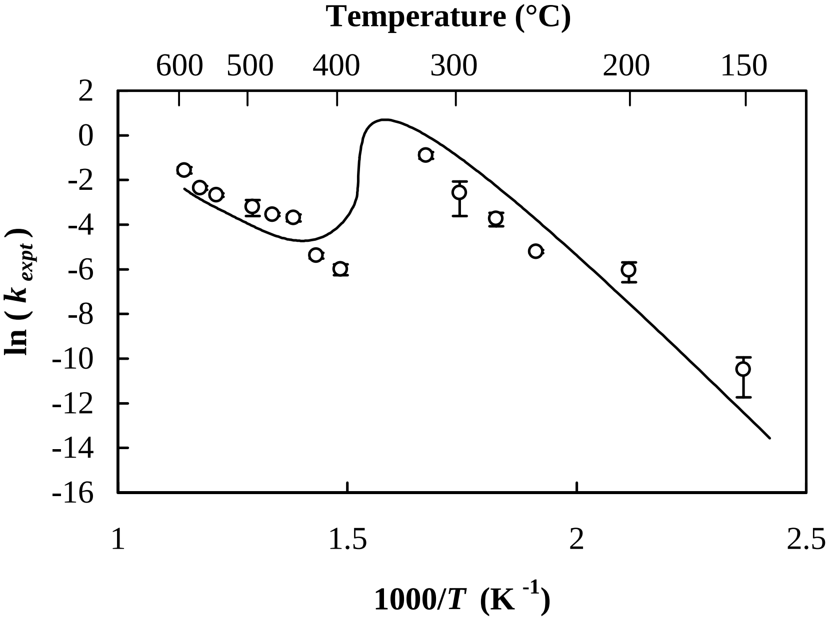

Figure 5.6: Experimental rate constant and the empirical rate expression from Eqn 5.10

In addition to the S_N1 mechanism, an S_N2 mechanism was considered. However, because of the steric hindrance of the *t*-butyl group, nucleophilic attack of a water molecule on the protonated MTBE is unlikely. Furthermore, an S_N2 mechanism would result in a kinetic fit involving the concentration of water to the first power, and this fit was considerably worse for the experimental data

Because the reaction was conducted at near neutral conditions ($[H^+] \approx [OH^-]$), a base-catalyzed mechanism would also fit the observed behavior of the rate constant. However, experiments with the addition of acid and base have confirmed that the acid-catalyzed pathway is dominant. These results will be presented in the following chapter of this thesis.

5.3.4 Comparison with Methylene Chloride Hydrolysis

The rates of methylene chloride hydrolysis and MTBE hydrolysis both show a local maximum below the critical temperature and a local minimum above T_c. At first glance, their behavior seems to be similar. However, the mechanistic reason for this rate behavior is in fact different. In the case of methylene chloride, the reaction proceeds by a nucleophilic substitution of a water molecule for a chloride group. The reaction rate decreases at the critical temperature because of changes in the solvation of the reactant and the transition state. Because the transition state has a stronger dipole moment, the transition state becomes less stable as the dielectric strength of water decreases dramatically in the critical region. This results in a larger activation energy for the nucleophilic substitution.

In the case of MTBE hydrolysis, the reaction proceeds by an acid-catalyzed mechanism. The rate of MTBE hydrolysis shows a decrease in the critical region due to the decrease in the concentration of H^+ as the ion dissociation constant of water is reduced by several orders of magnitude. This drop in K_w is also a result of the decrease in the dielectric strength of water, but the mechanism affecting the reaction rate is inherently different.

5.4 Conclusions

The rate of MTBE decomposition was experimentally measured in a batch reactor from 150 to 600°C and 250 bar. The decomposition rate shows a first-order dependence on the concentration of MTBE over the entire temperature range. The resulting first-order rate constant shows a local maximum below the critical temperature followed by a local minimum above the critical point. To explain the extrema in the rate constant, an acid-catalyzed mechanism was hypothesized and yielded predictions that were consistent with the experimental observations. A new empirical rate expression was determined with a first-order dependence on the concentrations of H^+ and MTBE (Eqn 5.10). For the entire temperature range studied from 150 to 600°C, the empirical rate expression quantitatively represents the experimentally measured decomposition rate within experimental uncertainties.

5.5 References

Brocard, J. C., and F. Baronnet (1987). "Effects de parois dans la pyrolyse du methyl *tert*-butyl ether (MTBE)," *J. Chim. Phys. Phys.-Chim. Biol.* **84**: 19.

Choo, K.-Y., D. M. Golden and S. W. Bensen (1974). “Very low-pressure pyrolysis (VLPP) of t-butylmethyl ether.” *International Journal of Chemical Kinetics* **6**: 631.

Funazukuri, T., R. M. Serikawa and K. Yamaura (1997). “Rate of dibenzyl ether decomposition in supercritical water.” *Fuel* **76**: 865.

Hanson, J. R., C. E. Ackerman and K. M. Scow (1999). “Biodegradation of methyl tert-butyl ether by a bacterial pure culture.” *Applied Environmental Microbiology* **65**: 4788.

Happel, A. M., E. H. Beckenbach and R. U. Halden (1998) "An evaluation of MTBE impacts to California groundwater resources." Report No. UCRL-AR-130897, Lawrence Livermore National Laboratory, Livermore, CA.

Kang, J. W., H. M. Huang, A. Lin and M. R. Hoffman (1999). “Sonolytic destruction of methyl tert-butyl ether by ultrasonic irradiation: the role of O_2, H_2O_2, frequency, and power.” *Environmental Science & Technology* **33**: 3199.

Katritzky, A. R., R. A. Barcock, M. Balasubramanian, J. V. Greenhill, M. Siskin and W. N. Olmstead (1994). “Aqueous high-temperature chemistry of carbocycles and heterocycles 20. Reactions of some benzenoid hydrocarbons and oxygen-containing derivatives in supercritical water at 460C.” *Energy & Fuels* **8**: 487-497.

Krammer, P. and H. Vogel (2000). “Hydrolysis of esters in subcritical and supercritical water.” *Journal of Supercritical Fluids* **16**: 189.

Liang, S., L. S. Palencia, R. S. Yates, M. K. Davis, J. M. Bruno and R. L. Wolfe (1999). “Oxidation of MTBE by ozone and peroxone processes.” *Journal of American Water Works Association* **91**: 104.

Marrone, P. A., P. M. Gschwend, K. C. Swallow, W. A. Peters and J. W. Tester (1998a). “Product distribution and reaction pathways for methylene chloride hydrolysis and oxidation under hydrothermal conditions.” *Journal of Supercritical Fluids* **12** (3): 239.

Marrone, P. A., P. M. Gschwend, K. C. Swallow, W. A. Peters and J. W. Tester (1998b). “Solvation effects on kinetics of methylene chloride reactions in sub and supercritical water: Theory, experiment, and ab initio calculations.” *Journal of Physical Chemistry A* **102** (35): 7013.

Narayan, R. and M. J. Antal Jr. (1990). "Influence of pressure on the acid-catalyzed rate constant for 1-propanol dehydration in supercritical water." *Journal of the American Chemical Society* **112**: 1927.

Penninger, J. M. L., R. J. A. Kersten and H. C. L. Baur (1999a). "Hydrolysis of diphenylether in supercritical water: Effects of dissolved NaCl." *Journal of Supercritical Fluids* **17**: 215.

Penninger, J. M. L., R. J. A. Kersten and H. C. L. Baur (1999b). "Reactions of diphenylether in supercritical water - mechanism and kinetics." *Journal of Supercritical Fluids* **16**: 119.

Ryan, E. T., T. Xiang and K. P. Johnston (1996). "Proton transfer reactions in subcritical and supercritical water." *Journal of Physical Chemistry* **100**: 9395.

Salvatierra, D., J. D. Taylor, P. A. Marrone and J. W. Tester (1999). "Kinetic study of hydrolysis of methylene chloride from 100 to 500C." *Industrial & Engineering Chemistry Research* **38** (11): 4169.

Squillace, P. J., J. S. Zogorski, W. G. Wilber and C. V. Price (1996). "Preliminary assessment of the occurrence and possible sources of MTBE in groundwater in the United States, 1993-1994." *Environmental Science & Technology* **30**: 1721.

Taylor, J. D., J. I. Steinfeld, and J. W. Tester (2001). "Experimental measurement of the rate of methyl *tert*-butyl ether hydrolysis in sub- and supercritical water." Accepted for publication in *Industrial & Engineering Chemistry Research*.

Townsend, S. H., M. A. Abraham, G. L. Huppert, M. T. Klein and S. C. Paspek (1988). "Solvent effects during reactions in supercritical water." *Industrial & Engineering Chemistry Research* **27**: 143.

Xiang, T., K. P. Johnston, W. T. Wofford and E. F. Gloyna (1996). "Spectroscopic measurement of pH in aqueous sulfuric acid and ammonia from sub- to supercritical conditions." *Industrial & Engineering Chemistry Research* **35**: 4788.

Xu, X., M. J. Antal Jr. and D. G. M. Anderson (1997). "Mechanism and temperature-dependent kinetics of the dehydration of tert-butyl alcohol in hot compressed liquid water." *Industrial & Engineering Chemistry Research* **36** (1): 23.

Xu, X., C. P. De Almeida and M. J. Antal Jr. (1991). "Mechanism and kinetics of the acid-catalyzed formation of ethene and diethyl ether from ethanol in supercritical water." *Industrial & Engineering Chemistry Research* **30**: 1478.

Yeh, C. K. and J. T. Novak (1995). "The effect of hydrogen peroxide on the degradation of methyl and ethyl tert-butyl ether in soils." *Water Environmental Research* **67**: 828.

Chapter 6

Reaction Pathway Analysis of MTBE Hydrolysis

This chapter analyzes the main reaction pathways responsible for the decomposition of MTBE under hydrothermal conditions. Specifically, the unimolecular decomposition and the acid-catalyzed hydrolysis pathways are considered. *Ab initio* computational calculation and new experiments are discussed as they relate to the reaction mechanism. These results will be submitted for publication in *Industrial & Engineering Chemistry Research*.

6.1 Background and Motivation

6.1.1 Background

In Chapter 5, the hydrolysis of methyl *tert*-butyl ether (MTBE) under hydrothermal conditions from 150-600°C at 250 bar was discussed. The experimentally measured reaction rate for the decomposition of MTBE reached a local maximum around 350°C followed by a local minimum near 400°C. An Arrhenius plot of the first-order rate constant versus 1000/T was shown in Figure 5.3, and two possible explanations for the decrease in reaction rate with increasing temperature near the critical point were discussed.

The first explanation assumed that two different reaction pathways occurred at isobaric conditions of 250 bar. With this assumption, an ionic hydrolysis mechanism dominates below the critical temperature where water is a polar solvent. Above the critical temperature, where water behaves as a nonpolar solvent, a nonionic pathway becomes the primary decomposition mechanism. Two separate rate expressions were fit to the data in the distinct regions, and comparable activation energies were determined for both temperature/density domains. However, the activation energy determined for the postulated nonionic pathway (at supercritical temperatures) was 98 kJ/mol whereas the gas-phase unimolecular decomposition value reported in the literature was 247 kJ/mol (Choo *et al.*, 1974). This large difference in the activation energies suggested that a different mechanism might be dominant in the supercritical region.

The second explanation for the unique behavior was that the reaction occurred by an acid-catalyzed mechanism (shown in Figure 5.4) over the entire temperature domain. According to this hypothesis, the decrease in reaction rate with increasing temperature near the critical point was attributed to the sharp drop in the concentration of H^+ as the ion dissociation product of water ($K_w = a_{H^+}a_{OH^-}$) was reduced from 10^{-11} to 10^{-18}. An empirical rate expression with explicit dependence on $[H^+]$ was fit to the data and was consistent with the measured rate constants within experimental uncertainty over the entire temperature range.

Although the acid-catalyzed mechanism was consistent with the experimentally measured rates, other mechanisms could also fit the experimental decomposition rate. For example, a base-catalyzed mechanism would show identical behavior as the acid-catalyzed mechanism, assuming that $[H^+] = [OH^-]$ (*i.e.* the acidity or basicity of the products and intermediates did not significantly alter the pH). Furthermore, ionic hydrolysis pathways in the supercritical region have not yet been experimentally validated. Therefore, further experiments and calculations were necessary to validate the hypothesized mechanism.

6.1.2 Objective

The ultimate objective of this study was to characterize the reaction mechanism(s) contributing to MTBE decomposition in both the sub- and supercritical water. Both *ab initio* computational chemistry tools and experimental measurements were employed to achieve this goal. Two different reaction mechanisms — the unimolecular decomposition and the acid-catalyzed hydrolysis — were considered, to determine the relative importance of each pathway.

The approach of the first part of this study was to calculate the effect of the solvent on the gas-phase decomposition rate of MTBE. In the previous chapter, this pathway was considered minor except at temperatures greater than 550ºC due to its large activation energy (247 kJ/mol) in the gas-phase (Choo *et al*., 1974). Because the transition state of this pathway has a significantly larger dipole moment than MTBE, however, the effective activation energy is reduced as the solvent becomes more polar (at lower temperatures), causing the rate to increase. Computational quantum chemistry tools were employed to determine the effects of the solvent on the activation energy. By doing so, the contribution of the unimolecular decomposition over the entire temperature range could be determined.

The aim of the second part of this study was to validate the acid-catalyzed hydrolysis pathway. According to the proposed reaction mechanism, the rate of MTBE decomposition is directly proportional to the concentration of H^+ in solution. Experimental measurements of the hydrolysis rate in the presence of strong acid or base were conducted to identify the effect of pH on the decomposition kinetics. By comparing the reaction rate at several different pH values, the dependence on the concentration of H^+ was determined and compared to that predicted by the mechanism.

6.2 Review of Prior Studies

6.2.1 *Ab Initio* Calculations of Solvent Effects on Reactions in SCW

Several authors have used *ab initio* computational tools to model solvent effects on reactions in SCW. Johnston and coworkers have looked extensively at the effects of solvation on the reaction of a chloride ion with methyl chloride using molecular dynamics (MD) tools as well as continuum models (see Bennett *et al*., 1995; Balbuena *et al*., 1995). The authors found that the change in solvation of ions in supercritical water, relative to ambient water, resulted in reaction rates that were 9-12 orders of magnitude greater than those in liquid water (ambient). Furthermore, the continuum model worked well at high and low densities but under-predicted the change in Helmholtz free energy for the reaction significantly at densities near the critical value (0.3 g/cc).

Pomelli and Tomasi (1997) later showed that they could reproduce the results by Johnston and coworkers using the polarized continuum model. This indicated that computations could be calculated much more efficiently than using MD to model individual water molecules. However, the continuum models also worked best in the region where the isothermal compressibility was not very large (high and low density).

Akiya and Savage (2000) used a combination of density functional theory and molecular dynamics for calculations on the dissociation of hydrogen peroxide in supercritical water. In their study, *ab initio* calculations were performed at vacuum conditions, and the resulting species (reactant and transition state) were then placed into the MD simulation. The authors found that solvation effects in supercritical water reduced the activation barrier for the dissociation of H_2O_2 by 2.1 kJ/mol relative to the gas-phase reaction.

In the hydrolysis of methylene chloride in sub- and supercritical water, Marrone *et al*. (1998) used *ab initio* computational tools to model solvent effects. The authors found the rate determining step to be the nucleophilic attack of H_2O on CH_2Cl_2 and calculated the transition state. Because the transition state was very polar, the activation barrier increased as the solvent became more polar. The authors developed a correction to the activation energy, relative to ambient water, using *ab initio* tools. The results were in good agreement with experimental measurements performed later in our laboratory (Salvatierra *et al*., 1999) and discussed in Chapter 4 of this thesis.

6.2.2 Effects of pH on Hydrothermal Reactions

Many authors have discussed acid-catalyzed reaction mechanisms for chemical transformations in sub-critical water. Siskin and Katritzky (2000) have written a review article that lists many of the reactions studied in hydrothermal water and that specifies which reactions are reported as being acid-catalyzed. The goal of these studies was to show the range of possible chemical reactions and qualitatively discuss mechanisms but not to investigate effects of acid on reaction kinetics quantitatively.

Eckert and coworkers have suggested the use of near-critical water for synthetic reactions to replace the need for added acid catalyst. In this manner, the enhanced value of K_w makes water a better medium for both acid- and base-catalyzed reactions. One such study involves Freidel-Craft alkylation reactions (T = 250-350°C), where the authors successfully synthesized substituted phenols by reacting phenol with secondary, tertiary, and to a lesser extent, primary alcohols (Chandler *et al*., 1997). In another study, Eckert and coworkers studied the rate of hydrolysis of various substituted benzoic acid esters from 250-300°C (Lesutis *et al*., 1999). As a result of the measured auto-acceleration in the rate of conversion and of the effect of changing substituents, the authors concluded that the hydrolysis occurred by an acid-catalyzed mechanism.

Krammer and Vogel (2000) have studied the rate of ethyl acetate hydrolysis in sub- and supercritical water (T = 250-400°C, P = 230-300 bar). In their analysis, they assumed that hydrolysis occurred via acid-catalysis and that the concentration of H^+ was due to the dissociation of the acetic acid produced in the reaction. Therefore, since an expression for K_A of acetic acid was not tabulated for their temperature/pressure domain, the authors fit an 8-parameter expression to K_A based on their hydrolysis data. According to their fit, K_A decreased by 8.5 orders of magnitude at 250 bar as the temperature was increased from 250°C (pK_A = 5.95) to 450°C (pK_A = 15.48). However, they concluded that near the critical temperature, the reaction mechanism changed from acid-catalysis (below T_c) to direct nucleophilic attack (above T_c).

Penninger *et al*. (1999b) have studied the hydrolysis of diphenylether in supercritical water from 415 to 480°C. In their analysis, they used an acid-catalyzed mechanism to describe the kinetics, where protons were provided by both the dissociation of water as well as the reaction product, phenol. In a subsequent study, the same authors studied the effects of added NaCl on the hydrolysis rate of diphenylether (Penninger *et al*., 1999a). Upon addition of small amounts of NaCl, the hydrolysis rate decreased. The decrease was attributed to the basicity of Cl^- under supercritical water conditions, which combined with H^+ to form molecular HCl. At higher salt concentrations, the hydrolysis rate increased proportional to the square root of the NaCl concentration. This was explained by a mechanism where hydrated Na^+ clusters provided the catalytic proton for the reactant, leaving NaOH.

Antal and coworkers have studied the acid-catalyzed dehydration of several alcohols in subcritical water (T = 225-320°C) with and without the addition of strong acid or base (Narayan and Antal, 1990; Xu and Antal, 1994; Xu *et al*., 1997;). In their initial study of the dehydration of *tert*-butanol to form isobutene, the authors described the kinetics of hydrolysis by an acid-catalzyed mechanism with two accessible reaction pathways (Xu and Antal, 1994). In one pathway, the protonated alcohol was dehydrated leaving a tertiary carbocation which then underwent elimination to form isobutene. In the second pathway, the carbocation reacted with another alcohol to form a protonated ether, which deprotonated and then underwent a unimolecular decomposition to form one isobutene molecule and one *tert*-butanol molecule. In their initial paper on *tert*-butanol, the authors fit empirical values for K_A of *tert*-butanol and determined that it decreased 9 orders of magnitude from ambient conditions to sub-critical conditions. However, in their later paper, the authors performed more experiments and concluded that the protons were primarily contributed from the H_2O, and that their fit values of K_A were probably not valid (Xu *et al*., 1997). In a study of the hydrolysis of 1- and 2-propanol, the primary alcohol was reported to react via direct acid-catalyzed dehydration, whereas isopropanol reacted by an acid-catalyzed ether formation followed by an uncatalyzed, unimolecular decomposition reaction (Antal *et al*., 1998). Note that this unimolecular decomposition of di-isopropyl ether is contrary to the mechanism we have proposed for the decomposition of MTBE and further motivates our study.

6.3 Computational and Experimental Methods

6.3.1 *Ab Initio* Calculations

Gaussian 98 was employed for quantum chemical calculations on the unimolecular decomposition of MTBE (Frisch *et al*., 1995). To model the solvent effects, the Self-Consistent Isodensity Polarized Continuum Model (SCI-PCM) was used. In this model, the shape of the molecule is approximated by a 3-dimensional surface mapped where the electron cloud density is 0.0004 (default value in *G98*). Then, the charge density is determined over this surface, and the solvent is modeled as a polarized continuum with a dielectric strength specified by the user.

The calculations were performed by first estimating the geometry of MTBE with empirical methods. The geometry of MTBE was then optimized using density functional theory (B3LYP) with the 6-31g(d) basis set in a vacuum. The SCI-PCM solvent model was then added and the geometry optimized for each value of dielectric strength (ε), beginning with the smallest values of ε (highest temperature) and using the resulting geometry as the initial guess for the subsequent value of ε. Once the geometry was determined for each value of ε, the vibrational frequencies and thermochemistry were calculated with B3LYP/6-31g(d). Finally, a larger basis set (6-311+g(3df,2p)) was used for single point calculations at each value of ε to get more accurate estimates of the energies.

Once the calculations of MTBE were completed, the geometry of the transition-state for the unimolcelular decomposition was investigated. The reaction coordinate of the unimolecular decomposition was assumed to be the hydrogen transfer from a methyl group to the oxygen atom. After guessing the initial geometry of the transition-state, the same procedure was followed for calculating the geometry, energy, and thermochemistry at each value of ε.

6.3.2 Effects of pH on MTBE Hydrolysis Rate

The objective of these experiments was to determine the effects of pH on the hydrolysis rate of MTBE. The experimental apparatus (shown in Figure 3.1) was described previously, and was used with the same operating procedure. However, in place of deionized water, solutions of HCl were used for acidic conditions, and solutions of NaOH were used for basic conditions. Solutions were prepared by first placing a measured quantity of deionized water into the feed bottle. Helium was then bubbled through the water for 5 minutes to remove any dissolved oxygen or carbon dioxide. After the water was properly degassed, a measured quantity of 1.0 M HCl (or 0.1033 N NaOH) was injected with a syringe through a septum and continually mixed with a stir bar on a magnetic plate. A head pressure of 10 psig (1.7 bar) helium was maintained over the solutions to exclude O_2 and CO_2 from the feed.

In the subcritical temperature region (at 250 bar), the hydrolysis rate of MTBE was measured at 200 and 250ºC at 5 different pH values. Two acidic solutions, two basic solutions, and one neutral solution (pure deionized water) were used to determine the dependence of the reaction rate on the concentration of H^+ (catalyst). The acidic solutions had ambient pH values of 3.0 and 3.7, and the basic solutions had pH values of

10.0 and 11.0. The pH of each solution was verified with titration prior to the experiments. The pH of the effluent from each experiment was measured with pH paper (± 0.2 pH units) to ensure that the products did not change the pH significantly.

For subcritical temperatures, these prepared solutions were sufficiently dilute to ensure complete dissociation of HCl and NaOH. The concentration of H^+ at the reaction conditions (subcritical temperature and high-pressure) was calculated as follows. For acidic conditions, the concentration of H^+ was determined by correcting the concentration (from the completely dissociated HCl) for the change in density from ambient conditions to reaction conditions:

$$\left[\mathrm{H}^+\right]_{T,P} = \left[\mathrm{H}^+\right]_{ambient} \frac{\rho(T,P)}{\rho_{ambient}} \tag{6.1}$$

For neutral conditions, the concentration of H^+ was calculated from the literature values of the dissociation of water (Marshall and Franck, 1981):

$$\left[\mathrm{H}^+\right]_{T,P} = \sqrt{\frac{K_w(T,P)}{\gamma_\pm^2(T,P)}} \tag{6.2}$$

For basic conditions, the concentration of OH^- was determined in the same manner as H+ was in Eqn 6.1:

$$\left[\mathrm{OH}^-\right]_{T,P} = \left[\mathrm{OH}^-\right]_{ambient} \frac{\rho(T,P)}{\rho_{ambient}} \tag{6.3}$$

and then $[H^+]$ was calculated as:

$$\left[\mathrm{H}^+\right]_{T,P} = \frac{K_w(T,P)}{\gamma_\pm^2(T,P)\left[\mathrm{OH}^-\right]_{T,P}} \tag{6.4}$$

$\gamma_\pm$ was calculated using an extended Debye-Huckel approach and found to vary from 1.0 to 1.1 over the conditions studied.

Experiments in the supercritical region were conducted at 450, 550, and 600ºC with the same range of pH solutions. However, under supercritical conditions, HCl and NaOH do not dissociate significantly. Estimates for the concentration of H^+ for these experiments will be discussed in the Results section that follows.

6.4 Results and Discussion

6.4.1 Unimolecular Decomposition Pathway

The transition-state for the unimolecular decomposition pathway was found as an intermediate point in the transfer of a hydrogen atom from a methyl group to the methoxy group. The geometries of MTBE and the transition-state are shown pictorially in Figure 6.1, where the reaction coordinate involves the hydrogen atom traveling from one group to the other. The completion of the reaction would involve the departure of the methanol molecule, leaving isobutene as the other product.

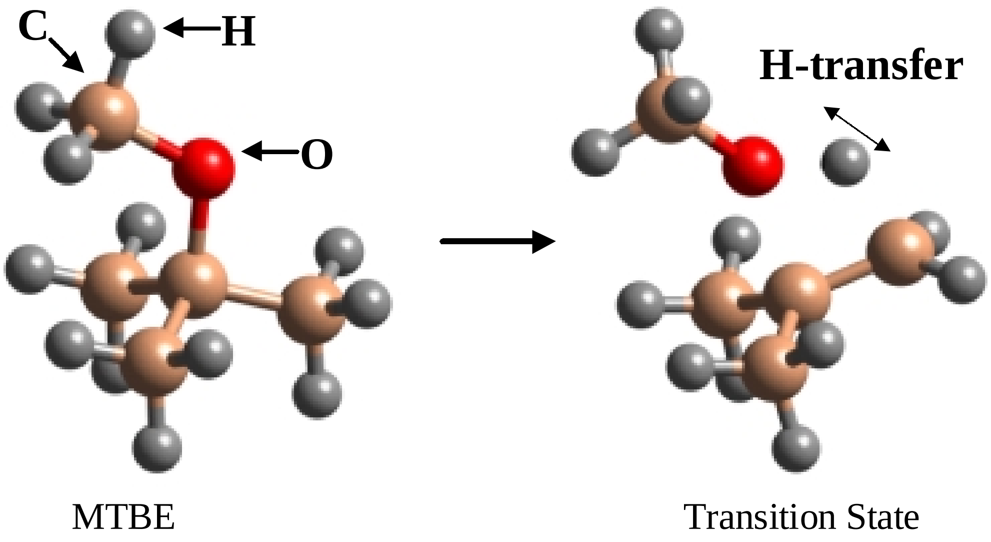

Figure 6.1: Geometries of MTBE and the unimolecular decomposition transition-state calculated with *Gaussian 98* using B3LYP/6-31g(d).

The calculated activation energy for the unimolecular decomposition under vacuum was 251 kJ/mol. The experimentally measured activation energy under very-low-pressure-pyrolysis ($P < 10^{-5}$ bar) was 247 kJ/mol (Choo *et al*., 1974). This type of discrepancy is not unusual for *ab initio* calculations because of their finite sized basis sets. For the purposes of this study, then, the activation energy in a vacuum was set to the value measured experimentally (in low-pressure gas-phase conditions). Calculated changes to the activation energy due to solvation effects are used as a correction to the literature value.

Calculations were performed successfully for all of the supercritical temperatures, but geometry optimizations for the transition state failed to converge for dielectric strengths greater than 7.0 (T = 381.5ºC, P = 250 bar). While this may limit the absolute applicability to the subcritical region, trends can be observed in the successful calculations and used to make approximations over the entire temperature range. Furthermore, the results will show that this pathway does not significantly contribute to the decomposition of MTBE at lower temperatures.

A plot of the dipole moment of MTBE and the transition state are shown as a function of dielectric strength (ε) in Figure 6.2. MTBE has a dipole moment of 0.47 D in a vacuum, then increases with dielectric strength, and finally levels off at ~ 0.6 D as ε gets large (> 5). The transition state has a dipole moment under vacuum conditions of 0.95 D, increases more rapidly with ε initially, and then levels off around 1.4 D. One can see that transition state has a dipole moment that is approximately twice as large as the reactant's dipole moment. The larger dipole moment results in greater stabilization of the transition state as the polarity of the solvent is increased, effectively decreasing the activation barrier.

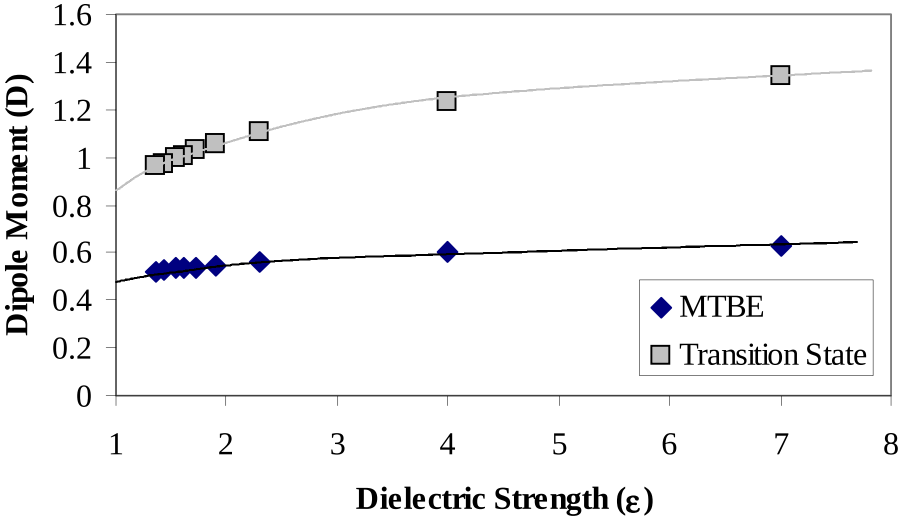

Figure 6.2: Dipole moments of MTBE and transition state versus dielectric strength.

The calculated activation energy as a function of ε is shown in Figure 6.3. The decrease appears approximately linear over this range of dielectric strength. One would expect that the activation energy would eventually level off as the polarity increases further. However, assuming E_a continues to decrease with the same slope should provide the most conservative estimate of the effective activation energy as a function of ε.

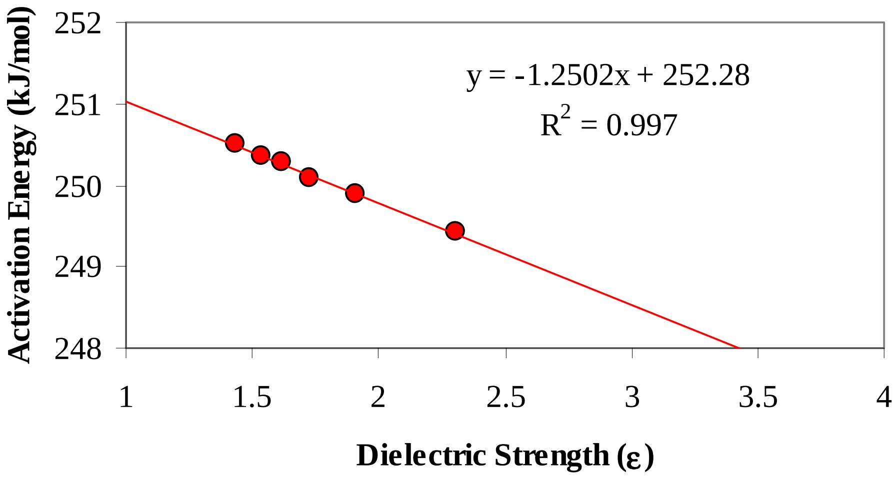

Figure 6.3: Plot of activation energy of unimolecular decomposition versus ε.

Applying this slope as a correction to the rate expression measured in the gas-phase, one obtains:

$$k_{uni} = A\exp\left[\frac{-E_a - f(\varepsilon)}{RT}\right] = 10^{13.9}\exp\left[\frac{-246860 + 1250\cdot\varepsilon}{8.314\cdot T}\right] \tag{6.5}$$

A comparison between the unimolecular decomposition rate constant calculated with Eqn 6.5 and the assumed-first-order rate constant measured in sub-and supercritical water is plotted versus 1000/*T* in Figure 6.4. This plot confirms that the unimolecular decomposition pathway is insignificant to the total reaction rate, except at temperatures greater than 550ºC. The expression for the rate constant in Eqn 6.5 gives a lower bound to the rate that MTBE will decompose at these temperatures. Since the observed rate is significantly faster than predicted in the gas-phase, one can conclude that water must behave as more than just a dielectric medium (i.e. as a reactant and/or catalyst) for the overall reaction. This fact suggests that acid/base hydrolysis may be important.

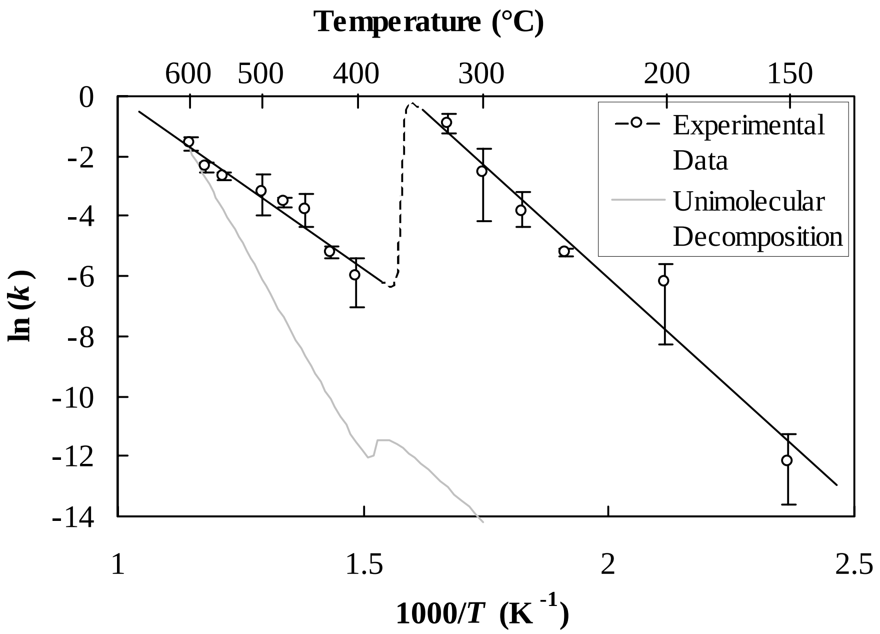

Figure 6.4: Comparison of measured MTBE disappearance rate constant with calculated contribution due to the unimolecular decomposition versus 1000/*T*.

6.4.2 Acid-Catalyzed Hydrolysis Pathway

Subcritical Experiments: In the subcritical region, experiments were performed at 200 and 250ºC (all were at 250 bar). A summary of the experiments conducted at 200ºC and 250 bar is shown in Table 6.1.

Table 6.1: Summary of experiments conducted at 200ºC and 250 bar.

Ambient pH	Calculated pH (200ºC, 250 bar)	# of points	Residence times (s)	Conversion (%)
3	3.1	6	10-120	11-92
3.7	3.8	5	15-180	13-94
7 (neutral)	5.6	6	30-720	5-77
10	7.2	3	30-9900	0-15
11	8.2	3	300-6000	0-1

The only measured products from these experiments were methanol, *t*-butanol, and isobutene. This indicates that no new decomposition pathways that result in additional products are triggered by the addition of acid or base. Furthermore, the relative amounts of each compound produced did not change as a function of pH, nor did the pH change as a function of conversion.

According to the proposed acid-catalyzed mechanism, the experimentally measured rate constant can be written as follows:

$$k_{expt} = k_2 \frac{K_1}{K_{\gamma,H_2O}} \left[\mathrm{H}^+\right] \tag{6.6}$$

And likewise:

$$-\log_{10}(k_{expt}) = -\log_{10}\left(k_2 \frac{K_1}{K_{\gamma,H_2O}}\right) + \mathrm{pH} \tag{6.7}$$

Therefore, a plot of $-\log_{10}(k_{expt})$ versus the pH (where pH = $-\log_{10}(a_{\mathrm{H}^+}) \cong -\log_{10}[\mathrm{H}^+]$) should have a slope of 1. Such a plot is shown in Figure 6.5 for the experiments conducted at 200ºC. The data show fairly linear behavior over most of the pH range, but becomes flatter under acidic conditions. The leveling off at low pH is most likely due to the fact that the reverse reaction is also catalyzed by the concentration of acid. At low pH, the reverse reaction becomes competitive with the forward reaction, and the apparent rate of decomposition is slower than expected. The slope obtained from a least-squares fit of all the data is 0.83 ± 0.35 (to 95% confidence). If we eliminate the data point at the lowest pH (where the reverse reaction is expected to be most significant), the slope increases to 0.94 ± 0.5. The predicted value for the slope of 1.0 is well within the uncertainty of the slope determined experimentally.

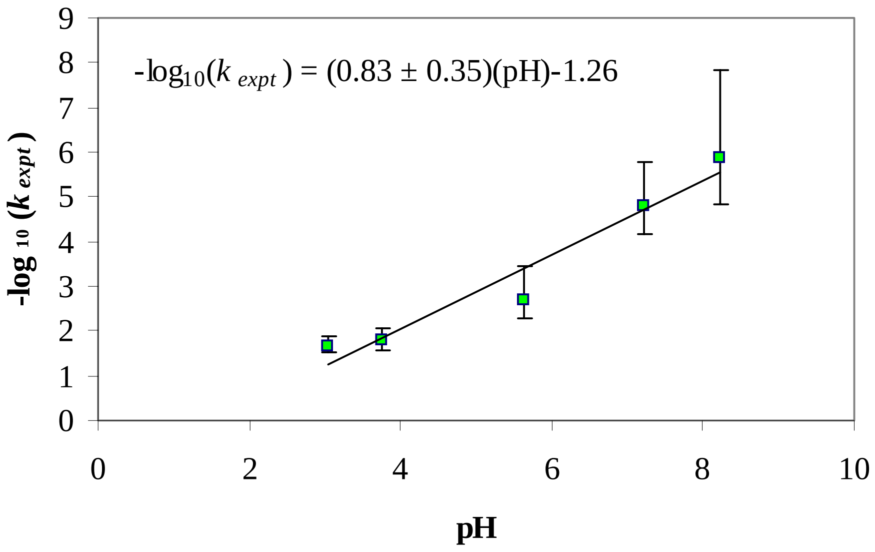

Figure 6.5: MTBE hydrolysis rate constant versus pH at 200ºC and 250 bar.

Similar experiments were conducted at 250ºC (and 250 bar) and are summarized in Table 6.2.

Table 6.2: Summary of experiments conducted at 250ºC and 250 bar.

Ambient pH	Calculated pH (250ºC, 250 bar)	# of points	Residence times (s)	Conversion (%)
3	3.1	4	5-20	84-98
3.7	3.8	5	5-30	61-98
7 (neutral)	5.6	7	30-540	23-93
10	7.1	4	30-5400	1-74
11	8.1	4	60-5400	0-40

Again, the primary products detected were methanol, isobutene, and *t*-butanol. Under neutral and acidic condition, comparable amounts of *t*-butanol and isobutene were produced. However, under basic conditions, significantly more *t*-butanol was produced than isobutene. The measured pH did not change over the course of the reactions, indicating that the products do not significantly alter the pH of the solution (at least at ambient temperatures).

A plot of $-\log_{10}(k_{expt})$ versus pH is shown in Figure 6.6. Similar to the results at 200ºC, the data are linear over most of the pH range but level under acidic conditions. The slope obtained using all of the data points was 0.75 ± 0.19 (to 95% confidence). If the lowest pH data point was omitted, the slope would increase to 0.83 ± 0.15. These values are slightly lower than expected, but given the assumptions in the treatment, are consistent with the proposed acid-catalyzed mechanism.

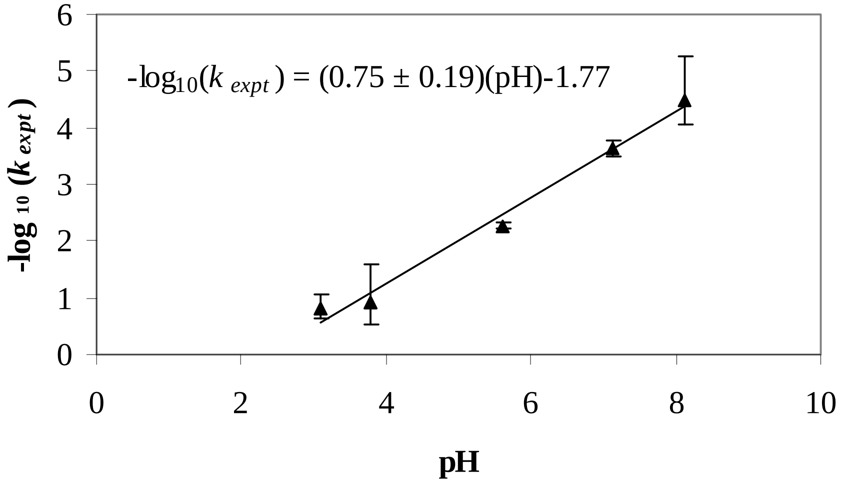

Figure 6.6: MTBE hydrolysis rate constant versus pH at 250ºC and 250 bar.

Supercritical Experiments: In the supercritical region, 250 bar isobaric experiments were conducted at 450, 550, and 600ºC. Calculation of the concentration of H^+ under supercritical conditions is not straightforward due to the small, but significant, degree of dissociation of HCl and NaOH. Furthermore, dissociation constants under these conditions inherently have large uncertainties due to the difficulty of *in situ* experimental measurements under these conditions.

For the experiments in supercritical water, the dissociation constants for HCl and NaOH were calculated using correlations found in the literature (Mesmer et al., 1988). The values used for 450°C and 250 bar (ρ = 109 kg/m^3) were $10^{-13.5}$ for HCl and $10^{-7.0}$ for NaOH. The value for K_w at these conditions was $10^{-18.36}$ (Bandura and Lvov, 2000). Using these values, the concentration of H$^+$ for the acidic conditions were found as follows:

$$\left[\mathrm{H}^+\right] = \sqrt{\frac{K_{HCl}}{K_{\gamma,HCl}}[\mathrm{HCl}]} \tag{6.8}$$

Similarly, the concentration of H$^+$ in the basic experiments was calculated as follows:

$$\left[\mathrm{H}^+\right] = \frac{\dfrac{K_w}{K_{\gamma,H_2O}}}{\sqrt{\dfrac{K_{NaOH}}{K_{\gamma,NaOH}}[\mathrm{NaOH}]}} \tag{6.9}$$

A summary of the experiments, with these assumptions, is shown in Table 6.3.

Table 6.3: Summary of experiments conducted at 450ºC and 250 bar.

Ambient pH	Calculated pH (450ºC, 250 bar)	# of points	Residence times (s)	Conversion (%)
3	8.2	5	7-45	74-90
3.7	8.6	5	5-60	54-90
7 (neutral)	9.2	18	5-60	25-77
10	12.4	4	30-3600	1-44
11	12.9	4	30-1800	0.5-18

It is important to notice that the conversion measured at the first data point increased greatly at lower pH values. This indicates that significant concentrations of the products were present over the course of the measurements. Because the reverse reaction is also acid-catalyzed and at residence times of interest, significant concentration of products exist, the measured (net) rate of MTBE decomposition may be slower than the true forward rate. A comparison of the experimentally measured rate constant versus pH is shown in Figure 6.7. Under basic conditions, the reaction rate slowed down significantly as would be expected. In fact, under basic conditions, the unimolecular decomposition pathway became significant, which complicates the determination of reaction order. The rate constant did increase slightly under acidic conditions, but not to the degree that was predicted by the mechanism. The resulting slope at 450°C was 0.57 ± 0.11 to a 95% confidence interval.

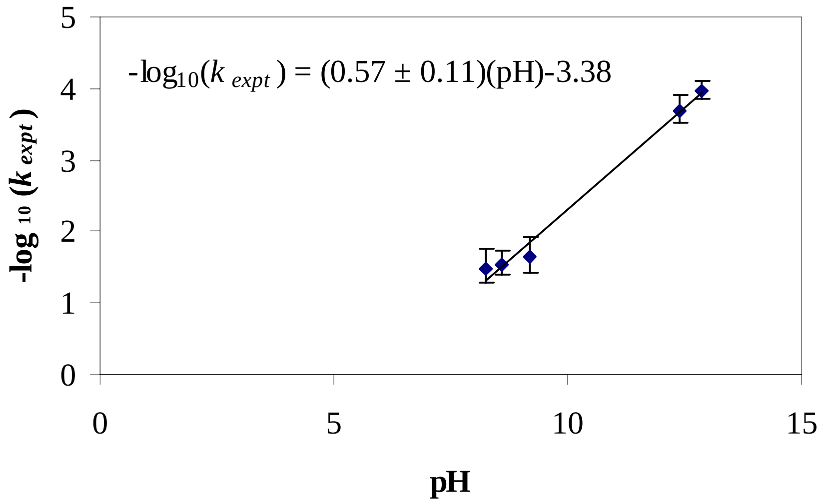

Figure 6.7: Measured rate constant versus pH at 450ºC and 250 bar.

There are several possible explanations for the small slope (relative to the predicted value of 1.0) shown in Figure 6.7. The first is that the reaction occurs via a mechanism different from that proposed in Figure 5.4. While the possibility of a different mechanism could be true, the qualitative behavior of the rate constant is consistent with the proposed mechanism and with the measurements below the critical temperature. Furthermore, any alternative mechanism would have to be acid-catalyzed and have to somehow account for the unique behavior of the reaction order of H^+, which is small for low pH, and greater at high pH. This is highly improbable and the apparent inconsistency is likely a result of other factors.

The discrepancy may be due to uncertainties in the data and to inaccurate values of the dissociation constants estimated for supercritical conditions. For example, there is obviously some scatter in the measured values of the rate constant both above and below the critical temperature (See Figure 6.4). Additionally, the values used for the dissociation constants have large uncertainties. This is demonstrated by the discrepancy in values of K_w reported for supercritical conditions, as discussed in the Appendix (Bandura and Lvov, 2000; Marshall and Franck, 1981).

A third explanation for the apparent inconsistency of the data lies in the experimental technique used in this study. Note that the measured rate constant (k_{expt}) corresponds to the net decomposition rate measured over a range of conversions (which begin with a nonzero value). The inability to measure initial rates is due to the finite mixing and heatup times that follow injection of the cold organic sample (MTBE). Therefore, to obtain good rate constant values, the reverse reaction must be insignificant relative to the forward reaction rate. Yet, Antal and coworkers have reported the formation of ethers in the dehydration of alcohols in sub- and supercritical water as acid-catalyzed (Xu *et al*., 1997; Antal *et al.*, 1998). Accordingly, the reverse reaction rate would increase proportionally as the concentration of acid is increased. Also, notice that the conversion before the first data point is greatest at low pH, indicating the initial rate is fastest. Therefore, because the initial conversion is higher, more products are available to participate in the reverse reaction and the measured decomposition rate is slower than the true forward reaction rate.

Experiments at both 550 and 600ºC were conducted at one acidic pH and one basic pH in addition to the original experiment at neutral. The reaction rate measured under acidic conditions was too fast for our apparatus, showing nearly complete conversion in less than 5 s. A summary of the experiments and results for neutral and basic (ambient pH = 10.0) is shown in Table 6.4.

Table 6.4: Experiments and results of MTBE hydrolysis at 550 and 600°C and 250 bar under neutral and basic conditions.

T **(ºC) and pH**	**# of points**	**Residence times (s)**	**Conversion (%)**	**k_{expt} (s^{-1})**
550 neutral	7	5-40	68-97	0.069
550 basic	7	15-180	19-97	0.020
600 neutral	6	5-30	84-99.5	0.21
600 basic	6	5-40	55-99	0.14

Under basic conditions, only very small amounts of *t*-butanol were detected, indicating that the reaction pathway switched to favor isobutene. Trace amounts of acetone were also detected, which is one of the primary intermediates in the oxidation of *t*-butanol. This presence of acetone may indicate some reaction of *t*-butanol with NaOH occurred. A shift to isobutene as the favored product is consistent with the unimolecular decomposition pathway becoming competitive with the hydrolysis pathway at high temperature.

In Table 6.4, it is clear that the rate constant under basic conditions (pH ≥ 13) is smaller than the value at neutral conditions (pH ≈ 10.8 to 11.0). Additionally, the conversion observed before the first data point is smaller under basic conditions. This is consistent with the acid-catalyzed mechanism. It is difficult to quantify the effect of the concentration of H^+ under these conditions for two reasons. The first reason is that dissociation constants for HCl and NaOH are not reported above 450ºC. Secondly, the unimolecular decomposition is competitive with the hydrolysis pathway and cannot be neglected.

6.4.3 Discussion

A plot that includes all of the calculations and measurements from this study is shown in Figure 6.8. The experiments conducted with acidic solutions are shown as triangles and show a faster rate than the neutral experiments (diamonds). The experiments with basic solutions (circles) show slower kinetics than those conducted with pure deionized water (neutral). Note: pH values reported in the legend of the chart represent the values at ambient conditions. The thin line labeled Eqn 6.5 is the modified rate constant of the unimolecular decomposition, which incorporates the correction to the activation energy due to solvent effects.

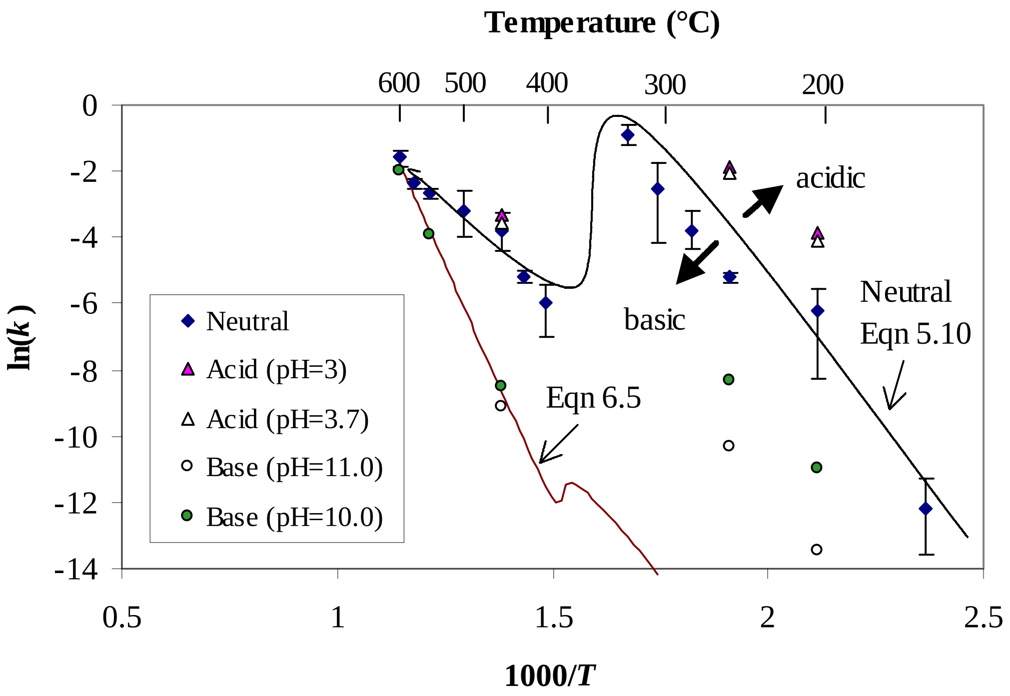

Figure 6.8: Summary of all MTBE hydrolysis experiments with varying pH and comparison to calculated values of the unimolecular decomposition rate constant.

In the experiments at supercritical temperatures, the unimolecular decomposition rate set the lower limit on the total measured reaction rate. As the concentration of H^+ decreased, the relative importance of this 'minor pathway' increased and became the dominant mechanism of decomposition. By adding excess base, the rate of acid-catalyzed pathways could be slowed down to the point where gas-phase reaction pathways could be measured. Furthermore, this limiting behavior verified the applicability of using gas-phase kinetic expressions to model reactions in supercritical water.

6.5 Conclusions

Reaction pathways of MTBE decomposition in sub- and supercritical water were analyzed to establish the importance of acid/base catalyzed hydrolysis in comparison to unimolecular decomposition. Computational tools were employed to correct the activation energy of the gas-phase unimolecular decomposition pathway. Although correcting for solvent effects decreased the activation barrier from the value in the gas-phase, the pathway did not contribute to the overall reaction rate for temperatures less than 550°C. However, the unimolecular decomposition rate set a lower bound on the reaction rate for each temperature.

Experiments were conducted to measure the effect of pH on the decomposition rate of MTBE. The reaction rate increased under acidic conditions and decreased under basic conditions, which was consistent with the proposed acid-catalyzed reaction mechanism. The reaction order with respect to H^+ was found to be 0.83 ± 0.35 and 0.75 ± 0.19 (to 95% confidence) at 200 and 250°C (250 bar). These slopes were similar to the value of 1.0 predicted by the proposed mechanism. The discrepancy between measured and predicted values was most likely caused by the reverse reaction becoming more significant under acidic conditions. The leveling off of the net experimental rate constant at low pH values supports this hypothesis.

The dependence of the reaction rate on pH at supercritical temperatures verified that the dominant reaction pathway is acid-catalyzed in that region, too. Quantifying the dependence on pH was difficult due to the high uncertainty in values for dissociation constants of HCl and NaOH in the supercritical region. However, the reaction order measured at 450°C was 0.57 ± 0.19. The apparent discrepancy between the measured slope and the predicted value of 1.0 was most likely due to two factors. The first is that the measured reaction rate under basic condition included contributions from both the acid-catalyzed pathway and from the unimolecular decomposition pathway. Secondly, the measured reaction rate under acidic conditions was slower due to the reverse reaction. Experiments at 550 and 600°C under basic conditions were also conducted and the measured rate was equal to that predicted by the unimolecular decomposition pathway within experimental uncertainty.

These results confirm that the primary decomposition pathway of MTBE in both sub- and supercritical water involves acid-catalysis. Although the reaction order for H^+ was not conclusively verified over the entire temperature domain, the mechanism and rate expression developed in Chapter 5 are in reasonable agreement with the conclusions reached in this study.

6.6 References

Antal Jr., M. J., M. Carlsson, X. Xu, and D. G. M. Anderson (1998). “Mechanism and kinetics of the acid-catalyzed dehydration of 1- and 2-propanol in hot compressed liquid water.” *Industrial & Engineering Chemistry Research* **37** (10): 3820.

Balbuena, P. B., K. P. Johnston, and P. J. Rossky (1995). “Computer-simulation study of an S_N2 reaction in supercritical water.” *Journal of Physical Chemistry* **99** (5): 1554.

Bandura, A. V. and S. N. Lvov (2000). "The ionization constants of water over a wide range of temperatures and densities." *Steam, water, and hydrothermal systems: Physics and chemistry meeting the needs of industry*. P. R. Tremaine, P. G. Hill, D. E. Irish and P. V. Palakrishnan, Eds. NRC Press, Ottawa.

Bennett, G. E., P. J. Rossky, and K. P. Johnston (1995). “Continuum electrostatics model for an S_N2 reaction in supercritical water.” *Journal of Physical Chemistry* **99** (43): 16136.

Chandler, K., F. H. Deng, A. K. Dillow, C. L. Liotta, and C. A. Eckert (1997). “Alkylation reactions in near-critical water in the absence of acid catalysts.” *Industrial & Engineering Chemistry Research* **36** (12): 5175.

Choo, K.-Y., D. M. Golden and S. W. Bensen (1974). “Very low-pressure pyrolysis (VLPP) of *t*-butylmethyl ether.” *International Journal of Chemical Kinetics* **6**: 631.

Frisch, M. J., G. W. Trucks, H. B. Schlegel, P. M. W. Gill, B. G. Johnson, M. A. Robb, J. R. Cheeseman, T. Keith, G. A. Petersson, J. A. Montgomery, K. Raghavachari, M. A. Al-Laham, V. G. Zakrzewski, J. V. Ortiz, J. B. Foresman, J. Cioslowski, B. B. Stefanov, A. Nanayakkara, M. Challacombe, C. Y. Peng, P. Y. Ayala, W. Chen, M. W. Wong, J. L. Andres, E. S. Replogle, R. Gomperts, R. L. Martin, D. J. Fox, J. S. Binkley, D. J. Defrees, J. Baker, J. P. Stewart, M. Head-Gordon, C. Gonzalez, and J. A. Pople (1995). *Gaussian, Inc*., Pittsburgh, PA.

Lesutis, H. P., R. Glaser, C. L. Liotta, and C. A. Eckert (1999). “Acid/base-catalyzed ester hydrolysis in near-critical water.” *Chemical Communications* **20:** 2063.

Krammer, P. and H. Vogel (2000). “Hydrolysis of esters in subcritical and supercritical water.” *Journal of Supercritical Fluids* **16**: 189.

Marrone, P. A., P. M. Gschwend, K. C. Swallow, W. A. Peters and J. W. Tester (1998). “Solvation effects on kinetics of methylene chloride reactions in sub and supercritical water: Theory, experiment, and ab initio calculations.” *Journal of Physical Chemistry A* **102** (35): 7013.

Marshall, W. L. and E. U. Franck (1981). “Ion product of water substance, 0-1000°C 1-10,000 bars. New international formulation and its background.” *Journal of Physical Chemistry Reference Data* **94** (2): 295-304.

Mesmer, R. E., W. L. Marshall, D. A. Palmer, J. M. Simonson, and H. F. Holmes (1988). "Thermodynamics of aqueous association and ionization reactions at high temperatures and pressures." *Journal of Solution Chemistry* **17** (8): 699.

Narayan, R. and M. J. Antal Jr. (1990). “Influence of pressure on the acid-catalyzed rate constant for 1-propanol dehydration in supercritical water.” *Journal of the American Chemical Society* **112**: 1927.

Penninger, J. M. L., R. J. A. Kersten and H. C. L. Baur (1999a). “Hydrolysis of diphenylether in supercritical water: Effects of dissolved NaCl.” *Journal of Supercritical Fluids* **17**: 215.

Penninger, J. M. L., R. J. A. Kersten and H. C. L. Baur (1999b). “Reactions of diphenylether in supercritical water - mechanism and kinetics.” *Journal of Supercritical Fluids* **16**: 119.

Pomelli, C. S., and J. Tomasi (1997). “*Ab initio* study of the S_N2 reaction $CH_3Cl + Cl^- \rightarrow Cl^- + CH_3Cl$ in supercritical water with the polarized continuum model.” *Journal of Physical Chemistry A* **101** (19): 3561.

Salvatierra, D., J. D. Taylor, P. A. Marrone and J. W. Tester (1999). “Kinetic study of hydrolysis of methylene chloride from 100 to 500C.” *Industrial & Engineering Chemistry Research* **38** (11): 4169.

Siskin, M., and A. R. Katritzky (2000). “A review of the reactivity of organic compounds with oxygen-containing functionality in superheated water.” *Journal of Analytical and Applied Pyrolysis* **54** (1-2): 193.

Xu, X. D., and M. J. Antal Jr. (1994). “Kinetics and mechanism of isobutene formation from *t*-butanol in hot liquid water.” *AIChE Journal* **40** (9): 1524.

Xu, X., M. J. Antal Jr. and D. G. M. Anderson (1997). “Mechanism and temperature-dependent kinetics of the dehydration of *tert*-butyl alcohol in hot compressed liquid water.” *Industrial & Engineering Chemistry Research* **36** (1): 23.

Chapter 7

Design and Construction of New SCWO Reactor

A new SCWO reactor was designed and built for improved capabilities in the laboratory. Dr. Phil Marrone, Dr. William Peters, and Professor Jefferson Tester determined the initial requirements for the design of the reactor, which was built soon after my arrival to the group. This chapter describes the advantages and capabilities of the reactor system and provides details of the components in the experimental apparatus. Operating procedures and a summary of preliminary experiments conducted with the system are included as well.

7.1 Motivation for Large Tubular Reactor

Historically, SCWO kinetic studies have been performed on a small-scale, tubular plug-flow reactor. The system was originally built when research on SCWO was begun in our group (Helling and Tester, 1987), and has evolved over time to incorporate several system improvements (Dinaro *et al.*, 2000). Because of its simple design and reliability, our group has used the plug-flow reactor system extensively for measuring kinetics.

The small plug-flow reactor system has several inherent limitations, however, and these are enumerated below:

1) *Reactions in the preheater:* Because organics are fed to the reactor in aqueous solutions, the feed streams are typically preheated to reactor temperatures prior to their introduction into the reactor. This becomes a problem for species that react in

hydrothermal water in the absence of oxygen. For example, MTBE and CH_2Cl_2 both hydrolyze in subcritical water, making isothermal reaction rates difficult to measure.

2) *Concentration limitations:* In the plug-flow reactor system, feed solutions are prepared by dissolving the organic and oxygen into water in separate feed tanks. The aqueous streams are then pumped into the reactor system. For species that are sparingly soluble in water, this poses a maximum concentration limit on the conditions for study. The problem of oxygen solubility was eliminated by the implementation of hydrogen peroxide feed solutions, where the H_2O_2 breaks down into H_2O and 1/2 O_2 in the preheater section. However, the limitation on maximum organic concentration remains. This is especially a problem for nonpolar reactants such as benzene or hexane.

3) *Residence time limitations:* The range of accessible residence times in the plug-flow system is determined by the reactor volume, the density of the reacting mixture, and the range of possible pump flow rates. With the current reactor and pumps, the achievable residence times range from approximately 2 to 15 s for typical supercritical water densities. This range of residence times is ideal for many oxidation reactions, such as those studied in our laboratory to date. However, for hydrolysis reactions, the time scales are much longer than the capability of the plug-flow reactor. Furthermore, very short residence times are desirable for fast reactions or to probe into the apparent induction time observed in some of the systems previously studied.

4) *Wall effects and metal catalysis:* There has been some concern about the possible effects of metal surfaces on reaction kinetics in SCWO. These effects range from catalysis of the nickel walls to radical quenching by collisions with metal surfaces.

Several studies in our group, using two or more different reactors in the plug-flow system, have shown effects of surface area on the reaction rate (for example, see Webley *et al*., 1991). Due to the small volume of the reactor, wall effects could play a significant role in the measured kinetics. However, the goal of our research is to provide intrinsic homogeneous reaction kinetics that are not dependent on wall reaction chemistry specific to any reactor system.

5) *Sampling limitations:* With the current plug-flow reactor, only one "data point" may be measured for a set of feed compositions and pump settings. In order to measure different residence times, the flow rate settings on the pumps must be changed and the system allowed to reach steady-state (which may take in excess of one hour). Furthermore, if wall effects are significant, changing the flow conditions could increase the turbulence and thus affect the conversion measured.

6) *Ex situ composition measurements:* In the plug-flow system, reactor effluent is quenched to ambient temperature and depressurized prior to composition measurement. By this process, any species that are stable under supercritical water conditions but unstable in ambient water will further react. To identify reaction pathways and accurately model reactions, detection of these reactive intermediates would be beneficial.

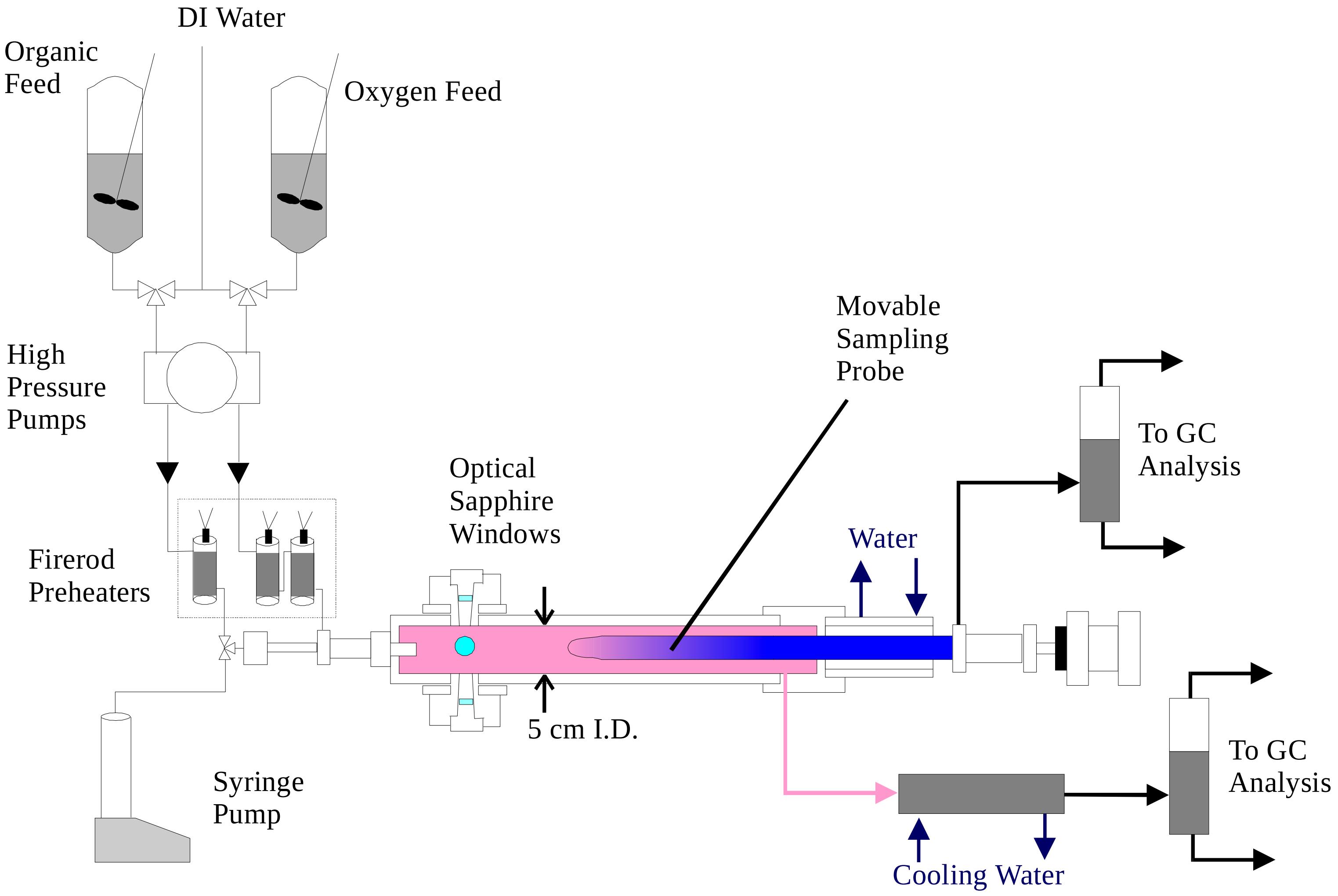

Figure 7.1: Schematic of large tubular SCWO reactor system at MIT.

7.2 Advantages of the New SCWO Reactor System

With the objective of overcoming these limitations of the existing plug-flow reactor, a new SCWO reactor system (shown in Figure 7.1) was designed and built. The system is capable of temperatures up to 650°C and pressures up to 300 bar. The specific advantages of the new reactor system are as follows:

1) The system was designed so that a pure organic stream may be fed directly to the reactor using a syringe pump. The pure organic stream is pumped through a water-cooled tube to a coaxial reactor inlet. In this inlet, the organic is fed down the centerline, and a water or water/oxygen stream enters in a surrounding cylinder. By this design, the organic is not preheated until it enters the reactor. This minimizes hydrolysis reactions and reactant decomposition prior to entering the reactor.

2) Because of the direct injection of the organic, the initial concentration of organic is not limited by the ambient solubility of the reactant in water. This allows for a much broader range of composition studies.

3) The reactor was designed with a movable sampling probe. The probe can be positioned at any location along the centerline of the reactor from 0.75 in. (1.9 cm) to 18.75 in. (47.6 cm) from the inlet. This results in a variable length reactor, where the accessible residence times — without changing the flow rate — ranges over a factor of 25. For example, at an ambient flow rate of 20 mL/min and a reactor temperature of 500ºC, the accessible residence times range from 5 to 130 s. If the pump flow rate is increased to 130 mL/min, the range of residence times decreases to 0.8 to 20 s. Therefore, the composition can be measured at residence times of 0.8 to 130 s at 500ºC for this range of pump flow rates.

4) The reactor has a 2 in. (5.08 cm) inner diameter and is designed to be operated in the laminar flow regime. This design feature exists to minimize (or even eliminate) contact of the fluid with the walls. Since the reactant feed and product sampling are conducted along the centerline, fluid elements in this region will theoretically never contact the reactor walls. This allows us to measure the pure hydrolysis or oxidation kinetics without possible effects of wall catalysis or radical quenching.

5) Since the sampling probe may be moved while the reactor is maintained at constant temperature and pressure (neglecting pressure deflections caused while moving the probe), it is possible to measure composition at many different axial locations without changing any of the reactor conditions. This can be accomplished by measuring composition at one location, slowly moving the probe forward and allowing equilibration, and then measuring another data point, and so on.

6) The new SCWO reactor system was also equipped with optical accessibility for *in situ* spectroscopic measurements. The design includes three sapphire windows at 90° angles located at a distance of 2.75 in. (7.0 cm) from the inlet. With these windows, Raman spectroscopy (or other spectroscopic tools) can be used with back-scattering or right-angle scattering (or transmission) for determination of compositions without quenching and sampling via gas chromatography.

7.3 Description of the New Reactor System Components

7.3.1 Upstream Feed Delivery and Preheating Section

The primary feed stream to the reactor is either a deionized water stream (for hydrolysis runs) or a hydrogen peroxide solution (for oxidation runs). 18.0 MΩ (megaohms) water (purified with a Barnstead Nanopure system described in Chapter 3) is stored in a 30 gallon (120 L) storage tank (Nalgene p/n 11102-0030) and degassed by bubbling helium through it for at least 5 minutes. A helium head pressure of 5 psig (0.3 bar) is maintained above the water feed. For oxidation experiments, a hydrogen peroxide solution is prepared and stored in another 30 gallon (120 L) storage tank with a helium head pressure of 5 psig (0.3 bar). A 3-way valve (Whitey p/n SS-43XS4) allows interchange between the two feed tanks. Water or peroxide solutions are pumped with a preparative HPLC pump (Rainin (now Varian) model SD-1). The pump is nominally capable of flows up to 200 mL/min and pressures up to 6000 psig (414 bar); however, at flow rates above 150 mL/min, vibrations (audible) in the pump increase and cavitation becomes a concern. The pump is equipped with a pressure transducer and pressure fluctuations are less than 30 psig under typical operating conditions. Additionally, a pressure gauge (Northwest Engineering p/n EOP-GF) is connected to the aqueous feed line for a second measurement.

The water (or peroxide solution) feed is preheated by two Watlow, ‘Made-to-order’ Firerod cartridge heaters in series. Each heater is 12 inches long with a 0.75 in. (1.9 cm) diameter and delivers 3000 W of heat (at 208 VAC). The Firerods are equipped with an internal type-K thermocouple to monitor the temperature of the heating elements, which may not exceed 800°C. Each Firerod is inserted into a 1.5 in. O.D. aluminum rod that was bored out to fit tightly around the heater. Each Firerod assembly has 40 feet of 1/8 (3.2 mm) in. O.D. (0.028 in. wall thickness) Inconel 625 tubing tightly coiled around the aluminum. The water/oxidant feed is pumped through this tubing and preheated to the desired reactor temperature.

The temperature is measured at the end of the two preheater assemblies with a type-K thermocouple inserted into the flowing stream. A PID temperature controller (Omega model CN9000A) is used to control the effluent temperature from the preheaters. One phase, 208 VAC power is delivered to the preheater from a silicon control rectifier (Omega p/n SCR71Z-260). Each preheater assembly is wrapped in 6 lb. (2.7 kg) Fiberfrax Durablanket S insulation and contained in a box made of insulating ceramic fiberboard. In the preheater, hydrogen peroxide solutions react completely to produce H_2O and 1/2 O_2. The preheated water (with or without oxygen) stream then flows through a 12 in. (30 cm) section of insulated 1/16 in. (1.6 mm) O.D. C-276 tubing to the inlet section of the reactor.

The organic stream can be fed to the reactor as either a pure organic stream or as a preheated aqueous stream. For compounds that do not hydrolyze and that have appreciable solubility in water, aqueous solutions may be prepared and stored in a 5 gallon (20 L) storage tank. No pump currently exists for this option, but such a pump would be expected to have a maximum flow rate of approximately 30 mL/min. The solution would be preheated with one 3000 W Firerod preheater assembly (as described previously) and then be fed into the reactor inlet. Alternatively, pure organics are fed directly to the reactor using a syringe pump (ISCO model 100DM). With this feed option, organics are not preheated until they enter the main reactor, thus eliminating decomposition due to hydrolysis. The syringe pump has a reservoir of 103 mL and can deliver pulseless flow over a range of 10 µL/min up to 25 mL/min at pressures up to 10,000 psig (680 bar).

7.3.2 Reactor Specifications and Capabilities

The reactor consists of a coaxial inlet, a main reactor tube, a window assembly, and a sampling probe. The entire assembled reactor is shown schematically in Figure 7.1 and pictorially in Figure 7.2. The entire reactor is mounted on an iron table (8 ft. 2 in. (2.5 m) long by 8 in. (20 cm) wide) supported by four legs. A 6 ft. x 4 in. x 1 in. (1.8 m x 10 cm x 2.5 cm) piece of iron is mounted on each side of the main vessel along the length of the reactor. Each piece of iron is secured to the table with 6 cap screws and must be in place before pressurizing the reactor. These iron pieces prevent the iron table from bowing under the pressure of the system. A 1 in. (2.54 cm) thick piece of rigid ceramic sheet (Zircar p/n RS-100) was cut to insulate each contact point between the reactor and the table. This sheet insulation raises the entire reactor (inlet, main tube, window assembly, and sampling probe) up off of the table and thermally insulates the reactor, where otherwise there would be direct metal-to-metal contact. Furthermore, the extra inch of lift allowed Fiberfrax Durablanket insulation to be wrapped around the remainder of the reactor length.

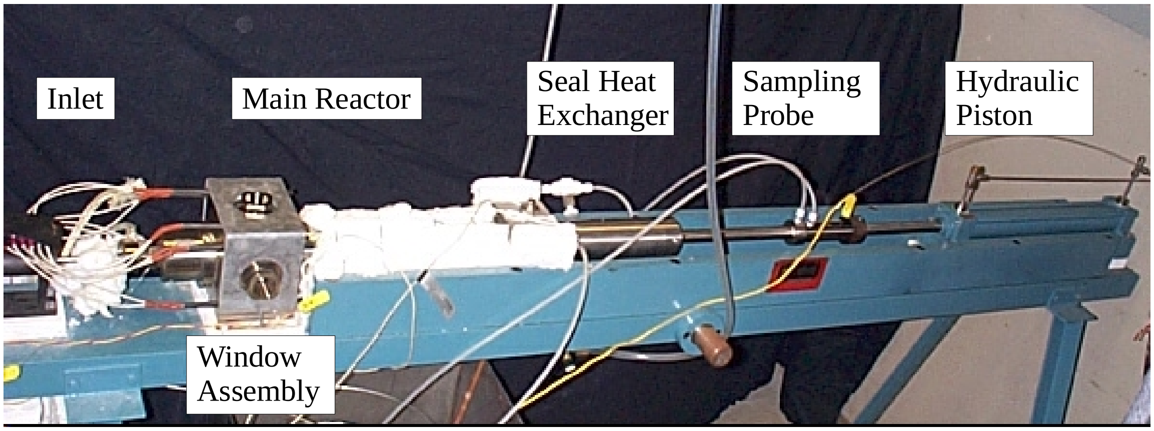

Figure 7.2: Picture of the new SCWO reactor (as assembled)

A photograph of the reactor inlet is shown in Figure 7.3. The inlet consists of several coaxial tubes, with a 1/32 in. (0.8 mm) type-K thermocouple inserted through the innermost tube. The thermocouple may be extended beyond the tip of the inlet or retracted into the inlet tube. Currently, the thermocouple is placed 1/2 in. (1.3 cm) beyond the tip of the inlet. The innermost tube has an O.D. of 1/8 in. (3.2 mm) (wall thickness of 0.02 in.) and provides the channel where the organic is fed to the reactor. The organic feed is connected to the inlet assembly with a modified 1/16 in. (1.6 mm) C-276 HiP (AM1) fitting and may be fed either as a preheated aqueous solution or as a pure, cold organic stream.

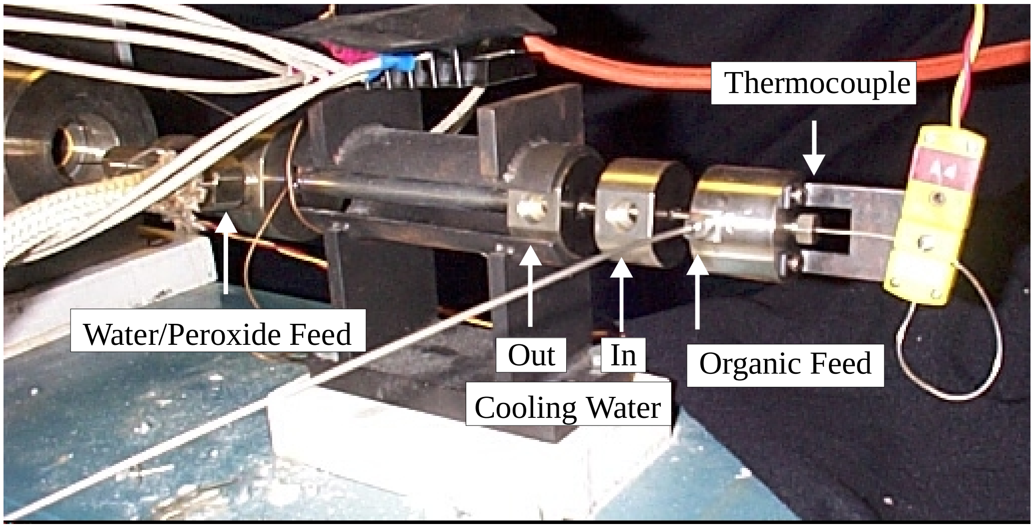

Figure 7.3: Photograph of inlet assembly for large tubular reactor.

Surrounding the organic feed tube are two concentric tubes (1/4 in. O.D. x 0.035 in. wall and 3/8 in. O.D. x 0.035 in. wall) where ambient water may flow to keep the organic feed cool prior to the reactor entrance. Cooling water is fed to the inner tube through an NPT port at the back of the inlet, and returns from the tip of the inlet through the outer tube. Near the entrance to the reactor, the preheated water or water/oxygen solution is connected with a 1/8 in. (3.2 mm) HiP fitting and is fed into the reactor around the annulus of the organic feed. The water is fed in an axial flow direction, but the inlet may be modified to include a small mixing volume at the reactor entrance in the future if desired by subsequent operators.

From the inlet, the solutions enter the main reactor tube where they may mix and begin to react. The main reactor consists of a 3 in. (7.6 cm) long C-276 tube (3 in. O.D. x 0.5 in. wall), followed by the window assembly, and then another 14 in. (36 cm) long C-276 tube (3 in. O.D. x 0.5 in. wall). The large tubing is connected to the window assembly block and to the exit support block by a custom c-seal (Pressure Science Inc. p/n 614A59-0032-C) with large glands around the circumference of the tubing. The c-seals have a cross-section shaped like a ‘C’ with the open cavity toward the pressurized fluid. These are designed so that as the pressure increases, the fluid fills the cavity, pushes the sides of the seal outward, and improves the sealing ability.

The short reactor tube that connects the inlet to the window block is wrapped with a 313 W high temperature heating tape (Omega p/n STH051-040). The heater is surrounded by one layer of Fiberfrax Durablanket S (6 lb.) insulation held in place with copper wire. The temperature of the reactor wall is measured by a 1/32 in. (0.8 mm) type-K thermocouple cemented to the reactor with Lynn Fiber Bond high-temperature (1260°C) cement. The wall temperature is controlled by an Omega PID controller (CN9000A) connected with a solid state relay (Omega p/n SSR240DC45) that delivers 110 VAC power to the heating tape. The fluid temperature in this section is measured by the thermocouple in the inlet, but cannot be controlled directly by the heating tape due to the long time delay between when heat is input and a temperature change is measured.

The window assembly is a 6 in. x 6 in. x 4.5 in. (15 x 15 x 11 cm) block of Hastelloy C-276 with a fitting machined in each face of the block. On the front and back sides are fittings that accept the large diameter tube that makes up the main reactor. On the top and each side of the block are fittings that accept sapphire window enclosures. The window enclosures are internally sealed before they are inserted into the block, and they are described in the thesis of Matthew DiPippo (1998). The bottom port on the block can accept a fourth window enclosure or an adapter that allows a 1/32 in. (0.8 mm) type-K thermocouple to be inserted into the middle of the block (as is currently being used). The wall temperature is measured by another 1/32 in. (0.8 mm) type-K thermocouple cemented onto the block. Heat is delivered to the window block by six 125 W strip heaters mounted around the block with a rigid aluminum jacket. The wall temperature is controlled by an Omega PID controller (CN9000A) with a solid state relay (SSR240DC45) and 110 VAC. The faces of the block are insulated with sheets of Durablanket S (6 lb.) with holes cut out for the windows and held in place by several pieces of copper wire.

The longer section of main reactor tube that connects the back side of the window block to the reactor outlet block is wrapped in a wide, heavy insulated, 940 W heating tape (Omega p/n SWH251-040). The wall temperature is measured by a 1/32 in. (0.8 mm) type-K thermocouple cemented to the wall and controlled by a CN9000A with an SSR delivering 110 VAC.

The reactor is designed to operate with laminar flow and therefore one can assume that the velocity is parabolic throughout the reactor:

$$v(r) = \frac{2\dot{m}}{\rho A}\left[1-\left(\frac{r}{R}\right)^2\right] \tag{7.1}$$

Assuming radial diffusion is negligible, the residence time from the inlet to the sampling probe at a length, *l*, can be calculated using the velocity of the fluid along the centerline of the reactor.

$$\tau = \frac{l}{v(0)} = \frac{l\rho A}{2\dot{m}} \tag{7.2}$$

Alternatively, if radial diffusion is significant, one cannot assume that each fluid element travels straight down the centerline of the reactor. For the extreme case of very fast radial diffusion, the reactor may be treated as plug-flow.

$$\tau = \frac{l}{v(\text{average})} = \frac{l\rho A}{\dot{m}} \tag{7.3}$$

It is unlikely that either of these assumptions is totally accurate for all operating conditions, so residence time distribution studies will need to be undertaken to characterize the reactor.

When cold organic is fed to the reactor, the assumption of laminar flow may be invalid due to natural convection. This is because the direction of flow is perpendicular to the force of gravity, so density differences will lead to asymmetries in the flow field (Peters, 2000). Natural convection has been shown to perturb flow patterns in transpiring wall SCWO reactors (Lieball *et al.*, 2001), and may be a factor in our system. The impact of natural convection on the flow is unclear. On one hand, the very small flow of the organic stream should allow for rapid heatup upon mixing with the water/oxidant stream, which has a flowrate approximately 3 orders of magnitude higher. On the other hand, with the current coaxial feed design, mixing at the inlet may not be very efficient. The cumulative effects of flow non-idealities will have to be measured experimentally with residence time distribution studies. If the effects of natural convection disturb the flow significantly, the reactor can be oriented vertically to reduce the radial mixing. Furthermore, modification to the inlet nozzle would be trivial if increased mixing of the streams were desired.

7.3.3 Sampling and Measurements

The reactor is equipped with a sampling probe that extends along the axial length of the reactor. The sampling probe enters the main reactor through the reactor outlet block with a sophisticated sealing mechanism that allows the probe to be moved while the system is at supercritical temperatures and pressures. The sealing mechanism consists of a hot seal, a shell and tube heat exchanger, and a cool, primary seal. The hot seal prevents flow of the hot fluid into the heat exchanger but does not provide the main pressure seal. The heat exchanger serves to cool the probe so that the primary seal may be made at a lower temperature. The primary pressure seal is made by two circular washers with opposing triangular cross-sections (▲▼) that can slide along the shaft of the sampling probe while it is moving, and make a tight seal when the probe comes to rest at the desired position.

The sampling probe has a 1 in. O.D. (2.54 cm) with a tapered tip to minimize drag. The sample stream continuously flows in the innermost tube, which is 1/8 in. O.D. (3.2 mm). Inside the sample tube is a 1/32 in. (0.8 mm) type-K thermocouple that extends down the entire length of the probe. The thermocouple may be withdrawn into the sample tube but is typically 0.5 in. (1.3 cm) beyond the tip of the probe.

Similar to the inlet assembly, two coaxial channels around the sample tube allow for cooling water to flow along the entire length of the sample probe. The cooling water inlet and outlet are connected with two NPT fittings at the back end of the probe. The water enters through the inner channel, quenching the reaction in the sample tube. The water then flows back through the outer channel and exits the probe.

The flow rate of the sample is controlled by a Hoke micro-metering valve (p/n 1656G2Y) with a digital readout knob (p/n 1600K1). The desired flow rate for the sample is calculated so that the volumetric flow along the centerline, with a cross-sectional area equal to the sample tube, is drawn into the probe. Assuming that the velocity profile is uniform over this open area of the sampling probe, the desired flow rate is calculated as follows:

$$F_{sample} = v(0) \cdot A_{sample} \frac{\rho(T,P)}{\rho_{ambient}} \tag{7.4}$$

where F_{sample} is the volumetric flow (mL/min) of the sample line, and:

$$A_{sample} = \pi \left(\frac{d_{sample}}{2} \right)^2 = 3.7 \text{ mm}^2 \tag{7.5}$$

This calculation defines an upper bound on the sample flow, but smaller flows are acceptable. If the flow rate through the sample tube is set to a higher value than that calculated with Eqn 7.4, then fluid elements would be drawn from a larger cross-section of the main reactor tube. This would result in a larger effective residence time due to the distribution of specific residence times among the fluid elements drawn in the sample.

After passing through the metering valve, the sample stream is at ambient pressure and temperature. Any gases no longer soluble in water will segregate into a second fluid phase. The stream is directed into a vertical tube packed with glass beads to separate the two fluid phases. The gas phase exits from the top of the separator and through a soap bubble flow meter. Samples are taken from the gas phase via a septum and analyzed by gas chromatography. The liquid phase exits the bottom of the phase separator, where the flow rate is measured using a stopwatch and a graduated cylinder. Liquid samples are collected in small, amber vials and analyzed via GC.

A hydraulic piston mounted on the iron table with the reactor (on 1 in. of rigid insulator board) is used to move the sampling probe. Hydraulic oil is pumped with a Rexroth pump (p/n PP2.5/P1-9/1S/BM1) into chambers on either side of the piston, causing the probe to move forward or backward. A 3-way electric switch allows the operator to control the movement of the probe.

Additionally, the reactor is designed so that it may be interfaced with *in situ* Raman spectroscopic measurements. With this configured, the laser would be focused through the side window and into the center of the reactor. Scattered light (90°) would be collected from the top window and focused onto a spectrometer, where it would be analyzed for shifts in its wavelength. The location of the window assembly is fixed at 2.75 in. (7 cm), but could be modified by constructing different lengths of the two sections of tubing that make up the main reactor body.

7.3.4 Downstream Quench Section

The remainder of the fluid from the reactor exits through a port in the bottom of the outlet block and is immediately cooled with ambient water. A short shell-and-tube heat exchanger on the outlet tube cools the product stream to stop any reaction. Following the short heat exchanger is an 18 x 12 x 15 in. (46 x 30 x 38 cm) rectangular, aluminum tank full of cooling water that further cools the product stream. The product stream passes through approximately 30 ft. (9.1 m) of loosely coiled Inconel 625 tubing. Cooling water is fed to the tank through a port near the bottom, and excess water exits through 3 bulkhead fittings connected to flexible rubber tubing and out to the floor drain.

The temperature of the cooled product stream is measured by a type-K thermocouple inserted in the flow path and the pressure is measured with a Dynisco pressure transducer (p/n G8320005M) with a digital readout (p/n 1290). Pressure through the system is controlled by a back-pressure regulator (Go p/n BP66-1A110*0154 with a custom valve coefficient, $C_v = 0.01$) and adjusted manually by the operator. Effluent from the back-pressure regulator (BPR) may be separated into gas and liquid phases and analyzed or simply collected as waste (since the composition measurements are performed with the sampling probe).

7.3.5 Safety Barrier

The entire apparatus is contained in a 4-walled room for safety purposes. The room consists of two concrete walls (from the building) and two walls erected primarily with Lexan and aluminum. The probe side faces one of the concrete walls, as it was the biggest uncertainty upon initiation of the reactor system. The wall at the inlet end of the reactor consists of two large aluminum sheets (3/16 in. (0.48 cm) thick) upon which are mounted many of the measurement readings and control devices. The remainder of the wall is 3/4 in. (1.9 cm) Lexan and includes a door to access the pumps. The remaining wall is constructed of two large Lexan sheets mounted on wheels that slide open — to allow access to the entire reactor — and closed, when the reactor is under pressure.

7.4 Reactor Operation

To start the reactor after it has been disassembled, the system must be filled with water before pressurizing. This is accomplished by removing the top window port and filling the main reactor with distilled, deionized, degassed 18.0 MΩ water until the level reaches the window seat. The reactor is then sealed tight and the pumps can be initiated. Once the flow is steady through the system, the back-pressure regulator is tightened to increase the pressure. This is done slowly for the first several hundred psi, and then more rapidly once a pressure of approximately 300 psig is established. The pressure is increased to 3300 psig, where it is held during the heatup stage. This pressure is slightly smaller than the typical operating pressure of 3550 psig to allow for the expansion of the fluid as it is heated through the critical temperature. Pressure and temperature measurements and controllers are located on a panel shown in Figure 7.4.

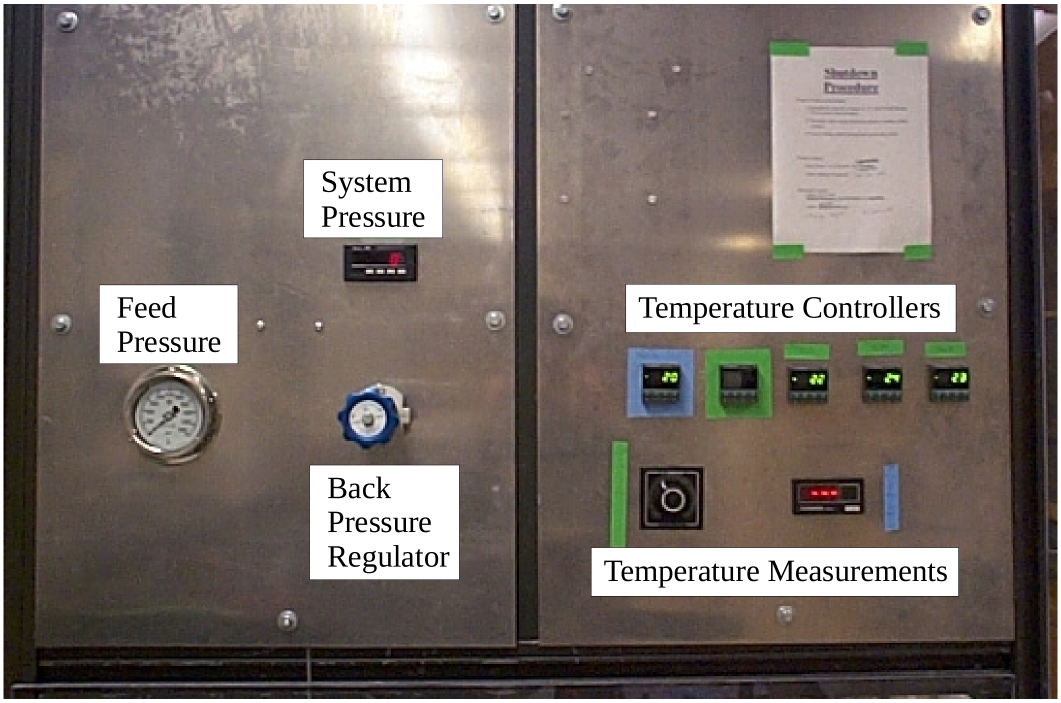

Figure 7.4: Temperature and pressure control panel for large tubular reactor

The cooling water for the main seal heat exchanger and the ‘quench’ tank are begun and heatup is initiated. To heat the reactor and the preheaters, the setpoints of the temperature controllers are increased in increments of 50 to 100ºC, and the reactor is allowed to reach the setpoints before further heating. This avoids integral windup of the controllers due to the slow temperature increase caused by the large thermal mass. During heatup, the fluid temperatures measured by the 3 thermocouples in the main reactor are significantly less than the wall temperatures, which are regulated by the heaters. Even when the final desired temperature is reached, the fluid temperature is less than the wall temperatures. This may indicate that heat is lost between the preheaters and the inlet, and the wall heaters cannot compensate for the heat loss.

Once the reactor is at the desired temperature and pressure, the position of the sample probe and the flow rate through the sample line can be set. To move the sample probe, the power switch on the hydraulic pump control panel must first be turned on. The 3-way switch then controls the movements of the probe. The probe moves forward slowly when the reactor is at high pressure, but care must be taken not to over-pressurize while moving the probe forward. Retracting the probe is more difficult, because the high pressure causes it to move very quickly, resulting in large pressure drops. Therefore, ideal operation would involve beginning with the probe in the desired position that is furthest from the inlet and slowly moving it forward to the other desired positions throughout the day. Before the valve is opened to allow flow through the sample line, a steady flow of cooling water should be established through the probe. The flow rate through the sample line is adjusted manually using the micro-metering valve.

The organic flow can then be initiated and the pressure adjusted to the desired value with the back-pressure regulator. The system should be allowed to equilibrate for at least one hour. After the system reaches steady-state, samples may be taken and analyzed for composition of the effluent. Once measurements are complete at a particular residence time, the probe can be moved forward to measure another residence time. The system will need some time to equilibrate after the disruption to flow and pressure, but it should be significantly less than one hour.

At the end of all measurements, the preheaters and reactor heaters can be turned off. The flow and high-pressure should be maintained through the system during the initial stages of cool-down to avoid the rapid boiling of the contents of the reactor. Once the system is at a temperature less than 100ºC, the pressure can be reduced and the pumps turned off.

7.5 Preliminary Testing

To date, test runs have been performed with deionized water to test the capabilities of the system. The reactor system was tested up to temperatures of 600ºC at a pressure of 250 bar. The probe was moved forward slowly (~0.1 cm/s) with modest pressure deflections observed. However, retracting the probe caused a rapid drop in pressure, since the probe moved fairly quickly (~3 cm/s).

During operation of the sampling probe, some scratches developed along the length of the probe. The probe was removed and repolished by Harwood Engineering in an attempt to remedy the problem. Upon reinsertion of the probe, the scratching persisted but did not have any effect on the probe’s ability to make a high-pressure seal. After further attempts to remedy the scratching, it was decided that nothing could be done.

Since the scratches did not affect the ability to seal, this should not pose a significant problem in the future.

The primary problem with the reactor is the seal between the large reactor tube and the window assembly block. Once the seal is made, the system may be cycled many times without problems. However, making the initial seal is not straightforward and is not predictable. Attempts were made using two adjacent c-seals to increase the amount the seals are compressed. This was successful for some time, but is not working at the moment. Currently, no immediate solution is available and further work on making this large diameter seal is necessary.

7.6 References

DiNaro, J. L., J. W. Tester, K. C. Swallow, and J. B. Howard (2000). "Experimental measurements of benzene oxidation in supercritical water." *AIChE Journal* **46** (11): 2274.

DiPippo, M. M. (1998). "Phase behavior of inorganic salts in sub- and supercritical water." Ph.D. Thesis, Department of Chemical Engineering, MIT. Cambridge, MA.

Helling, R. K., and J. W. Tester (1987). "Oxidation kinetics of carbon monoxide in supercritical water." *Energy & Fuels* **1**: 417.

Lieball, K., K. A. Smith, W. A. Peters, B. Wellig, P. R. Von Rohr, and J. W. Tester (2001). "Design of operating conditions for a transpiring wall reactor for supercritical water oxidation." In process.

Peters, W. A. (2000) Personal Communication.

Webley, P. A., J. W. Tester, and H. R. Holgate (1991). "Oxidation kinetics of ammonia and ammonia-methanol mixtures in supercritical water in the temperature range 530-700 °C at 246 bar." *Industrial & Engineering Chemistry Research* **30**: 1745.

Chapter 8

In Situ Raman Spectroscopy in Supercritical Fluids

One of the primary limitations of analytical techniques used in the supercritical fluids laboratory is the inability to measure composition without first reducing the temperature and the pressure to ambient values. Because of this limitation, some species that are stable under supercritical conditions but unstable at ambient conditions cannot be measured. As a result, some reaction pathways are incomplete or may include species that have not been observed experimentally.

On a more fundamental level, there is currently no good model for reaction dynamics in supercritical fluids. Since a supercritical fluid is neither a gas nor a liquid, the kinetic models that are established for these phases are not directly applicable. Therefore, tools that probe molecular-level processes are essential to developing a proper fundamental understanding of reactions in supercritical fluids.

One solution to these problems is the development of Raman spectroscopy for measurements in supercritical fluid reactors. The applicability of Raman spectroscopy to detect intermediate species in SCWO has been demonstrated elsewhere (for example, see Croiset and Rice, 1998). Additionally, *in situ* spectroscopic tools can be used probe reactions and solvation processes at a molecular level. In this chapter, preliminary results of measurements using *in situ* Raman spectroscopy are discussed.

The Raman spectroscopy apparatus, donated by the Asahi Chemical Company (See Section 8.2.1), was assembled and the initial measurements were conducted with the help of Arturo Casielles, Markus Haider, and Pankaj Bhatia (all from Professor Steinfeld's group). Because the sample compartment in the current configuration of the Raman apparatus has temperature limitations, all measurements were conducted in supercritical carbon dioxide (SCCO$_2$) rather than SCW. It is hoped that insight gained from these experiments will aid in the implementation of Raman spectroscopy for identification and characterization of specific chemical species in supercritical water oxidation systems. In addition, we plan to use Raman methods in synthetic chemistry experiments underway in SCCO$_2$/H$_2$O mixtures.

The focus of these experiments was to determine how vibrational frequencies change as temperature, pressure, and density are varied under supercritical conditions. An understanding of vibrational changes with respect to changes in these physical properties is necessary in order to measure species composition quantitatively for conditions of interest. Furthermore, several investigators have suggested that local density enhancements (or "clustering") occur in SCCO$_2$ systems, especially near the critical point (Tucker, 1999). *In situ* Raman spectroscopy provides molecular information about the vibrations and can be used to probe local solvation effects.

8.1 Introduction to Raman Spectroscopy

Raman spectroscopy is a method of probing the molecular vibrations of species by analyzing the scattering of light incident on a sample. At a specific wavelength, molecules interact with incident photons. If the photon energy corresponds to an eigenstate of the vibrational Hamiltonian, the photon may be absorbed, producing an excited state. At non-resonant frequencies, the light is instantly re-emitted. This re-emission of the photon is the light scattering process.

Light may be scattered either elastically or inelastically, as shown in Figure 8.1. Elastic, or Rayleigh, scattering occurs when the photon is re-emitted at the same frequency as the incident photon. This leaves the molecule in its initial electronic and vibrational state. A small fraction of re-emitted light is shifted away from its incident frequency by Raman (or inelastic) scattering. When Raman scattering occurs, the molecule ends up in a different vibrational state (either higher or lower). If the molecular vibrational state is at higher energy than the initial state, the photon emitted has a lower energy than the incident photon (longer wavelength); this is called Stokes' scattering. Similarly, a transition to a lower-energy vibrational state results in a photon with higher energy than the incident photon; this is called anti-Stokes' scattering. Due to the higher population of the lower vibrational states, anti-Stokes' scattering is typically much less intense than Stokes' scattering. For our conditions and measurements, only Stokes' scattering will be considered.

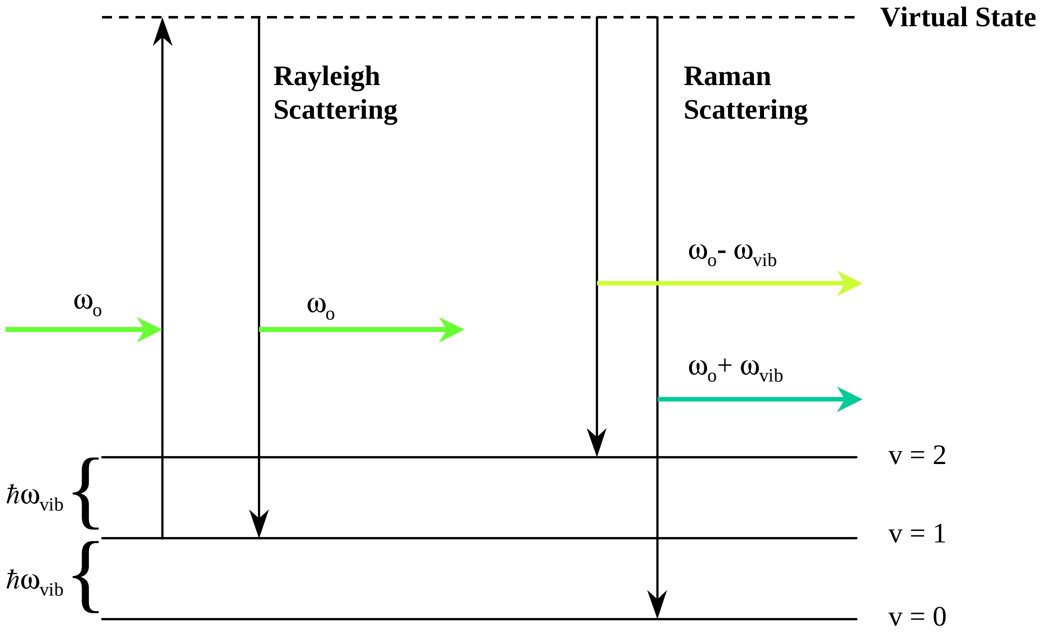

Figure 8.1: Energy level diagram showing Rayleigh and Raman scattering.

8.1.1 Theory

The Raman effect may be derived readily from a classical-mechanical model. For a monochromatic laser operating at a particular frequency, ω_o, the fluctuating electric field at a given point in the path of the laser can be expressed as:

$$E = E_0 \cos(\omega_0 t) \tag{8.1}$$

where E_o is the amplitude of the electric field fluctuation. As the light wave interacts with electrons in a molecule, the fluctuating electric field induces a dipole moment:

$$\mu_{ind} = \alpha E = \alpha E_0 \cos(\omega_0 t) \tag{8.2}$$

where α is the molecular polarizability.

If the molecule possesses a specific vibration of frequency ω_{vib}, we can define the vibrational normal coordinate, q, as:

$$q = q_0 \cos(\omega_{vib} t) \tag{8.3}$$

We can expand the polarizability as a Taylor series in normal coordinates of vibration, evaluated at equilibrium:

$$\alpha = \alpha_0 + \left[\frac{\partial \alpha}{\partial q}\right]_0 q + \frac{1}{2}\left[\frac{\partial^2 \alpha}{\partial q^2}\right]_0 q^2 + \ldots \tag{8.4}$$

Ignoring second order and higher terms of q, the dipole induced by an incident laser can be expressed as:

$$\mu_{ind} = \alpha_0 E_0 \cos(\omega_0 t) + \left[\frac{\partial \alpha}{\partial q}\right]_0 q_0 E_0 \cos(\omega_0 t)\cos(\omega_{vib} t) \tag{8.5}$$

By trigonometry:

$$\cos(A)\cos(B) = \frac{1}{2}\left[\cos(A+B) + \cos(A-B)\right] \tag{8.6}$$

And so we can rewrite Eqn. 8.5 as:

$$\mu_{ind} = \alpha_0 E_0 \cos(\omega_0 t) + \left[\frac{\partial\alpha}{\partial q}\right]_0 q_0 E_0 \frac{1}{2}\left[\cos[(\omega_0 + \omega_{vib})t] + \cos[(\omega_0 - \omega_{vib})t]\right] \quad (8.7)$$

From this derivation, we can see that the resonant frequencies of the polarizability have a Rayleigh contribution, ω_o, and Raman contributions, (ω_o+ω_{vib}) and (ω_o-ω_{vib}). Furthermore, one can see that Rayleigh scattering is proportional to the polarizability of the molecule at equilibrium, α_o. Therefore, any particle that has an electron cloud, and hence polarizability, will scatter light via the Rayleigh effect, whereas Raman scattering depends on the change of the polarizability, $[d\alpha /dq]_o$, caused by the vibration. Therefore, vibrations that change the polarizability of a molecule are referred to as “Raman active”. The vibrational modes that are the most Raman active are symmetric stretches, because they distort the size of the molecule's electron cloud.

In Raman spectroscopy, scattered light is collected and dispersed by a monochromator. The incident light is filtered out, and a detector measures the intensity of the remaining light as a function of its wavelength. Measurements are typically reported as the amount the light has been “shifted” from its incident frequency. Correlating the Raman shifts to known vibrational frequencies of molecules allows for species identification. Calibrating of the integrated area of a vibrational band to an internal standard can then be used to quantify compositions.

An important feature of the Raman effect is that it can occur for any frequency of incident light (although the scattering amplitude varies with incident wavelength). Other spectroscopic techniques, such as IR or UV/vis, are limited by the requirement that the solvent and windows do not absorb in certain regions of the spectrum. In Raman spectroscopy, however, one can choose a laser such that the solvent and windows do not interfere with the measurement.

8.1.2 Application to Solutes in Supercritical Fluids

When a molecule is in the gas phase, collisions may be neglected in first order, and therefore, its vibrational frequencies are approximately the same as if the same molecule were in a vacuum. However, when a molecule is dissolved in a solvent, the solvent interacts strongly with the molecule, resulting in a perturbation of the electronic structure. This change in electronic structure affects the vibrational frequencies and can be observed in the measured spectrum.

The type of interactions between the solvent and the solute determines the degree to which the vibrational spectrum is perturbed. For example, a solvent that forms hydrogen bonds with a solute will have a much greater influence than a solute that interacts only via induced dipole-induced dipole dispersion forces. Therefore, vibrational spectroscopy can be used to probe the nature of solvation interactions between a solute and its surrounding solvent molecules.

Supercritical fluids are typically described as dense gases. Near the critical point, however, several authors have observed large negative partial molar volumes of solutes, which they have attributed to strong solvent-solute interactions (Kim and Johnston, 1987; Kauffman, 1996). These strong attractive interactions lead to enhanced local densities solvent molecules, sometimes approaching liquid-like densities, around the solute. This local density enhancement, or solvent clustering, could have significant effects on solubilities, reaction pathways, and phenomena such as crystallization. Therefore, it is important to measure the degree of clustering that occurs in solutions near the critical point and to determine the effects this may have on the thermodynamic and kinetic properties of the solution. Raman spectroscopy can be used to probe the local solvent environment around a dissolved species and is, therefore, an effective tool for elucidating this clustering phenomenon.

8.2 Experimental Setup and Measurements

8.2.1 Raman Apparatus

The Asahi Chemical Company donated the Raman apparatus (JASCO model NR-1000) that was used in these experiments. The Raman unit consisted of a laser, a sample chamber, collection optics, a spectrometer, a detector, and a control/data collection station. The source of excitation light was a water-cooled 8 W (total output for all lines) Ar^+ laser with wavelength selection of 514.5 nm monochromatic light. The maximum power output at 514.5 nm was 2 W, but only 200 mW was used for these experiments. The laser beam was directed into the sample chamber where it was focused vertically (upward) into the center of the sample. A concave mirror above the sample reflected the light down through the sample a second time. A schematic of the Raman apparatus interfaced with the $SCCO_2$ system is shown in Figure 8.2.

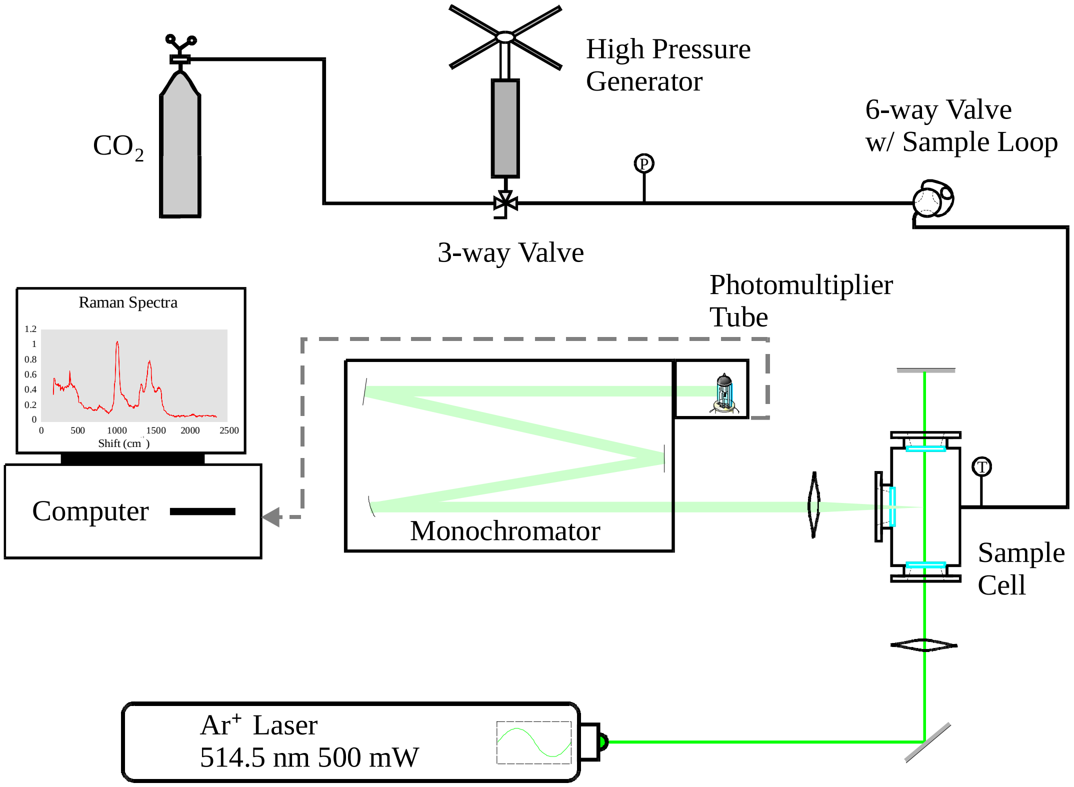

Figure 8.2: Schematic of Raman apparatus interfaced with SCCO$_2$ sample cell. (See Figure 8.3 for details of sample cell.)

Scattered light was collected at a right angle from the incident radiation with a collimator and then focused onto a slit (1.0 mm) where the light entered the spectrometer. Diffraction gratings separated the light by its wavelength in the triple pass spectrometer. The separated light was measured through an exit slit (1.0 mm) using a photomultiplier tube (PMT) with a scanning speed of 1 cm^{-1}/s. With these settings, the measured resolution of the system (using a HeNe laser) was approximately 6 cm^{-1}. The signal from the PMT was measured and stored in the control station, from where it could be exported to a personal computer (PC). For all measurements, the signals from 8 scans over the frequency range were averaged to minimize interference by noise. Bhatia (1998) describes in detail the interface between the control station and the PC.

8.2.2 Supercritical Carbon Dioxide System

A small, high-temperature, high-pressure cell was designed and built for measurement of species dissolved in $SCCO_2$. The cell was machined from a stainless steel (316) rod according the drawing shown in Figure 8.3.

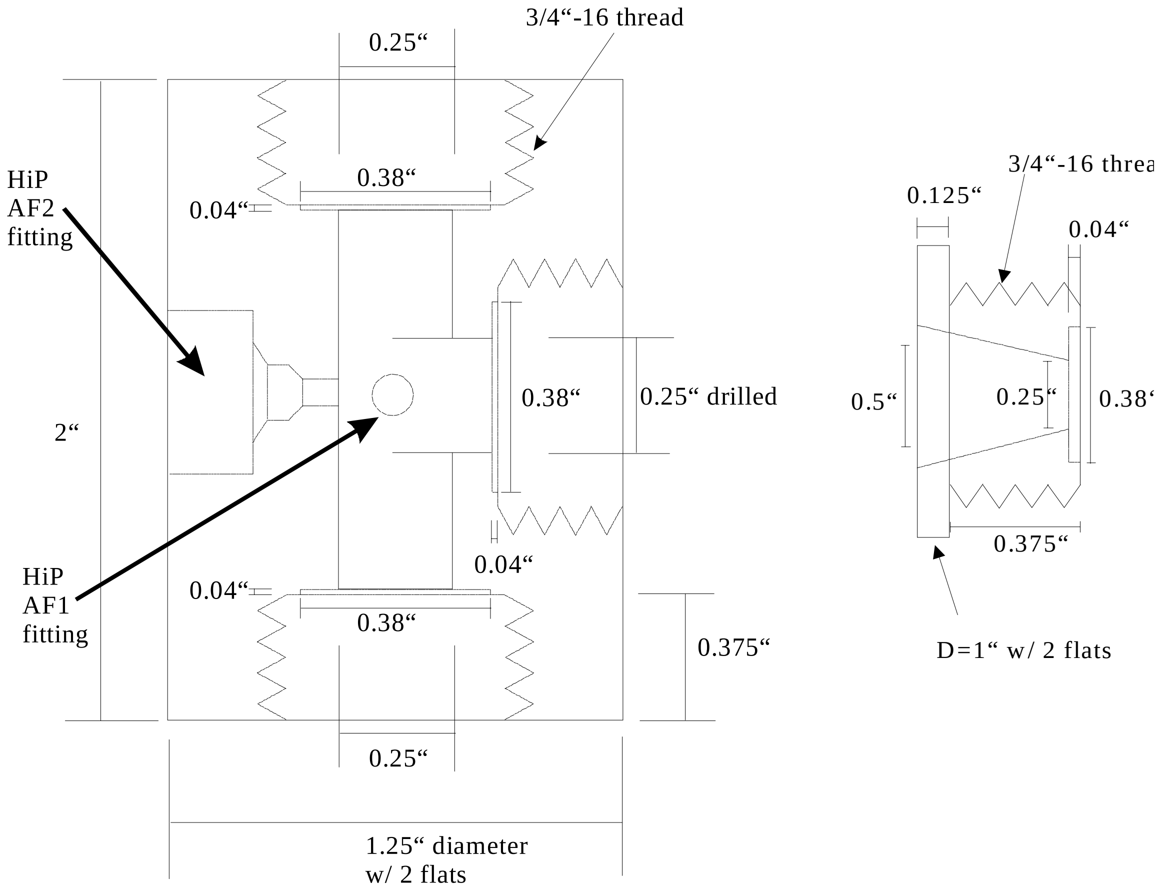

Figure 8.3: Machinist's drawing of the $SCCO_2$ sample cell and glands.

The assembled cell has 3 sapphire windows (3/8 in. (9.5 mm) O.D. x 1/8 in. (3.2 mm) thick) held in place by 3 SS-316 glands with hand-cut poly(tetrafluoroethylene) (PTFE) gaskets to make the seal. Alternatively, copper foil gaskets have been tested and could be used if higher temperatures were desired. The windows are located on the bottom and top — where the laser beam enters and exits — and on one side perpendicular to the beam path, where the scattered light is collected. One port that accepts 1/8 in.

(3.2 mm) High Pressure Equipment (HiP) taper seal fittings (AM2) and one port that accepts 1/16 in. (1.6 mm) HiP AM1 fittings are machined into the cell. Through these two ports, temperature can be measured and fluids may be pumped into or out of the cell.

Temperature was measured with a 1/32 in. (0.8 mm) type-T thermocouple inserted to the inner wall of the cell. In order to avoid direct reflection of the laser, the thermocouple was not inserted into the middle of the cell. The temperature of the cell was controlled with an Omega CN9000A PID controller. The output of the controller ranged from 4 to 20 mA and triggered a solid state relay (Omega p/n SSR240DC45). When triggered, the relay delivered 0 to 104 W (manually controlled by the operator with a Variac®) of power to a flexible tape heater (Omega p/n FGS051-020).

Liquid carbon dioxide (99.8% pure, “bone dry”) with a dip tube was connected through a 3-way valve to a high-pressure generator (HiP p/n 50-6-15). With the 3-way valve pointed toward the cylinder, liquid CO_2 was drawn into the chamber of the pressure generator by manually withdrawing the piston with its hand crank. The 3-way valve was then switched to connect the pressure generator to the sample cell, and the contents were manually pumped into the main cell. The pressure was measured with a Dynisco pressure transducer (p/n G832-000-7.5M) that was connected between the pressure generator and the sample cell.

Solutes were introduced into the reactor using a 6-way valve (Valco p/n C6UW) connected in the CO_2 line. Using a glass syringe, a 25 μL sample loop was filled with the desired solute (benzene or methylene chloride) with the 6-way valve in the “load” position. The 6-way valve was switched to the “inject” position, and CO_2 was used to displace the organic from the sample loop and into the cell.

8.2.3 Experimental Measurements

Three sets of experiments were conducted in this study: 1) Pure CO_2; 2) Benzene dissolved in CO_2; and 3) Methylene chloride dissolved in CO_2. For each set of experiments, spectra were measured at 80ºC with pressures ranging from 30 to 136 bar (series 1). Then, holding the pressure constant at 136 bar, spectra were measured at 80, 50, and 31.1ºC (series 2). Finally, spectra were measured at 31.1ºC with pressures ranging from 30 to 136 bar (series 3). These 3 series of measurements are displayed as arrows on the phase diagram of pure CO_2 in Figure 8.4 to show where these conditions lie relative to the critical point (T_c = 31.1ºC, P_c = 73.8 bar).

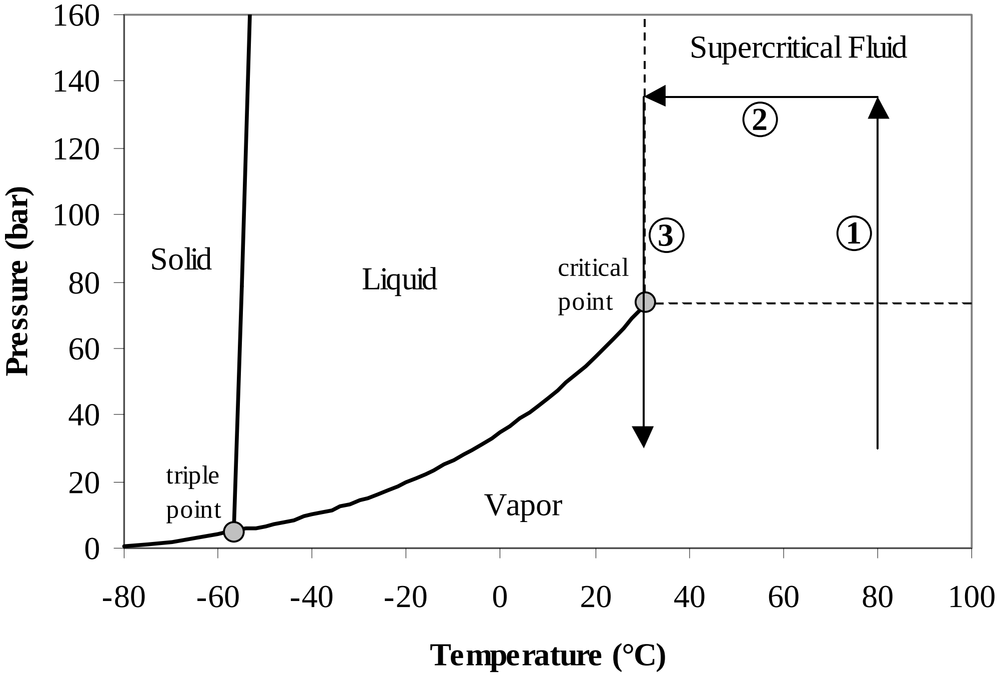

Figure 8.4: Phase diagram of CO_2 showing the range of experimental temperatures and pressures. Each arrow represents a series of conditions studied.

8.3 Results and Discussion

8.3.1 Pure CO_2

As a baseline for understanding the intermolecular interactions in supercritical fluids, the effects of temperature and pressure (and density) on the vibrations of pure $SCCO_2$ were measured. The focus of this part of the study was to measure changes in the symmetric stretch of CO_2, which has a fundamental frequency of 1333 cm^{-1}. However, due to Fermi resonance with the second harmonic of the CO_2 bending vibration ($\omega = 667$ cm^{-1}), the symmetric stretch is split into a Fermi dyad with vibrational bands measured at 1285 and 1388 cm^{-1} (Shimanouchi, 1972).

In this set of experiments, spectra were measured from 1250 to 1420 cm^{-1} at 7 different sets of conditions to cover a range from sub- to supercritical. The temperatures ranged from 31.1 to 80ºC and the pressures ranged from 33.3 to 136 bar. The resulting spectra are shown in Figure 8.5, according to the 3 series of measurements described previously. To allow comparison, the spectra are scaled so that all vibrational bands are comparable in size (Figure 8.5). The lines on each plot are drawn at the gas-phase values from the literature.

The complete assigned Raman spectra for CO_2 is listed in Table 8.1. As expected, the measured spectra show two large peaks in this region. One peak is measured at 1282-1287 cm^{-1} and the other is measured at 1385-1390 cm^{-1}. The two peaks are approximately the same size at 80ºC, but the high-frequency peak becomes larger than the low-frequency peak as the temperature is decreased. Furthermore, two small peaks at approximately 1264 and 1409 cm^{-1} are observed, primarily at high pressure. The relative size of these two peaks increased with temperature because they correspond to ‘hot-bands'. These 'hot-bands' result from Raman scattering from the thermally populated $v_2 = 1$ level. The Fermi interaction increases for higher vibrational levels of the bending mode resulting in a larger splitting for the hot band transitions. Because the population of the $v_2 = 1$ level increases with temperature, the relative size of these 'hot bands' also increases with temperature.

Table 8.1: Assignment of Raman spectra of CO_2 (Herzberg, 1945).

Frequency (cm^{-1})	**Upper State**[a] v_1 v_2^l v_3	**Lower State**[a] v_1 v_2^l v_3	**Relative Intensity**
1285.5	0 2^0 0	0 0^0 0	Very strong
1388.3	1 0^0 0	0 1^0 0	Very strong
1264.8	0 3^1 0	0 1^1 0	Medium
1409.0	1 1^1 0	0 1^1 0	Medium
1242	0 4^2 0	0 2^2 0	Weak
1305.1	0 4^2 0	0 2^0 0	Very weak
1325.0	?	?	Very weak
1344.1	1 2^0 0	0 2^2 0	Very weak
1369.4	1 2^2 0	1 0^0 0	Very weak
1430	1 2^2 0	0 2^2 0	Weak
1528	2 0^0 0	0 2^0 0	Weak

[a] Upper and lower states are listed according to values of vibrational quantum numbers (v_i) for the 3 fundamental modes and l represents the angular momentum quantum number.

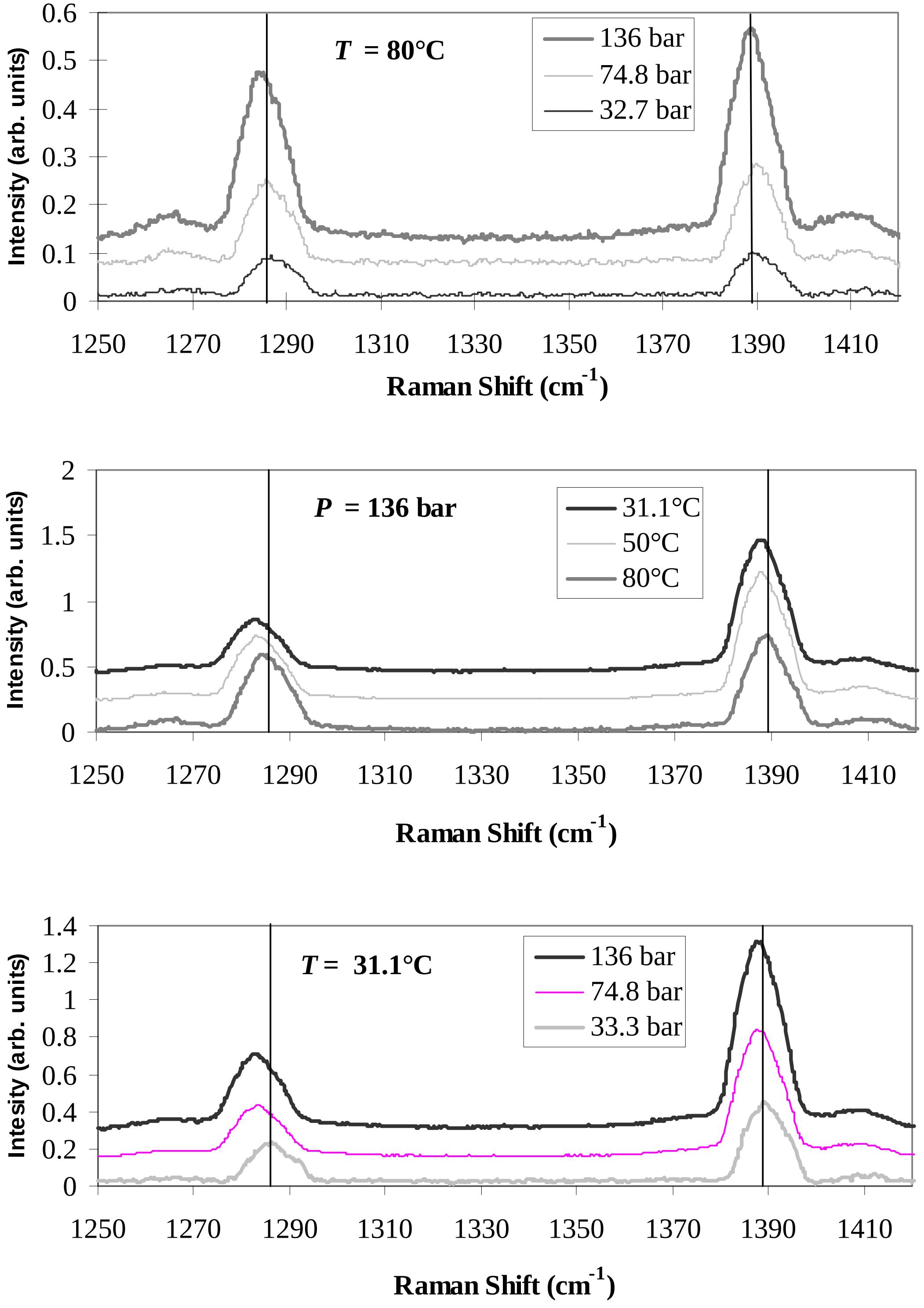

Figure 8.5: Measured spectra of pure CO_2 as functions of temperature and pressure.

By comparing the peak locations, one can see that the vibrations shifted to a slightly lower frequency as the pressure was increased at constant temperature. The spectra also shifted to lower frequency as the temperature was decreased at constant pressure. Both of these observations are in agreement with the fact that higher densities result in larger intermolecular interactions. In this case, the interactions stabilize the vibration and caused it to be red-shifted. Figure 8.6 shows how the peak location of the low-frequency band varied as a function of density. (Note: peak locations were approximated by eye and no spectral analysis software was employed.) It is clear from this plot that the shift is primarily a function of density. For similar values of density, the peak location is approximately the same, regardless of temperature. Furthermore, the shape of the curve matches what would be predicted qualitatively. The curve is linear at low density due to increased collisions, and begins to level off at high density as the fluid becomes a liquid, continuously interacting with adjacent molecules.

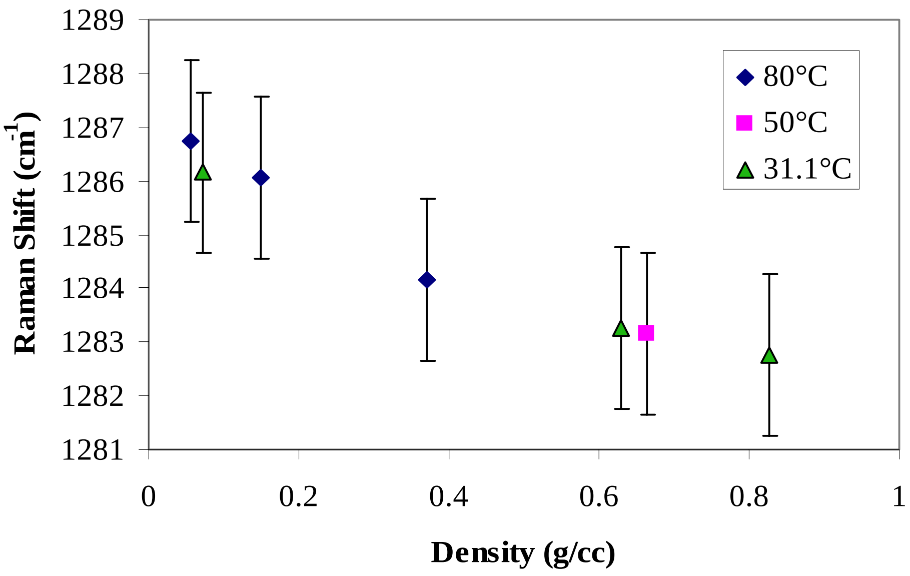

Figure 8.6: Peak location as a function of density for 1285 cm^{-1} band of pure CO_2. Error bars were set to ± 1.5 cm^{-1}.

8.3.2 Benzene in CO_2

In the second set of experiments, the effects of CO_2 density on the vibrations of benzene were measured. Many of the vibrational modes of benzene are Raman active, but the two strongest modes are shown pictorially in Figure 8.7. The first mode is the totally symmetric C_6 ring stretch (also called the ring-breathing mode), which has a fundamental frequency for pure benzene of 993.1 cm^{-1} in the gas phase and 991.6 cm^{-1} in the liquid phase (Shimanouchi, 1972). The second vibration studied was the totally symmetric C-H stretch, with a gas-phase frequency of 3073.9 cm^{-1} and a liquid-phase value of 3062 cm^{-1} (for pure benzene) (Shimanouchi, 1972). Both of these vibrational modes had Raman cross-sections much greater than CO_2, which allowed for measurements at low molar concentrations. For example, a spectrum measured at 80ºC and 74.8 bar from 950 to 1450 cm^{-1} (Figure 8.8) shows the size of the ring-breathing band of benzene relative to the CO_2 bands at just 5 mol%. The benzene band is at least 50% the size of each CO_2 band, representing a Raman cross-section that is at least 10 times as big.

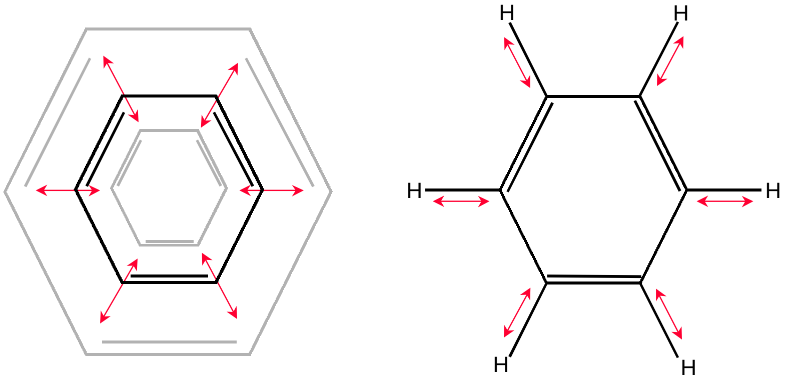

Ring Breathe (ω_2) Symmetric C-H Stretch (ω_1)

Figure 8.7: Strongest Raman-active vibrational bands of benzene.

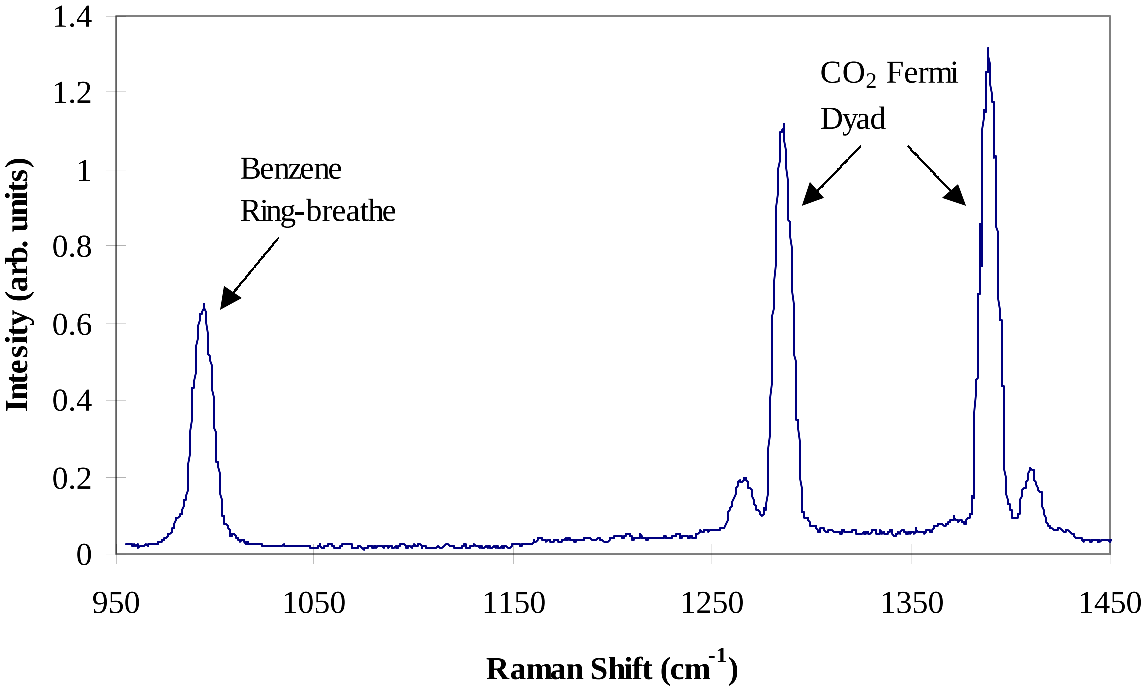

Figure 8.8: Spectra of 5 mol% benzene in CO_2 (to show comparison of band sizes).

The spectra of the ring-breathing mode of benzene as functions of temperature and pressure are shown in Figure 8.9. Also included for comparison (in Figure 8.9) is a line at the gas-phase value of the vibrational frequency and the measured ambient liquid benzene spectrum. For this particular vibrational mode, the gas-phase and liquid-phase values are not significantly different, which implies that the mode is not very sensitive to intermolecular interactions. Likewise, little effect is seen in the spectra as the density of CO_2 is changed. One can see a slight shift of the spectra to lower frequency as the pressure is increased at constant temperature. As the temperature is decreased at constant pressure, no detectable shift in the vibrational band is observed.

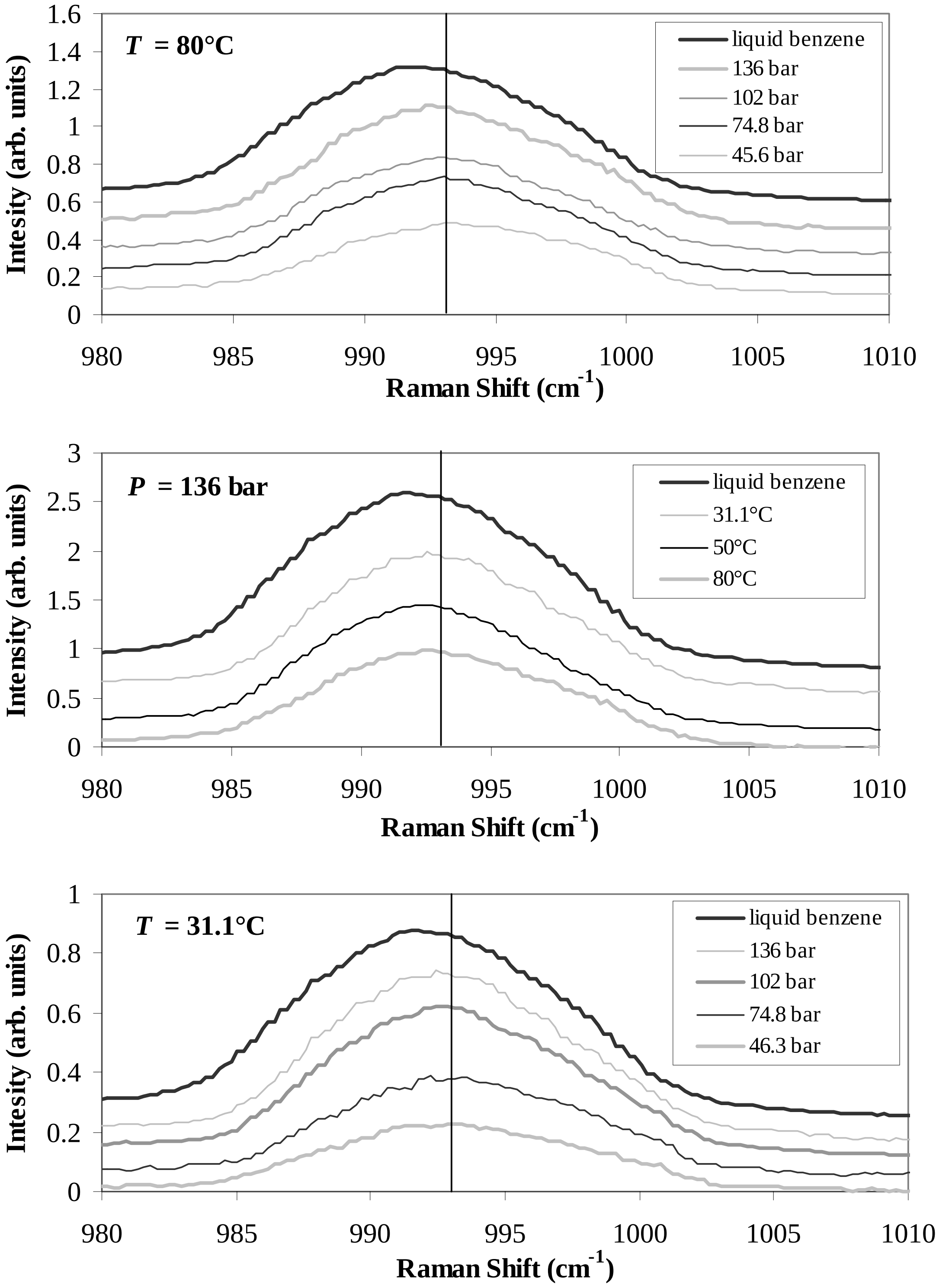

Figure 8.9: Spectra of benzene ring-breathe vibration as a function of CO_2 conditions.

A plot of the measured peak location for the ring-breathing mode at all conditions studied is shown as a function of density in Figure 8.10. Any shift in the peak location is smaller than the uncertainty associated with the measurement, and therefore, no quantitative conclusions can be drawn.

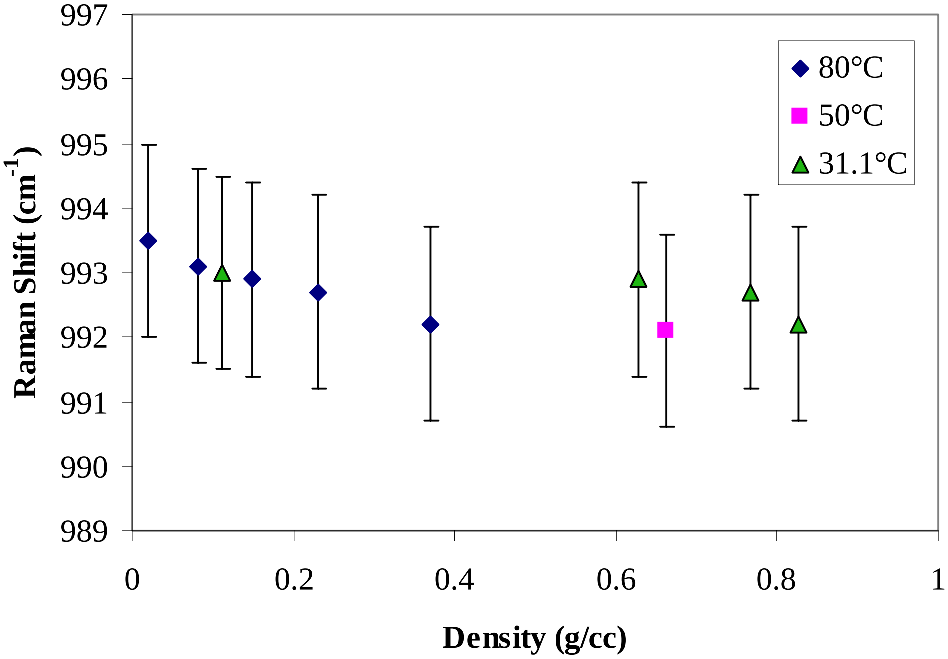

Figure 8.10: Benzene ring-breathe vibrational peak location as a function of CO_2 density. Error bars were set to ± 1.5 cm^{-1}.

A better probe for the local environment around benzene molecules is the symmetric C-H stretch. The liquid-phase frequency (3062 cm^{-1}) for this vibration is almost 14 cm^{-1} less than the gas-phase value (3073.9 cm^{-1}) for pure benzene. Therefore, one might expect that benzene dissolved in high-pressure (liquid-like) CO_2 would have a vibrational frequency that is shifted significantly from its value in low-pressure (gas-like) CO_2, thereby approximating the frequency of liquid benzene. The spectra of benzene dissolved in CO_2 measured at each set of conditions are shown in Figure 8.11, compared with the gas-phase value (line) and the measured ambient liquid benzene spectrum. One can see that, again, the vibrational frequency is red-shifted as the pressure is increased at both 31.1 and 80ºC. However, the vibrations of benzene dissolved in high-pressure CO_2 show a maximum shift of only 3 cm^{-1}. This modest shift does not even begin to approach that seen as pure benzene transitions from a gas to a liquid phase. This indicates that the interactions of CO_2 molecules (at high density) with benzene do not alter the electronic structure nearly as significantly as other benzene molecules, as is observed in liquid benzene.

A plot of the peak location for the symmetric C-H stretch (Figure 8.12) shows that the band shift decreased up to densities of approximately 0.4 g/cc. At higher density, the peak remained fairly constant, possibly indicating that the local density of solvent molecules around a solute reaches its maximum value at moderate densities. Again, the higher frequency vibration measured in CO_2 at 31.1ºC and 74.8 bar (~ 0.6 g/cc) relative to that measured at 50ºC and 136 bar (~ 0.6 g/cc) is not immediately clear. However, it is difficult to make conclusions based on this because of the large size of the uncertainty associated with these peak locations.

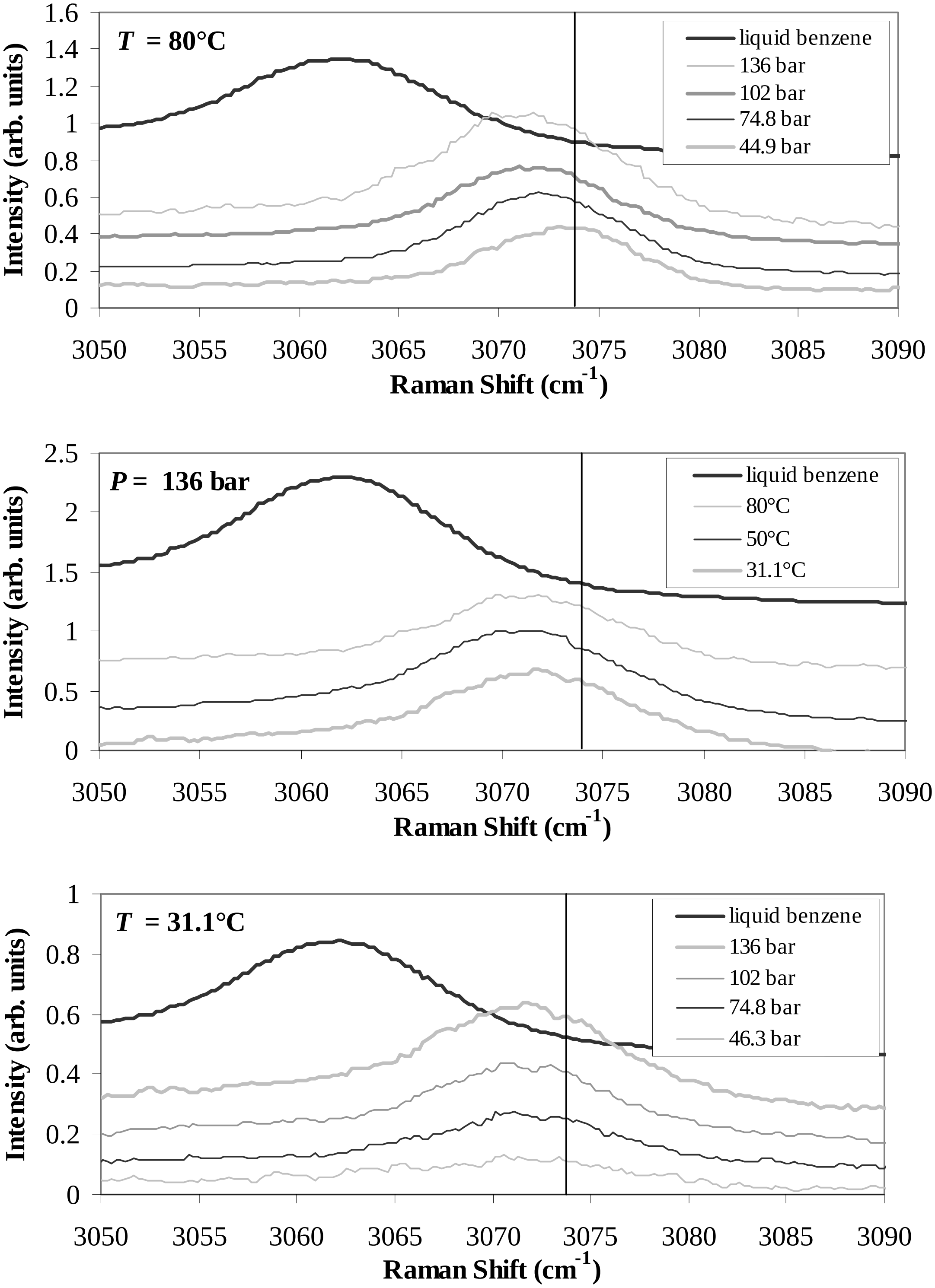

Figure 8.11: Spectra of benzene C-H stretch as a function of CO_2 conditions.

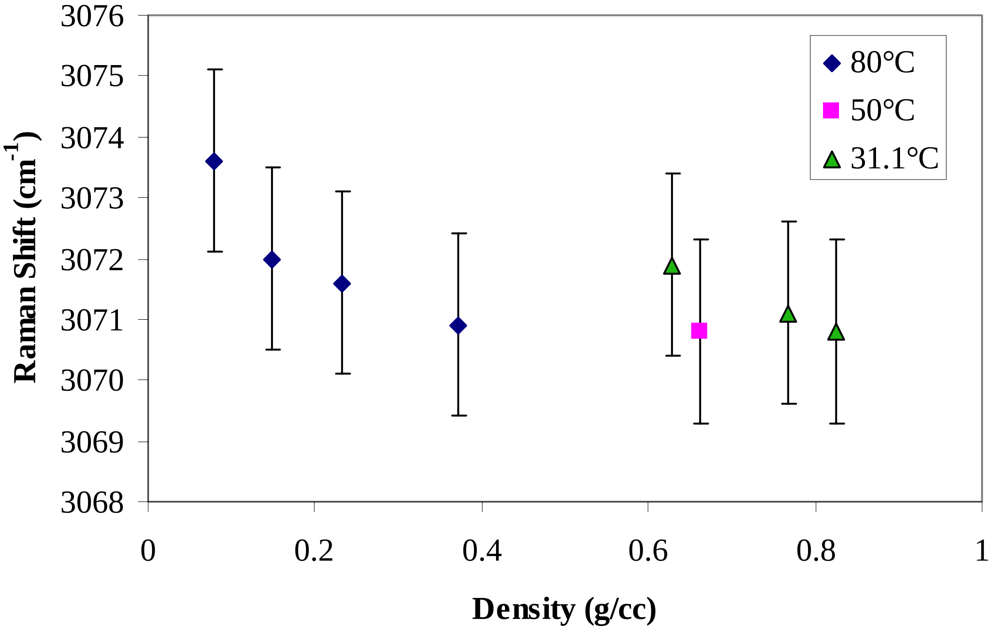

Figure 8.12: Peak location of benzene C-H stretch of benzene as a function of CO_2 density. Error bars were set to ± 1.5 cm^{-1}.

8.3.3 Methylene Chloride in CO_2

In the third set of experiments, the Raman spectrum of methylene chloride was measured as a function of temperature and pressure (and density) of CO_2. Two modes of vibration were chosen as the focus of the study and are shown pictorially in Figure 8.13. The modes correspond to the symmetric $C-H_2$ stretch and the symmetric $C-Cl_2$ stretch. Both modes are Raman active, but the $C-Cl_2$ stretch has a greater Raman scattering cross-section. This is due to the larger change in polarizability caused by the motion of the chlorine atoms, which have big, loosely bound electron clouds.

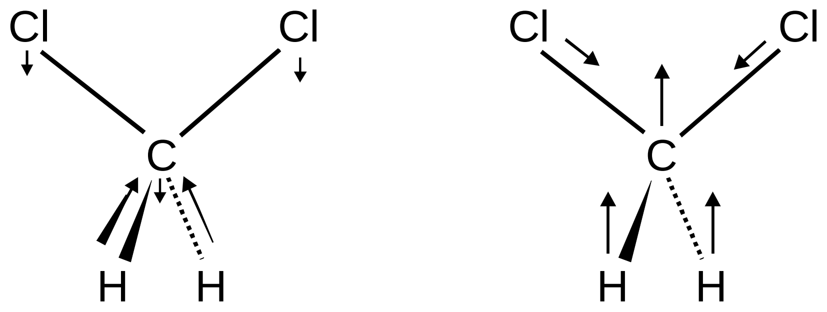

Symmetric C-H_2 Stretch (ν_1) Symmetric C-Cl_2 Stretch (ν_3)

Figure 8.13: Strongest Raman-active modes of methylene chloride

The C-H_2 stretch has a fundamental frequency of 2999 cm^{-1} in the gas phase and shifts to a value of 2984 cm^{-1} in the liquid phase. With this large shift caused by intermolecular solvent-solute interactions, this particular vibrational mode might be a good candidate for local solvation effects in supercritical fluids. Figure 8.14 shows the spectra measured as the conditions of the CO_2 were varied. At first glance, it is clear that the signal-to-noise ratio is significantly smaller for this vibrational band than for those measured previously with benzene. The poorer signal is due to the small Raman scattering cross-section caused by the small change in the overall polarizability. One can also see that no noticeable shift of the peak is observed as the density of CO_2 is increased. This indicates that the interactions between CO_2 and CH_2Cl_2 do not affect the electronic structure such that the C-H_2 stretch is altered in any detectable way.

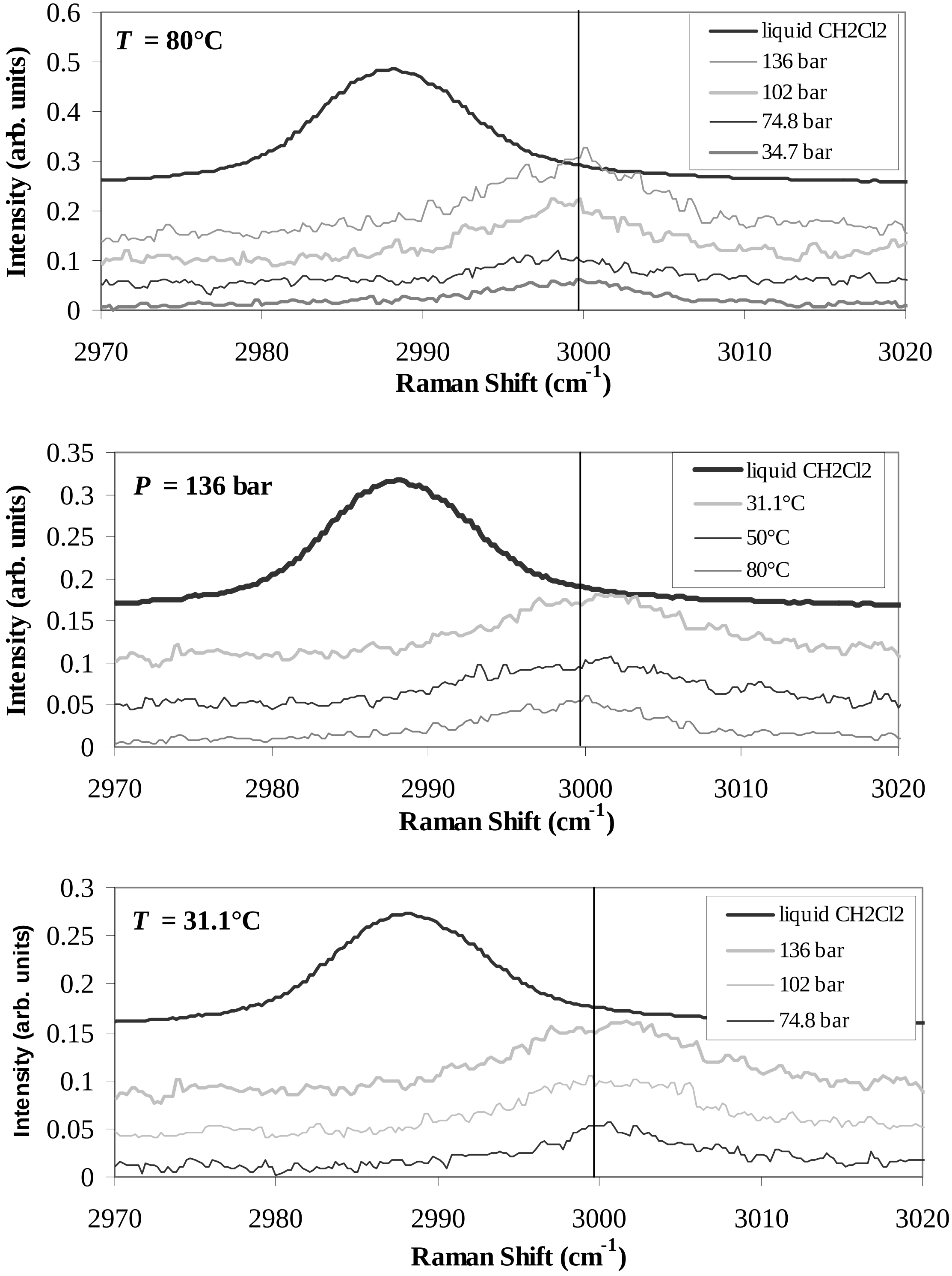

Figure 8.14: Spectra of C-H_2 symmetric stretch of CH_2Cl_2 as a function of CO_2 conditions.

In addition to the study of the C-H_2 stretch, the dependence of the C-Cl_2 stretching band on the density of CO_2 was investigated. The fundamental frequency for the C-Cl_2 stretch is 713 cm^{-1} in the gas-phase and 700 cm^{-1} in the liquid-phase (Shimanouchi, 1972), again indicating that it may be a good probe for intermolecular interactions. The measured spectra of the C-Cl_2 stretch for each set of CO_2 conditions are shown in Figure 8.15. A slight shift in the vibrational band is observed at 80ºC as the pressure is increased. This shift occurs up to approximately 102 bar and then levels out. The band does not shift further as the temperature is decreased or as the pressure is varied at 31.1ºC.

A plot of the C-Cl_2 stretch peak location as a function of CO_2 density is shown in Figure 8.16. Again, one can see a linear region at low density that levels off for densities greater than 0.2 g/cc. This leveling off of the band shift could indicate a local density enhancement around the solute. Alternatively, the leveling off could simply reflect that increasing the density of CO_2 near the solute no longer alters its electronic structure.

The maximum peak shift observed as the density of CO_2 increased from gas-like conditions to liquid-like conditions was approximately 3 cm^{-1}, which is much less than the shift seen from gas-phase to liquid-phase CH_2Cl_2 (approximately 13 cm^{-1}). This indicates that the intermolecular interactions of CO_2 with CH_2Cl_2 do not significantly alter its electronic structure.

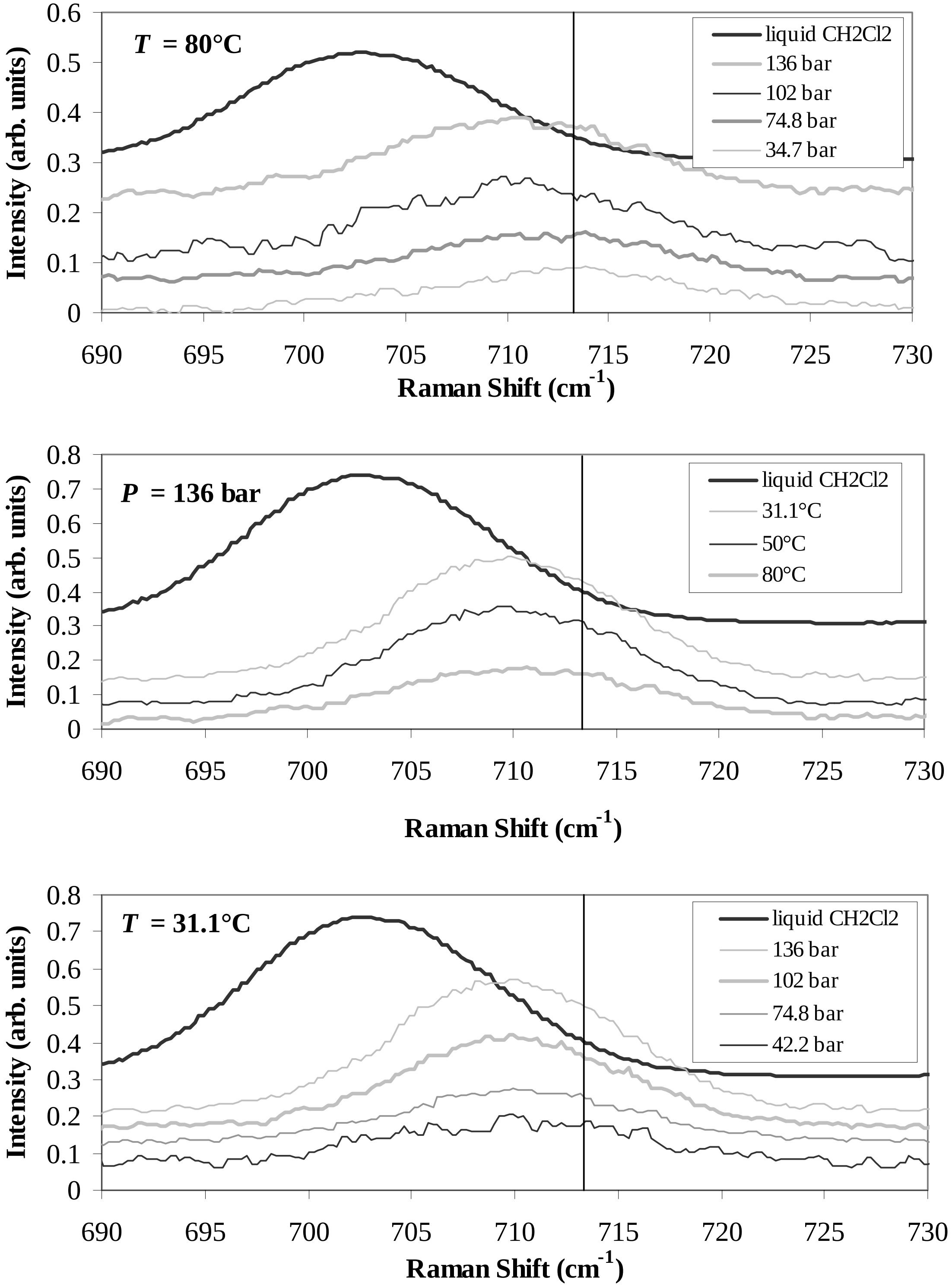

Figure 8.15: Spectra of C-Cl_2 symmetric stretch of CH_2Cl_2 as a function of CO_2 conditions.

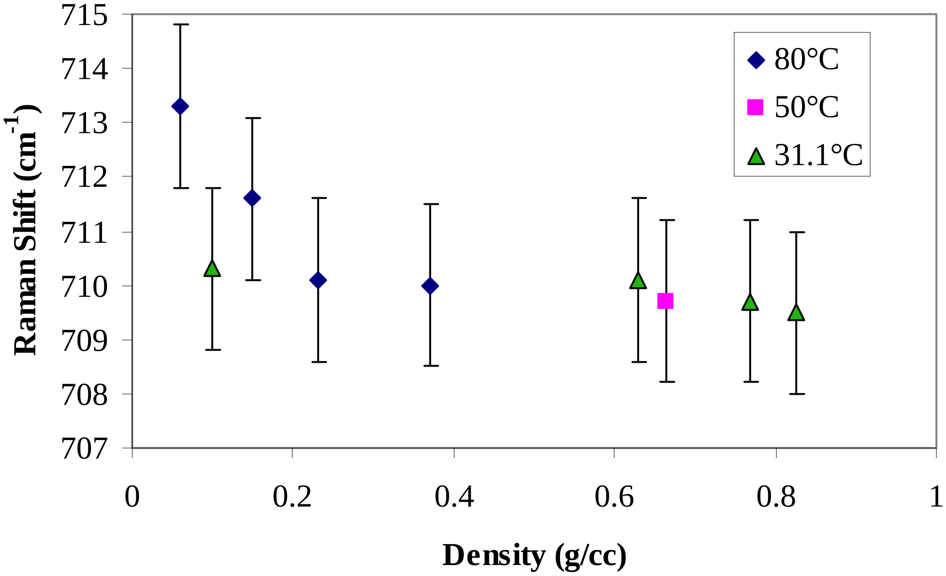

Figure 8.16: Peak location of C-Cl_2 stretch of CH_2Cl_2 as a function of CO_2 density.

8.4 Conclusions

A small cell was designed and built with sapphire windows to allow for Raman measurements of species dissolved in $SCCO_2$. The Fermi dyad of CO_2 (1285 and 1388 cm^{-1}) was measured at temperatures ranging from 31.1 to 80ºC and pressures ranging from 30 to 136 bar. The peaks shifted monotonically to lower frequencies as the density of CO_2 was increased from 0.6 to 0.82 g/cc at temperatures from 31.1 to 80°C. Hot bands were observed at 1264 and 1409 cm^{-1}, and their relative size increased with increasing temperature.

Two vibrational bands of benzene dissolved in CO_2 were measured over the same range of conditions studied for pure CO_2. The vibrational bands of benzene had larger Raman scattering cross-sections than CO_2, allowing for measurement at fairly dilute conditions (<5 mol%). Both peaks showed a shift to lower frequency as the density was increased up to values of approximately 0.4 g/cc. Further increasing the density did not cause further shift in the peaks. This shift was attributed to increased intermolecular interactions between the solute and nearby CO_2 molecules. The maximum shift observed was significantly smaller than the shift seen as benzene is condensed from a gas to a liquid, indicating that CO_2 does not interact as favorably as other benzene molecules do. The data had peculiar trends at 31.1°C, yielding higher frequency vibrations than spectra measured at 50 and 80°C for comparable density.

Two vibrational bands of CH_2Cl_2 were measured in CO_2 as temperature was varied from 31.1 to 80°C and with pressures of 30-136 bar. The scattering cross-section of the symmetric C-H_2 stretch was too small to obtain a good signal-to-noise ratio for the conditions studied. However, it did not appear that the CO_2 density affected the frequency significantly. The C-Cl_2 stretch was measured and showed similar behavior to benzene. The peak shifted to lower frequency as density was increased up to approximately 0.2 g/cc and then remained constant as density was further increased. This could indicate that the local density of CO_2 reaches liquid-like values at moderate densities. However, the maximum observed shift is still significantly smaller than that seen for liquid CH_2Cl_2.

In order to make quantitative conclusions about the local density of CO_2 around solutes, Raman measurement results should be combined with molecular dynamics (MD) simulations. The application of MD could be employed using classical mechanics, but would likely need to be coupled with *ab initio* computational chemistry to allow for rearrangement of the electronic structure, which will affect the vibrational frequencies.

8.5 References

Croiset E. and S. F. Rice (1998). "Direct observation of H_2O_2 during alcohol oxidation by O_2 in supercritical water." *Industrial & Engineering Chemistry Research* **37**(5): 1755.

Herzberg, G. (1945). *Molecular Spectra and Molecular Structure: Volume II*, Krieger Publishing Company, Malabar, FL.

Kauffman, J. F. (1996). "Spectroscopy of solvent clustering." *Analytical Chemistry News & Features* :248 A

Kim, S., and K. P. Johnston (1987). "Clustering in supercritical fluid mixtures." *AIChE Journal* **33** (10): 1603.

Shimanouchi, T., (1972) *Tables of Molecular Vibrational Frequencies Consolidated Volume I*, National Bureau of Standards, Washington, D. C.

Tucker, S. C. (1999). "Solvent density inhomogeneities in supercritical fluids." *Chemical Reviews* **99**: 391.

Chapter 9

Summary and Conclusions

The research presented in this thesis addressed the primary goal of providing a better understanding of reactions that occur in sub- and supercritical water at temperatures from 100 to 600°C and pressures from the vapor pressure to 250 bar. Emphasis was placed on determining the effects of changes in the physical properties of water on reaction rates and mechanistic pathways. Experiments and modeling of methylene chloride hydrolysis demonstrated that water, a reactant in the initial elementary step, also behaved as a dielectric medium that stabilized the transition state. In the study on MTBE, experiments showed that protons, provided by dissociated water, catalyzed the primary reaction pathway.

Additionally, several new experimental and modeling tools were developed that expand the capabilities of the laboratory. *Ab initio* quantum chemistry calculations were performed using *Gaussian 98* to determine a correction for solvent effects on reaction rates. A new reactor system for SCWO was designed and built with optical accessibility and a movable sampling probe. Raman spectroscopy was used to probe interactions between solutes and solvents in supercritical fluids.

The following enumerated list summarizes the specific objectives of this thesis (in italics) and the conclusions reached from each study:

Kinetic Measurements and Analysis of Mechanisms:

1) *Measure the isothermal rate of methylene chloride hydrolysis in sub- and supercritical water.* Experiments at isothermal conditions from 100 to 500°C were completed using two different reactor systems. Quartz ampoule reactors were used for measurements from 100 to 250°C (at the vapor pressure of water). Some of the ampoules contained small amounts of Hastelloy C-276 to determine the catalytic effects of the metal on the reaction rate. A small high-temperature, high-pressure batch reactor was designed and built for isothermal hydrolysis experiments up to 600°C (and 250 bar). The apparatus was designed with a 6-way valve to inject a small sample into the reactor, where it was rapidly mixed and heated to the final reaction temperature.

   The results from quartz ampoule batch experiments clearly showed that (1) surface effects due to Hastelloy C-276 metal on CH_2Cl_2 hydrolysis were negligible, and (2) the Fells and Moelwyn-Hughes (FMH) rate constant correlation (from the literature) predicted slower CH_2Cl_2 hydrolysis kinetics than our experimental results. A new empirical first-order rate expression, obtained using data from 100 to 250°C, was determined and correlated using a standard Arrhenius expression for the rate constant. The empirical rate expression developed in this study yielded predictions of the rate constant faster than those of the FMH correlation up to 150°C.

   At higher temperature, the hydrolysis rate showed a local maximum near the critical point followed by a sharp drop. Above the critical temperature, the rate increased again with temperature. The drop in the rate of hydrolysis was attributed to changes in the physical properties of water.

2) *Measure the hydrolysis rate of methyl tert-butyl ether (MTBE) in sub- and supercritical water.* The rate of MTBE decomposition was experimentally measured in a batch reactor from 150 to 600°C and 250 bar. The decomposition rate showed a first-order dependence on the concentration of MTBE over the entire temperature range. The resulting first-order rate constant increased with temperature below the critical point and reached a local maximum. In the near-critical region, the rate constant dropped to local minimum and then increased with temperature above the critical point.

   To explain the extrema in the rate constant, an acid-catalyzed mechanism was hypothesized and yielded predictions that were consistent with the experimental observations. A new empirical rate expression was determined with a first-order dependence on the concentrations of H^+ and MTBE. For the entire temperature range studied from 150 to 600°C, the empirical rate expression quantitatively modeled the experimentally measured decomposition rate within the uncertainty of the experiments.

3) *Probe the reaction pathways of MTBE in sub- and supercritical water.* Experiments were conducted to measure the effect of pH on the decomposition rate of MTBE. The reaction rate increased under acidic conditions and decreased under basic conditions, which was consistent with the proposed acid-catalyzed reaction mechanism. The reaction order with respect to H^+ was found to be 0.83 ± 0.35 and 0.75 ± 0.19 (to 95% confidence) at 200 and 250°C (at 250 bar). These values were similar to the value of 1.0 predicted by the proposed mechanism. The discrepancy between measured and predicted values was most likely caused by the reverse reaction becoming more

significant under acidic conditions. The leveling off of the net experimental rate constant at low pH values supports this hypothesis.

The dependence of the reaction rate on pH at supercritical temperatures verified that the dominant reaction pathway is acid-catalyzed in that region, too. Quantifying the dependence on pH was difficult due to the high uncertainty in values for dissociation constants of HCl and NaOH in the supercritical region. However, the reaction order measured at 450°C was 0.57 ± 0.19. The apparent discrepancy between the measured slope and the predicted value of 1.0 was most likely due to two factors. The first is that the measured reaction rate under basic conditions included contributions from both the acid-catalyzed pathway and from the unimolecular decomposition pathway. Secondly, the measured reaction rate under acidic conditions was slower due to the reverse reaction. Experiments at 550 and 600°C under basic conditions were also conducted and the measured rate was equal to that predicted by the unimolecular decomposition pathway within experimental uncertainty.

These results confirm that the primary decomposition pathway of MTBE in both sub- and supercritical water involves acid-catalysis. Although the reaction order for H^+ was not conclusively verified over the entire temperature domain, the mechanism and rate expression developed in Chapter 5 are in reasonable agreement with the conclusions reached in this study.

Molecular Modeling Studies:

4) *Model the hydrolysis of* CH_2Cl_2*, correcting for solvent effects on the reaction rate.*

The effects of water as a solvent on the hydrolysis reaction of CH_2Cl_2 were modeled as a dielectric continuum using Kirkwood theory. A correction factor, obtained from *ab initio* calculations, was applied to adjust the activation energy in order to account for differences in the free energy of solvation of the reactant and the transition state. With the Kirkwood correction, the rate expression quantitatively predicted the experimentally measured reaction rate over the entire temperature range (from 100 to 500°C).

The resulting correlation was compared with a rate expression regressed previously in our laboratory. This previous rate expression was based on conversion measurements at the end of a non-isothermal preheater. The two rate expressions showed good agreement at temperatures from 320 to 370°C, where reaction rates were fastest and most of the conversion had occurred in the nonisothermal experiments.

5) *Determine the mechanism of MTBE hydrolysis and model the reaction rate.* Reaction pathways of MTBE decomposition in sub- and supercritical water were analyzed to establish the importance of acid/base catalyzed hydrolysis in comparison to unimolecular decomposition. Computational tools were employed to correct the activation energy of a gas-phase unimolecular decomposition pathway. Although correcting for solvent effects decreased the activation barrier from the value in the gas-phase, the pathway did not contribute significantly to the overall reaction rate for temperatures less than 550°C. However, the unimolecular decomposition rate set a lower bound on the reaction rate for each temperature. This lower bound on the rate was observed experimentally at supercritical temperatures under basic conditions, where the acid-catalyzed pathway was essentially shut off.

Diagnostic Equipment and Technique Development:

6) *Design and construct a new "state-of-the-art" SCWO reactor system.* A new, large-bore SCWO reactor system was developed and tested up to 600°C and 250 bar. The new system has the following advantages: 1) Organic compounds may be fed directly into the reactor, eliminating the need for preheating where hydrolysis or pyrolysis may occur; 2) The accessible concentrations of organic are not limited by solubility in ambient water; 3) The reactor has a movable sampling probe, allowing for a wide range of residence times; 4) The reactor has a large diameter (5 cm I.D.) to eliminate contact of the reactant with walls where surface reactions may interfere; 5) The movable sampling probe allows for measurement at many residence times without changing the flow conditions; 6) The reactor is optically accessible, allowing for *in situ* Raman spectroscopic measurements.

7) *Develop in situ Raman spectroscopy methods.* A small cell was designed and built with sapphire windows to allow for Raman measurements of species dissolved in $SCCO_2$. The Fermi dyad of CO_2 (1285 and 1388 cm^{-1}) was measured at temperatures ranging from 31.1 to 80ºC and pressures ranging from 30 to 136 bar. The peaks shifted monotonically to lower frequencies as the density of CO_2 was increased from 0.06 to 0.82 g/cc at temperatures from 31.1 to 80°C. Hot bands were observed at 1264 and 1409 cm^{-1}, and their relative size increased with increasing temperature.

   Two vibrational bands of benzene dissolved in CO_2 were measured over the same range of conditions studied for pure CO_2. The vibrational bands of benzene had larger Raman scattering cross-sections than CO_2, allowing for measurement at fairly dilute conditions (<5 mol%). Both peaks showed a shift to lower frequency as the density was increased up to values of approximately 0.4 g/cc. Further increasing the density did not cause further shift in the peaks. This shift was attributed to increased intermolecular interactions between the solute and nearby CO_2 molecules. The maximum shift observed was significantly smaller than the shift seen as benzene is condensed from a gas to a liquid, indicating that CO_2 does not interact as favorably as other benzene molecules do.

Two vibrational bands of CH_2Cl_2 were measured in CO_2 as temperature was varied from 31.1 to 80°C and with pressures of 30-136 bar. The scattering cross-section of the symmetric $C\text{-}H_2$ stretch was too small to obtain a good signal-to-noise ratio for the conditions studied. However, it did not appear that the CO_2 density affected the frequency significantly. The $C\text{-}Cl_2$ stretch was measured and showed similar behavior to benzene. The peak shifted to lower frequency as density was increased up to approximately 0.2 g/cc and then remained constant as density was further increased. This could indicate that the local density of CO_2 reaches liquid-like values at moderate densities, though, the maximum observed shift is still significantly smaller than that seen for liquid CH_2Cl_2.

Chapter 10

Recommendations

The objective of the work presented in this thesis was to obtain a better understanding of the effects of solvent molecules on reactions in sub- and supercritcal fluids. The following section lists recommendations for areas that should be investigated further based on observations and unresolved issues seen in this work:

1) **Explore applicability of CH_2Cl_2 results to other halogenated organics.** While methylene chloride is of practical interest itself, it is important to determine if the results of this study can be generalized to broader classes of organic compounds. The first extension would be to measure the hydrolysis kinetics of another simple chlorinated alkane, such as ethyl chloride (C_2H_5Cl) or either isomer of dichloroethane (CH_3CHCl_2 or CH_2ClCH_2Cl). These particular compounds are relevant because one might expect a similar hydrolysis mechanism to CH_2Cl_2. Furthermore, it is possible that the stabilization of the transition state of these compounds relative to the reactant would be similar. Therefore, a determination of whether the same values of the Kirkwood correction could be used for these other chlorinated alkanes is interesting. Further extension might also include chlorinated alkenes, such as dichloroethylene and trichloroethylene (TCE).

   A second extension to the results obtained from the study on methylene chloride would be to study the kinetics of dibromomethane hydrolysis. It is important to determine if the carbon-bromine bond reacts by the same mechanism as the carbon-chlorine bond.

2) **Determine the most efficient *ab initio* techniques for calculating solvation effects.** In *ab initio* calculations performed on CH_2Cl_2 and its transition state, the compounds were modeled as a spherical cavity containing a dipole moment and surrounded by a dielectric continuum. For the unimolecular decomposition of MTBE, the solvent was modeled as a polarized continuum around the solute, where the shape of the cavity was calculated as the contour where the electron density was a specified value. While the second method gives a more realistic model of the solvent shell, it is also computationally more expensive. Furthermore, the simpler method used in the methylene chloride studies were sufficient to model the effects over the entire temperature range, as demonstrated by the good agreement between the experimental data and the corrected rate expression.

   Secondly, the entire geometry was optimized for each value of dielectric strength in the studies on MTBE. It is likely, however, that there are more efficient ways of constraining the geometry to only include variations along the reaction coordinate. This would require looking at how the geometry in the remainder of the molecule (excluding the reaction coordinate) changed and how these changes affected the total energy calculated. The result of these two studies would be a determination of the level of calculations necessary to adequately model solvation effects in sub- and supercritical water.

3) **Investigate the contribution of the reverse reaction in the hydrolysis of MTBE.** One of the conclusions reached in the experiments under acidic conditions was that

the reverse reaction became significant, effectively slowing down the measured net reaction rate. One approach to probing the effects of reverse reaction would be to measure the rate of MTBE formation when methanol and *t*-butanol (and isobutene) are fed to the reactor. The excess of these products should increase the relative contribution of the reverse reactions and the measured net rate of disappearance would be slower.

Secondly, rate constants can be estimated for each of the later reaction steps using *ab initio* methods for each temperature and pressure. Kinetic modeling should be used to determine the concentration of each species for the entire reaction network and the relative contribution of each step to the overall observed rate. Several other pathways could be added to include protonation of MTBE from other sources, such as the carbocation.

4) **Compare the reaction pathways of MTBE to organic sulfides.** An obvious extension of the studies of the carbon-oxygen-carbon functional group is to study carbon-sulfur-carbon chemistry. Organic sulfides are an important class of chemicals for the application of chemical demilitarization. Methyl *tert*-butyl sulfide is a good starting point for this study because of its structural similarity to MTBE. However, the hydrolysis of thiodiglycol has been studied previously in our lab and therefore might be a convenient starting point. In either case, the initial experiments would focus on determining if the hydrolysis occurs by an acid-catalyzed mechanism. One would logically predict that the initial protonation would occur to a lower extent (slower) for the sulfide equivalent because it is less electronegative than oxygen. But

the second step should be faster because the carbon-sulfur bond is weaker than the carbon-oxygen bonds.

5) **Measure the decomposition of MTBE at similar temperatures and pressures in a non-aqueous medium.** By conducting decomposition measurements in a dense inert, such as Argon, the rate of the unimolecular decomposition can be validated. Furthermore, any effects of intermolecular interactions that occur when water is present could be eliminated. This would give a more conclusive understanding of the role water plays in the reaction mechanism. Secondly, small amounts of water or acid could be added to the Argon to further characterize the hydrolysis reaction pathways.

6) **Begin studies on the new SCWO reactor system.** The large-bore SCWO reactor has been tested with water up to 600°C and 250 bar. However, some problems have occurred in making the seal between the large reactor tube and the window block assembly. The first step towards using the reactor for measuring kinetics requires that the seal be made robust and consistent.

   After the sealing problem is overcome, the flow in the reactor needs to be characterized. This can be accomplished by measuring residence time distributions (RTD) using a tracer that will not hydrolyze, such as acetone. Patricia Sullivan has performed preliminary RTD studies on the continuous stirred tank reactor (CSTR) and a similar method should be employed for the large-bore reactor. The primary concern is that natural convection will induce radial mixing near the inlet to the reactor. If radial mixing is significant, the inlet may be modified to premix the organic with the high temperature water in a small volume prior to entering the main reactor. Additionally, the RTD studies will characterize the degree of radial diffusion of the tracer. Since all measurements are along the centerline, it is necessary to determine the amount of reactant (and products) diffusion to the remainder of the volumetric flow of water in the reactor.

7) **Combine Raman spectroscopy measurements with molecular dynamics (MD) simulations to model solvation in supercritical carbon dioxide.** In this study, Raman spectroscopy was used as a qualitative probe of solute-solvent interactions in supercritical carbon dioxide. To properly model the bandwidths and peak locations, however, the experimental measurements should be combined with MD simulations. This first requires the development of good pair potential functions for the solutes and CO_2. Because models for benzene and methylene chloride are not readily available, these need to be developed. Alternatively, measurements could be conducted with solutes such as N_2 or CO, where pair potential functions with CO_2 are already available.

8) **Use Raman spectroscopy to measure *in situ* compositions for reaction kinetics in supercritical CO_2.** The first step in using Raman spectroscopy for composition measurements in supercritical fluids requires proper calibration of the Raman scattering cross section ($d\sigma/d\Omega$) as a function of CO_2 temperature, pressure, and density. This should be done by first verifying the applicability of internal field effect scaling of Raman intensities in condensed phases. The internal field effect states that the ratio of the Raman scattering cross-sections can be approximated by:

$$\frac{(d\sigma/d\Omega)_{fluid}}{(d\sigma/d\Omega)_{gas}} = \alpha \cdot \left[\frac{n_r}{n_0} \cdot \frac{\left(n_r^{\ 2}+2\right)^2 \left(n_0^{\ 2}+2\right)^2}{81} \right]$$

where n_o and n_r respectively are the refractive index of the dense fluid at the excitation frequency, ω_o, and at the Raman scattered frequency, ω_o-ω_{vib}. The parameter α is an empirical constant that is approximately equal to 1, except for totally symmetric hydrogen stretching vibrations. Once calibrations are completed, Raman spectroscopy should be used to measure compositions for reaction systems of interest in $SCCO_2$.

Chapter 11

Appendices

11.1 Correlations for the Ion Dissociation Constant of Water (K_w)

11.2 Detailed Analytical Methods for Gas Chromatography

11.3 Tabulated Experimental Data

11.1 Correlations for the Ion Dissociation Constant of Water (K_w)

Historically, researchers in SCWO have used the Marshall and Franck (1981) (M&F) correlation for K_w over all temperature and density conditions. However, at the time that their correlation was developed, all of the experimental data used were at densities greater than 0.4 g/cc. Extrapolation to lower densities was deployed for prediction of K_w. Several authors have expressed concern over the accuracy of K_w at densities less than 0.4 g/cc (Pitzer, 1982; Bandura and Lvov, 2000). In a collaboration sponsored by the International Association for the Properties of Water and Steam (IAPWS), Bandura and Lvov (B&L) have developed a correlation with a more complete set of experimental data at lower densities and with the correct extrapolation to the ideal gas limit (Bandura and Lvov, 2000).

In our study presented in Chapters 5 and 6, we have used the M&F correlation for densities above 0.4 g/cc ($T < 390°C$) and the B&L correlation for lower densities ($T > 390°C$). A comparison of the values of K_w used for this study with the extrapolation of the M&F correlation is shown in Figure 1.3. Above the critical point of water, the B&L correlation predicts values of K_w approaching 3.5 orders of magnitude greater than the M&F extrapolation. The resulting proton concentration is 50 times greater with the B&L value of K_w.

Bandura, A. V., and S. N. Lvov (2000). In *Steam, water, and hydrothermal systems: Physics and chemistry meeting the needs of industry*, Tremaine, P. R., Hill, P. G., Irish, D. E., Palakrishnan, P. V., Eds., NRC Press, Ottawa.

Marshall, W. L., and E. U. Franck (1981). "Ion product of water substance, 0-1000°C, 1-10,000 bars. New international formulation and its background." *Journal of Physical Chemistry Reference Data* **94**: 295.

Pitzer, K. S., (1982). "Self-ionization of water at high temperature and the thermodynamic properties of the ions." *Journal of Physical Chemistry* **86**: 4754.

11.2 Detailed Analytical Methods for Gas Chromatography

HP 5890 Series II Gas Chromatograph : Light Gas Analysis

Column Type and Configuration	
Column	50 ft. x 1/8 in. 60/80 mesh Coarboxen 1000 column in series with 8 ft. x 1/8 in. 60/80 mesh Molsieve 5A column
Carrier Gas	28.5 mL/min (80°C) helium at 50 psig head pressure
Switching Valve	Initially through Carboxen, switch at 7.9 min
Injection Type and Configuration	
Injector	Manual, splitless
Injection volume	200 μL with 250 μL syringe
Inlet Type	Packed
Inlet Septa	SGE Auto-Sep 11 mm (p/n 041872)
Temperature Settings	
Inlet	110°C
Detector	110°C
Initial Oven Temperature	80°C for 4.0 min.
Ramp	40°C/min.
Final Oven Temperature	110°C for 8.0 min.
Detector Information	
Type	TCD
Reference Gas	36.0 mL/min of helium
Makeup Flow	off
Retention Times	
Oxygen	3.3 min.
Nitrogen	4.5 min.
Carbon Monoxide	6.3 min.
Carbon Dioxide	9.3 min.

HP 5890 Series II Gas Chromatograph : Light Hydrocarbon Analysis

Column Type and Configuration	
Column	15 m x 320 µm Astec GasPro bonded PLOT column (p/n 81103)
Carrier Gas	2.0 mL/min (70°C) helium at 10.0 psig head pressure
Injection Type and Configuration	
Injector	Manual, split 15:1
Injection volume	200 µL with 250 µL syringe
Inlet Liner	Split/splitless, glass wool packed, capillary inlet liner (HP p/n 19251-60540)
Inlet Septa	Supelco Thermogreen LB-2 11 mm (p/n 20654)
Temperature Settings	
Inlet	200°C
Detector	200ºC
Initial Oven Temperature	50ºC for 1.0 min.
Ramp	8.0ºC/min.
Final Oven Temperature	160ºC for 12.3 min.
Detector Information	
Type	FID
H_2 Flow	30 mL/min
Air Flow	300 mL/min
Auxiliary Gas	38.0 mL/min of nitrogen
Retention Times	
Methane	1.6 min.
Ethane	2.1 min.
Ethylene	2.5 min.
Acetylene	3.5 min.
Propylene	6.1 min.
Isobutene	10.5 min.

HP 5890 Series II Gas Chromatograph : Hydrogen and Helium Analysis

Column Type and Configuration	
Column	12 ft. x 1/8 in. 80/100 mesh Porapak T column in series with an 8 ft. x 1/8 in. 60/80 Molsieve 5A colcumn
Carrier Gas	Nitrogen at 50 psig head pressure
Switching Valve	Initially through Carboxen, switch at 7.9 min
Injection Type and Configuration	
Injector	Manual, splitless
Injection volume	200 µL with 250 µL syringe
Inlet Type	Packed
Inlet Septa	Supelco Thermogreen LB-2 11 mm (p/n 20654
Temperature Settings	
Inlet	120°C
Detector	120ºC
Oven Temperature	60ºC for 6.0 min.
Detector Information	
Type	TCD
Reference Gas	36.0 mL/min of nitrogen
Makeup Flow	off
Retention Times	
Helium	1.6 min.
Hydrogen	2.2 min.
Hydrocarbons	5.7 min.

HP 6890 Gas Chromatograph : Liquid Analysis for Organics

Column Type and Configuration	
Column	30 m x 530 µm x 1 µm film thickness DB-1 (J&W Scientific p/n 125-1035) preceded by 5 m of Restek Hydroguard column (Restek p/n 100810)
Carrier Gas	4.2 mL/min (80°C) helium at 3.7 psig head pressure
Purge Valve	Initially off, on at 1 min with purge flow of 3.0 mL/min
Injection Type and Configuration	
Injector	HP GC autoinjector
Injection volume	0.5 µL splitless with 5 µL syringe (fast injection)
Sample Settings	2 washes and 3 pumps
Solvent Washes	2 (with water) post injection
Inlet Liner	Single taper, glass wool packed, capillary inlet liner (HP p/n 5062-3587)
Inlet Septa	Merlin Microseal duckbill (HP p/n 5182-3442)
Temperature Settings	
Inlet	150°C
Detector	200ºC
Initial Oven Temperature	60ºC for 2.5 min.
Ramp	20ºC/min.
Final Oven Temperature	110ºC for 5 min.
Detector Information	
Type	FID
H_2 Flow	40 mL/min
Air Flow	450 mL/min.
Auxiliary Gas Flow	45 mL/min of N_2
Retention Times	
Methanol	2.350 min.
Dissolved Isobutene	2.485 min.
Ethanol	2.795 min.
Acetone	3.125 min.
tert-Butanol	3.585 min.
Methacrolein	4.096 min.
MTBE	4.252 min.

11.3 Tabulated Experimental Data

Tabulated data for CH_2Cl_2 hydrolysis experiments performed in glass ampoules at the vapor pressure. Some ampoule had Hastelloy C-276 powder mixed with the solution. Note: Concentration values correspond to mmol/L measured at ambient *T* and *P*.

***T* = 100°C, no metal present**

τ (hr)	$[CH_2Cl_2]$
0	22.10
42	18.58
90	16.77
162.5	12.09
210.5	12.06
258.5	10.31
330	7.57

***T* = 130°C**

Metal	τ (hr)	$[CH_2Cl_2]$
None	0.00	18.00
	14.50	12.87
	20.00	6.02
	43.00	3.89
	66.33	1.53
	92.00	0.53
15 mg	0.00	18.00
	15.50	12.69
	16.00	6.86
	41.50	5.78
	53.50	3.01
	89.50	0.84
200 mg	0.00	18.00
	16.50	12.57
	17.25	11.49
	19.50	7.88
	24.50	8.38
	47.00	4.37
	49.00	3.80
	72.75	2.07

***T* = 150°C**

Metal	**τ (min)**	**[CH_2Cl_2]**
None	0	16.00
	110	16.40
	205	10.82
	300	7.57
	420	3.63
	480	2.93
	570	1.85
None	0	16.00
	90	20.05
	150	17.09
	240	10.49
	360	5.41
	450	2.75
	570	1.35
15 mg	0	16.00
	105	14.73
	195	8.01
	285	6.89
	405	4.06
	465	2.44
	555	1.57
200 mg	0	16.00
	90	18.08
	195	10.33
	300	6.00
	360	4.88
	450	2.68
	540	1.74

***T* = 200°C**

Metal	**τ (min)**	**[CH_2Cl_2]**
None	0	18.00
	6	13.82
	10	9.91
	18	7.93
	30	2.24
	42	2.80
	48	1.04
15 mg	6	15.01
	10	9.71
	18	10.69
	24	5.87
	42	2.55
	48	2.46
200 mg	10	8.41
	18	9.05
	24	4.33
	30	1.67
	42	4.83
	48	2.06

***T* = 250°C**

Metal	**τ (min)**	**[CH_2Cl_2]**
None	0	22.10
	2	11.56
	4	2.58
	6	1.82
	10	0.60
15 mg	0	22.10
	2	14.24
	4	3.88
	6	1.06
	10	0.66
200 mg	0	22.10
	2	15.49
	4	2.08
	6	0.60

CH_2Cl_2 hydrolysis experiments performed with the high-temperature, high-pressure reactor at 250 bar.

T (°C)	**τ (s)**	**[CH_2Cl_2]**
300	5	24.00
	9	7.91
	11	10.79
	13	7.45
	15	5.72
	17	4.19
325	10	58.40
	20	17.75
	25	18.97
	30	7.58
	40	6.02
340	5	82.00
	10	45.58
	15	17.81
	20	22.85
	20	9.38
	25	25.65
	25	5.07
	30	0.56
	35	1.38
	35	2.31
	40	7.28
350	5	82.00
	5	81.98
	5	88.83
	10	41.54
	15	34.18
	15	40.02
	18	34.66
	18	17.88
	20	6.97
	22	12.51
	25	3.18
	30	1.65

T (°C)	**τ (s)**	**[CH_2Cl_2]**
360	5	85.08
	10	55.09
	15	26.14
	18	20.23
	20	10.75
	22	9.32
	25	5.69
	30	2.50
390	5	99.85
	5	79.30
	10	78.60
	13	68.24
	15	19.73
	17	58.80
	20	5.17
	25	63.47
450	120	0.373
	180	0.332
	240	0.279
	300	0.239
	360	0.213
	420	0.199
	480	0.181
	540	0.128
	600	0.095
500	60	0.327
	90	0.314
	150	0.159
	210	0.095
	240	0.061
	300	0.049
	360	0.041

Tabulated data for MTBE hydrolysis experiments at 250 bar under neutral pH conditions. Note: Concentration values correspond to mmol/L measured at ambient *T* and *P*.

T **(°C)**	**τ (s)**	**[MTBE]**	**[MeOH]**	**[*t*-BuOH]**	**[*i*-C_4H_8]**
150	300	4.072	0.025	0.015	0.000
	600	3.596	0.031	0.019	0.000
	1800	3.178	0.048	0.054	0.005
	3600	2.997	0.075	0.082	0.008
	7200	3.184	0.123	0.135	0.007
200	30	4.395	0.219	0.234	0.018
	120	3.873	0.334	0.404	0.045
	240	1.934	1.750	2.095	0.357
	480	1.244	2.141	2.581	0.464
	720	1.026	2.250	2.764	0.518
250	30	3.728	0.853	1.034	0.107
	45	3.580	0.875	0.986	0.152
	60	3.362	1.219	1.459	0.223
	90	2.756	1.469	1.770	0.295
	120	2.475	1.625	1.905	0.321
	300	0.781	2.625	2.865	0.732
	540	0.250	2.938	3.000	0.821
275	15	2.134	1.625	1.689	0.357
	30	1.082	2.109	2.297	0.450
	45	1.216	2.313	2.432	0.571
	60	0.616	2.656	2.568	0.875
	90	0.370	2.813	2.568	0.732
	120	0.177	2.969	2.757	0.804
300	5	1.161	2.000	1.892	0.411
	10	0.876	2.375	2.270	0.536
	15	0.218	2.594	2.027	0.375
	15	0.900	2.125	2.189	0.446
	20	0.435	2.406	2.189	0.589
	25	0.243	2.547	2.216	0.643
325	1	0.227	2.875	2.203	0.661
	2.5	0.128	3.000	1.986	1.268
	4	0.071	2.844	1.743	0.643
	7	0.016	3.219	1.662	0.804
	10	0.006	3.063	1.297	0.768

T (°C)	τ (s)	[MTBE]	[MeOH]	[t-BuOH]	[i-C_4H_8]
400	15	10.970	0.722	0.446	0.188
	30	10.440	0.891	0.554	0.309
	60	10.119	1.313	0.770	0.339
	90	8.789	1.719	0.919	0.434
	120	9.442	2.063	1.108	0.786
	180	7.265	2.891	1.392	0.732
	240	7.561	3.531	1.595	0.857
	300	6.991	4.031	1.784	1.036
400	20	10.184	1.469	0.919	0.473
	40	9.181	1.250	0.649	0.321
	60	7.775	3.313	1.838	0.875
	120	4.612	5.375	2.541	1.125
	180	5.302	5.125	2.338	1.071
	240	5.177	4.781	2.162	1.286
	300	3.730	6.094	2.378	1.357
	540	2.670	6.875	2.338	1.214
425	15	12.007	1.469	0.770	0.402
	15	10.249	1.906	1.000	0.438
	30	10.616	2.500	1.149	0.732
	45	8.830	3.656	1.541	0.938
	60	9.140	4.094	1.595	0.786
	120	5.844	5.031	1.777	1.098
	180	5.774	6.625	2.108	1.446
	240	4.384	7.375	2.041	1.598
	360	2.414	8.906	1.905	3.464
425	30	7.877	3.594	1.757	0.946
	60	6.946	4.938	2.297	1.027
	90	5.610	5.500	2.203	1.429
	180	3.657	7.750	2.270	1.625
	300	1.762	9.188	1.946	1.768
450	5	8.618	4.594	1.338	0.643
	7	7.136	6.250	1.784	1.071
	15	6.256	6.875	1.743	1.893
	20	6.100	7.281	1.392	1.214
	25	4.899	8.281	1.730	1.643
	45	3.174	10.063	1.270	1.804
	60	1.944	10.156	0.905	3.393

T (°C)	τ (s)	[MTBE]	[MeOH]	[*t*-BuOH]	[*i*-C_4H_8]
450	5	11.392	3.781	1.014	0.786
	10	8.881	5.000	1.311	1.125
	20	8.397	6.000	1.378	1.179
	30	5.399	8.625	2.216	1.571
	40	4.752	9.219	1.662	1.786
	50	4.653	8.438	1.554	1.946
	60	2.641	8.125	1.041	3.036
475	15	6.106	7.969	1.378	1.446
	30	4.123	9.625	1.297	1.857
	45	2.432	11.438	1.054	1.964
	60	1.665	11.750	0.878	1.893
	90	0.690	12.000	0.568	2.286
500	5	7.830	6.781	1.135	1.607
	5	5.847	5.875	0.865	3.661
	10	5.245	9.375	1.351	1.429
	15	4.420	9.375	0.946	2.911
	20	2.938	9.688	0.743	3.304
	30	2.241	11.594	0.649	2.429
	45	1.442	14.063	0.554	2.821
550	5	5.081	10.625	0.662	1.946
	10	3.509	12.813	0.507	2.054
	15	2.366	13.281	0.392	2.339
	20	1.611	12.813	0.351	2.464
	25	1.271	13.938	0.257	1.964
	30	0.932	15.094	0.209	2.911
	40	0.428	12.500	0.155	2.589
575	5	4.203	10.000	0.358	1.786
	5	3.808	9.125	0.311	1.643
	7	3.291	12.031	0.284	1.536
	10	2.259	13.750	0.230	2.089
	15	1.348	14.344	0.159	2.607
	20	0.935	14.688	0.151	2.946
	30	0.369	14.375	0.104	2.714

***T* (°C)**	**τ (s)**	**[MTBE]**	**[MeOH]**	**[*t*-BuOH]**	**[*i*-C_4H_8]**
600	5	2.807	14.375	0.284	2.107
	10	1.726	13.906	0.189	2.429
	15	0.742	11.344	0.100	2.411
	20	0.590	13.438	0.100	2.732
	25	0.297	12.594	0.089	2.321
	30	0.127	15.938	0.086	3.161

Tabulated data of MTBE hydrolysis experiments at 250 bar and under acidic and basic conditions. Note: Concentrations reported as ambient mmol/L.

***T* = 200°C**

pH (ambient)	**τ (s)**	**[MTBE]**	**[MeOH]**	**[*t*-BuOH]**	**[*i*-C_4H_8]**
3.0	10	5.888	0.331	0.622	0.143
	20	3.912	0.625	1.128	0.357
	30	2.965	1.063	1.784	0.643
	60	2.223	1.375	2.041	0.625
	90	1.015	2.406	3.135	1.143
	120	0.472	2.313	2.878	0.982
3.7	15	5.222	0.406	0.622	0.161
	45	3.037	1.500	2.081	0.679
	90	2.149	1.375	1.892	0.571
	135	0.778	2.250	2.716	1.000
	180	0.314	2.313	2.973	1.143
10.0	30	5.562	0.000	0.000	0.000
	4500	5.109	0.000	0.070	0.000
	9900	4.713	0.000	0.109	0.000
11.0	300	4.981	0.000	0.000	0.000
	1800	4.909	0.000	0.000	0.000
	6000	4.941	0.000	0.039	0.000

***T* = 250°C**

pH (ambient)	**τ (s)**	**[MTBE]**	**[MeOH]**	**[*t*-BuOH]**	**[*i*-C_4H_8]**
3.0	5	1.105	2.438	2.905	2.911
	10	0.450	2.594	3.014	3.125
	15	0.216	2.844	3.203	2.911
	20	0.114	3.375	3.176	3.089
3.7	5	2.795	1.938	2.838	1.625
	10	0.972	2.406	3.365	2.714
	15	0.386	1.750	2.311	2.339
	20	0.195	2.688	3.392	2.536
	30	0.115	3.313	3.838	2.911
10.0	30	7.272	0.000	0.045	0.000
	600	5.952	0.581	0.824	0.223
	1800	4.420	1.438	2.095	0.643
	5400	1.891	2.594	3.622	1.304
11.0	60	7.955	0.000	0.000	0.000
	720	7.643	0.100	0.155	0.000
	1800	7.441	0.225	0.365	0.096
	5400	4.802	0.475	0.676	0.264

***T* = 450°C**

pH (ambient)	τ (s)	[MTBE]	[MeOH]	[*t*-BuOH]	[i-C_4H_8]
3.0	7	4.477	12.500	3.716	6.875
	10	3.173	12.906	3.095	8.625
	15	3.123	13.750	3.311	7.679
	20	2.506	13.844	2.973	8.036
	30	1.640	14.781	2.554	9.643
	45	1.170	15.625	2.095	9.643
3.7	5	9.096	10.875	3.959	6.321
	15	6.422	11.563	3.486	7.946
	30	3.756	14.219	2.865	8.839
	45	2.665	14.844	2.338	8.929
	60	1.856	15.406	1.811	9.554
10.0	30	23.238	0.191	0.051	0.121
	300	20.821	1.469	0.291	1.018
	1200	17.435	4.219	0.730	3.107
	3600	10.948	8.625	1.243	5.143
11.0	30	25.587	0.141	0.000	0.077
	180	22.574	0.575	0.072	0.295
	600	20.146	1.500	0.216	0.732
	1800	18.711	4.219	0.676	2.643

***T* = 550°C**

pH (ambient)	τ (s)	[MTBE]	[MeOH]	[*t*-BuOH]	[i-C_4H_8]
10.0	15	10.78	4.34	0.16	1.03
	45	5.42	8.97	0.24	1.84
	60	4.43	9.16	0.18	1.89
	90	2.26	10.69	0.22	2.16
	120	1.51	11.84	0.16	2.25
	150	0.93	10.94	0.14	2.07
	180	0.33	12.56	0.14	2.41

T **= 600°C**

pH (ambient)	**τ (s)**	**[MTBE]**	**[MeOH]**	**[*t*-BuOH]**	**[*i*-C_4H_8]**
10.0	5	6.781	8.375	0.189	1.429
	10	4.183	9.906	0.157	2.018
	15	1.757	12.188	0.139	2.357
	20	0.777	12.031	0.103	2.232
	30	0.178	12.031	0.127	2.429
	40	0.060	11.875	0.072	2.446